UNIVERSIDADE DE SÃO PAULO
INSTITUTO DE FÍSICA DE SÃO CARLOS

Guilherme Tomishiyo Teixeira de Sousa

Rapidly rotating condensates in a bubble trap

São Carlos

2022

Guilherme Tomishiyo Teixeira de Sousa

Rapidly rotating condensates in a bubble trap

Thesis presented to the Graduate Program in Physics at the Instituto de Física de São Carlos da Universidade de São Paulo, to obtain the degree of Doctor in Science.

Concentration area: Basic Physics

Advisor: Dra. Mônica Andrioli Caracanhas Santarelli

Original version

São Carlos
2022

Sousa, Guilherme Tomishiyo Teixeira de
Rapidly rotating BECs in a bubble trap / Guilherme Tomishiyo Teixeira de Sousa; advisor Mônica Andrioli Caracanhas Santarelli -- São Carlos 2022.
143 p.

Thesis (Doctorate - Graduate Program in Basic Physics) -- Instituto de Física de São Carlos, Universidade de São Paulo - Brasil , 2022.

1. Atomic physics. 2. Bose-Einstein condensates. 3. vortices. 4. Bubble trap. 5. Quantum gases. I. Santarelli, Mônica Andrioli Caracanhas, advisor. II. Title.

FOLHA DE APROVAÇÃO

Guilherme Tomishiyo Teixeira de Sousa

Dissertação apresentada ao Instituto de Física de São Carlos da Universidade de São Paulo para obtenção do título de Doutor em Ciências. Área de Concentração: Física Básica

Aprovado(a) em: 01/12/2022

Comissão Julgadora

Dr(a). Mônica Andrioli Caracanhas Santarelli

Instituição: (IFSC/USP)

Dr(a): Lauro Tomio

Instituição: (UNESP/São Paulo)

Dr(a). Emanuel Alves de Lima Henn

Instituição: (IFSC/USP)

Dr(a): Reinaldo Santos de Lima

Instituição: (IAG/USP)

Dr(a): Marcos César de Oliveira

Instituição: (UNICAMP/Campinas)

This is work is dedicated to friends: friends who have always been supportive, who believed in me even when I myself did not. I wouldn't make it without you.

ACKNOWLEDGEMENTS

First I would like to thank the endless efforts and support of my supervisor, Mônica Caracanhas, who accepted me as student when I was in a dire need. I would also want to thank Prof. Vanderlei Bagnato for the financial support, scientific advice and for creating a very intellectually stimulant environment in the institute, invaluable in the process of learning. I own many thanks to students and staff from the Optic's Group, in particular, Lucas Madeira for all the help with physics discussion, computer related issues and bibliographical suggestions.

My thanks are also owned to my parents and family: without your support, comprehension, patience and tolerance for all my mistakes and delays, this work would not be possible.

Finally, I would like to thank CNPq under the grant 140663/2018-5 for providing all the financial support that made it possible for working in this project with my full attention and dedication.

"A delayed game is eventually good, but a rushed game is forever bad."
Shigeru Miyamoto

ABSTRACT

SOUSA, G. T. T. de **Rapidly rotating condensates in a bubble trap**. 2022. 143p. Thesis (Doctor in Science) - Instituto de Física de São Carlos, Universidade de São Paulo, São Carlos, 2022.

We study a rotating Bose-Einstein Condensate (BEC) trapped in a shifted harmonic oscillator and Mexican Hat trap, which approximates the potential of a bubble trap potential in some situations. We determined the vortices configurations that appears in this system by varying the interaction and angular momentum of the atomic cloud. The system phase diagram has the macrovortex configurations for small values of the interaction parameter. The charge of the central vortex increases with increasing rotation. Higher values of the atomic interaction turns the macrovortex unstable. It decays into multiple single-charged vortices that arrange themselves in a lattice. Since the vortices are not always visible in the absorption images, we look for alternative methods to characterize the vortex configuration. More specifically, we search for experimental signatures to determine the transitions in the phase diagram. For that, we study how the BEC's velocity field affects the collective modes of the condensate. The splitting of the modes degenerescence and the increase in the mode frequency with angular velocity, which can be traced to a reduction in the gas compressibility, can be seen as an indirect signature of the presence of the vortices in the trapped BEC.

Keywords: Atomic physics. BECs. Vortices. Bubble trap.

RESUMO

SOUSA, G. T. T. de **Condensados em rápida rotação em armadilhas do tipo bolha**. 2022. 143p. Tese (Doutorado em Ciências) - Instituto de Física de São Carlos, Universidade de São Paulo, São Carlos, 2022.

Nós investigamos o comportamento de um condensado de Bose-Einstein (BEC) em rotação em armadilhas do tipo oscilador harmônico deslocado e chapéu mexicano, que aproximam um potencial do tipo bolha em algumas situações. Determinamos as configurações de vórtices que aparecem no sistema ao variar-se o momento angular da nuvem e o parâmetro de interação. O diagrama de fases do sistema possui uma configuração de macrovórtice para valores pequenos do parâmetro de interação. A carga do vórtice central aumenta com o aumento da velocidade de rotação. Valores mais altos do parâmetro de interação tornam o macrovórtice instável, promovendo seu decaimento em múltiplos vórtices de carga unitária que se arranjam em uma rede. Uma vez que os vórtices nem sempre são visíveis nas imagens por absorção, procuramos por métodos alternativos para caracterizar a configuração de vórtices. Mais especificamente, procuramos por assinaturas experimentais para determinar a transição no diagrama de fases. Para isso, estudamos o efeito que o campo de velocidades do condensado provoca nos modos coletivos do condensado. A separação dos modos degenerados, juntamente com o aumento da frequência com a velocidade angular, associada a uma redução na compressibilidade do gás, pode ser vista como uma assinatura indireta da presença de vórtices em um condensado armadilhado.

Palavras-chave: Física atômica. BECs. Vórtices. Armadilhas do tipo bolha.

LIST OF FIGURES

LIST OF ABBREVIATIONS AND ACRONYMS

BEC	Bose-Einstein Condensate or Bose-Einstein Condensation
LLL	Lowest Landau Level
MH	Mexican Hat
SHO	Shifted Harmonic Oscillator
TAAP	Time averaged adiabatic potentials
TOP	Time orbiting potential

CONTENTS

1 INTRODUCTION

Bose-Einstein condensates (BECs) are not a novel phenomenon: their prediction dates back to the pioneer works of Bose and Einstein in 1925 (1); however its experimental realization in ultra-cold gases had to wait much longer, taking place only in 1995 (2). A condensate realized in ultra-cold gases, in contrast to liquid helium, the archetypal BEC, is interesting because the weak interaction between the gas' constituents allow for a much larger condensate fraction (defined as the ratio between the number of particles occupying the condensate state to the total number of particles). Another desirable consequence of the weak interaction is the larger size of the vortex cores, which make them easier to observe when compared to liquid helium. Other virtues worth noticing include the simple mathematical description possible due to the macroscopic occupation of the ground state, the experimental possibility of controlling multiple parameters of the system (from the strength and sign of interaction by means of the Fano-Fesbach resonance to the geometry of the system by exploring many trap configurations) and the spatial scales being in the μm order, allowing for imaging by absorption techniques. Since their experimental realization, condensates have offered contributions to multiple areas in physics: from atomic physics to condensate matter, optics and high energies.

Interacting BECs can also be superfluids. Rotating superfluids manifests a dramatic feature of the quantum nature of the system: because a weakly interacting condensate can always be described by a single particle wave function, with a well defined phase and module, it can be shown that if we relate the module of the wave function to the gas' density and the gradient of the phase to the gas' velocity field, then the curl of the velocity field — and therefore its circulation — must always vanishes in a closed loop, except if the loop contains singular points. The caveat mentioned in the last sentence is no mere curiosity however, since it entails the formation of quantized vortices: lines of vanishing density around which the phase of the condensate changes by an integer multiple of 2π, a phenomenon already known from superconducting physics. In condensates trapped by harmonic oscillator type potentials (the most common potential, usually describing the bottom of an Ioff trap in a quadrupole configuration (3)), increasing the system's angular velocity results in the formation of additional vortices that arranges themselves in the condensate forming a lattice. By overlapping their velocity fields, this vortices mimic the behavior of a rigid body rotating at that same angular velocity. However, the angular velocity cannot increase without limit since centrifugal effects due to the rotation cancel the effects of the trap at a critical angular velocity determined by the trapping frequency, leading to a deconfinement of the gas. This problem prompted research of anarmonic potentials, capable of maintaining confinement even after the critical angular velocity.

Initially efforts were concentrated in a quadratic plus quartic potential, were it was predicted that for an ever increasing velocity a hole must form around the condensate's rotation axis, creating a regime where the condensate occupies in bulk an annular region together with a lattice of vortices. With even higher angular velocities the width of the annular region decreases while the radii of the whole increases, with the condensate occupying a thin ring. The vortices now would migrate from the bulk to the hole, occupying the zero density region and forming what was called a giant vortex or macrovortex (4). Experimental results were, however, inconclusive: no vortices were found past the rapidly rotating regime (5). The authors of (5) suggest that either the mean field approximation fails to be applicable to the condensate in this regime or there is a tilting of the vortex axis with respect to the plane of the condensate which disturbs the absorption imaging technique. Seeking in parts to address this problem, another potential that attracted the attention of the community was the bubble trap potential. This is a potential that allows for control over the shape and topology of the system, and also provides a stronger than harmonic term for the confining potential (6). In many situations of interest, this potential can be related to the simpler shifted harmonic oscillator potential, also called a ring potential due to the annular shape a BEC takes when trapped by this potential. In other situations it can be approximated as a Mexican Hat type potential, formed by a quartic minus a quadratic term.

In this work, we seek to characterize analytically and numerically dynamical and equilibrium properties of a rotating BEC under a bubble trap. Different techniques are required for weak and strong interactions. For a weakly interacting gas we follow an idea originally proposed by Butts (7) and suppose the system to be described by the product of a Gaussian and a power or the radius, with the power being related to the system's angular momentum. We then minimize the system's energy to obtain relevant parameters for a given angular velocity and interaction parameter. This results in predictions for the vortices charge and charge distribution in the phase space formed by the angular velocity and interaction parameter, and those predictions are investigated numerically with use of a Crank-Nicholson scheme with imaginary time propagation. Another prediction is made by using perturbation theory, where the boundaries between pure states of different charge is computed. Second order transitions, i.e, macrovortex becoming unstable and decaying in singly charged vortices are analyzed by studying the stability matrix of the system.

For higher interaction parameters the Gaussian no longer describes the condensate with satisfaction, but it becomes possible to use the Thomas-Fermi approximation. This approximation takes a different form depending in the trapping potential and the vortex distribution. In this work, we analyze the cases of a pure macrovortex or a vortex lattice. The resulting Thomas-Fermi profiles are then used to better understand the behavior of the vortices in the phase diagram initially created in the first part of this work. Once more the results are checked against numerical predictions.

For the dynamical properties, we studied the monopole and in-plane quadrupole modes of the system, using sum rules for obtaining analytical expressions em terms of expected values of the energies for the frequencies of the modes. We also simulated this modes numerically by creating adequate perturbations in the initial state of the condensate and evolving it in real time. Our expectations were that the presence of vortices would produce effects in the collective modes, in this way allowing a method for indirect detection of vortices that does not relying in imaging techniques. For the monopole mode, we found a behavior already familiar in the literature for the quartic potential: the frequency of the mode increases, but not considerably, with the angular velocity. We also found that a vortex lattice produces higher frequencies than a macrovortex, for the same total charge. For the quadrupole mode, the presence of rotation breaks the degeneracy of two modes that carry opposite angular momentum, with the splitting of the modes being proportional to the total angular momentum.

2 THEORETICAL INTRODUCTION

In this chapter we establish the basic theory required in our work. We begin discussing the phenomenon of Bose-Einstein condensation in an ideal free gas. We then discuss Fano-Fesbach resonances and how magnetic fields can be used to manipulate the s-wave scattering length in ultracold collisions, a feature that can be explored to attain a controllable interaction strength between ultracold BEC atoms. Treating the interaction in a mean field approach leads to the Gross-Pitaevskii equation, a key equation in BEC theory. With this equation, it is possible to show that the BEC can be thought as a fluid obeying equations similar to hydrodynamical equations, an important feature in studying the collective modes of the gas. With the hydrodynamic analogy, it is possible to relate the phase of the wave function with the velocity field of the gas, and due to the single valuedness of the wave function, one can show that the phase (and hence the velocity field) must be quantized in any closed loop. A non-vanishing winding leads to the phenomenon of a vortices and vortex lattices in rotating BECs. The subsequent structure of the condensate depends on how fast the condensate rotates in comparison to the trap frequency, and if the two frequencies are comparable one reaches a Lowest Landau Level (LLL) regime, which is in direct analogy to the Quantum Hall effect from condensate matter physics. While in a free and harmonically trapped gas with rotation one can show by an energy argument that vortices always have charge 1, the situation changes if the potential is not harmonic: this leads to multiply quantized vortices. The formation of a vortex lattice or a multiply quantized vortex is therefore a function of the both the rotation rate and the interaction strength, which we can represent as a phase diagram in this parameter space. Finally, we end the chapter discussing collective modes, which can be studied by means of the hydrodynamic description or by the sum rule approach. This modes changes if the trapping potential changes, and therefore we include analysis of both harmonic and quartic trappings.

2.1 Bose-Einstein condensation

2.1.1 A heuristic introduction

Before giving a formal definition of Bose-Einstein condensation, we begin with a more simple heuristic discussion. The concept of a BEC was originally proposed by Bose in 1924, (1) and latter elaborated by Einstein in 1925. (8) The observation from Bose, in attempting to explain why classical statistics were inadequate in low temperature regimes, was to argue that in a system where the particles are ideal bosons (non-interacting particles possessing integer spins), there would be nothing preventing a large scale occupation of the ground state, provided the temperature was low enough. This is to be contrasted to fermion particles (particles with half-integer spins), where even at absolute zero there can be no large scale occupation of the ground state because of Pauli's exclusion principle.

A simple order of magnitude estimation of the condensation temperature can be done by means of a dimensional argument. The relevant parameters for an ideal, homogeneous boson gas are the temperature T, the number of particles per unit volume n and the particle's mass m. The only energy scale that can be formed by those parameters is the combination $\hbar^2 n^{2/3}/m$, where $\hbar = 2\pi h$ and h is the Planck's constant. By dividing by the Boltzmann's constant k_B, we obtain

$$T_C \sim \frac{\hbar^2 n^{2/3}}{m k_B}. \tag{2.1}$$

If this equation is evaluated for liquid ^{4}He at saturated vapour pressure, it yields $T_C \sim 3.13\,\mathrm{K}$, which is close to the lambda point temperature $T_\lambda = 2.17\,\mathrm{K}$.

Another way to think about the onset of condensation is to ascribe to each particle in the gas a length scale, the thermal De Broglie's wavelength given by

$$\lambda_T = \left(\frac{2\pi\hbar^2}{m k_B T}\right)^{1/2}, \tag{2.2}$$

then to define the temperature of condensation to be the temperature where this length scale becomes of the same order of the mean interparticle separation given by $n^{-1/3}$. This yields:

$$T_C \sim 2\pi\frac{\hbar^2 n^{2/3}}{m k_B}, \tag{2.3}$$

which is of the same order of Eq.(2.1). This suggests a simple physical picture that when the temperature is low enough the wave function of individual particles of the gas start to overlap and the gas as a whole behaves in a coherent way. This notion can be made more rigorous and sophisticated and we shall discuss it further in the next section.

Finally, it is also possible to think about BECs in terms of the chemical potential of a gas of particles occupying a volume V in contact with a thermal reservoir of temperature T and with a particle reservoir of N particles. For this system the grand partition function can be written as (9):

$$\ln \Theta(T, V, \mu) = -\sum_j \ln\left\{1 - \exp\left[-\left(\varepsilon_j - \mu\right)/k_b T\right]\right\}, \tag{2.4}$$

where the sum is over all particle states j with energy ε_j. For this function it is easy to show that if the occupation of a state is unbounded, then the occupation number of the

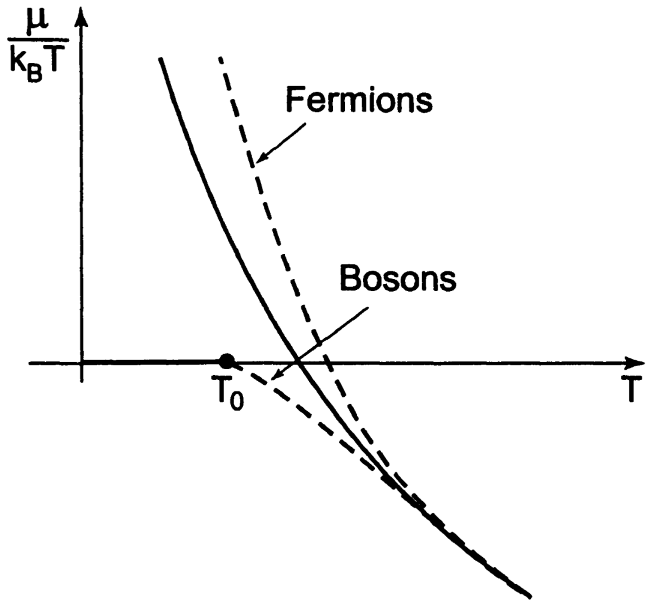

Figure 1 – Chemical potential as a function of temperature for classical particles (solid line), bosons and fermions. For bosons, the system undergoes Bose-Einstein condensation at temperature T_0, where the chemical potential takes the constant value $\mu = 0$.
Source: SALINAS(9)

state j at temperature T is given by the Bose statistics:

$$\langle n_j \rangle = \frac{1}{\exp\left[\left(\varepsilon_j - \mu\right)/k_B T\right] - 1}, \tag{2.5}$$

and the total number of particles is

$$N = \sum_j \frac{1}{\exp\left[\left(\varepsilon_j - \mu\right)/k_B T\right] - 1}. \tag{2.6}$$

Equation (2.6) can be solved for μ as a function of N, T and V. In particular, in the classical limit one can show that

$$\frac{\mu}{k_B T} = \ln\left[\frac{1}{\gamma}\left(\frac{2\pi\hbar^2}{m k_B}\right)^{3/2}\right] + \ln\left(\frac{N}{V}\right) - \frac{3}{2}\ln T, \tag{2.7}$$

where $\gamma = 2S+1$ is the multiplicity of spin. If we take the lowest state to have $\varepsilon_0 = 0$, then clearly in order to have $\langle n_0 \rangle \geq 0$ in Eq.(2.5) we need $\mu \leq 0$. For large T in Eq.(2.7) μ is indeed negative, but as T decreases the classical expansion allows for $\mu \geq 0$. For fermions this is indeed the case: for low enough temperatures, adding particles actually increases the free energy of the system for low enough temperatures, because Pauli's exclusion principle precludes particles from population the same quantum state. But for bosons, for some temperature T_C the system reaches $\mu = 0$ and remains at this constant value.

When this temperature is reached there's no change in free energy with the addition of particles to the system, and the lowest energy state acts as a particle reservoir. This is displayed schematically in Figure 1.

The condensation temperature T_c can be calculated using Eq.(2.6) by setting $\mu = 0$ at this temperature. We can then use the energy spectrum of free particles, $\varepsilon_j = \varepsilon_k = \hbar^2 k^2/2m$ and transform the sum over the states into an integral (in the thermodynamic limit):

$$N = \gamma V C \int \frac{\varepsilon^{1/2}}{\exp\left(\varepsilon/k_B T_C\right) - 1} d\varepsilon, \tag{2.8}$$

with $C = \frac{1}{4\pi^2}\left(\frac{2m}{\hbar^2}\right)^{3/2}$. This has the solution

$$T_C = \frac{1}{2}\left[\frac{4\pi^2}{\gamma\Gamma\left(\frac{3}{2}\right)\zeta\left(\frac{3}{2}\right)}\right]^{3/2} \frac{\hbar^2 n^{2/3}}{m k_B}, \tag{2.9}$$

which is equal to the previous results Eq.(2.3) and Eq.(2.1), apart from the numerical factor containing the Gamma function $\Gamma(3/2)$ and the Zeta function $\zeta(3/2)$.

In this work we are normally concerned with condensates with a high condensate fraction, i.e, $N_0/N \sim 1$, where N_0 is the number of particles occupying the ground state. Experimentally, this can be realizable in ultracold gases of alkali atoms, where the number density ranges from $10^{13} - 10^{15}\,\mathrm{cm}^{-3}$.This yields condensation temperatures that ranges from hundreds of nK to a few μK.

2.1.2 Critical temperature for non-uniform condensates

The same basic principles used to calculate the critical temperature in a uniform condensate holds for calculating it if the condensate is under a trapping potential, the difference being that now in passing from a discrete sum to an integration, one was to account carefully for the density of the states for a given energy. As an illustration of the process, we quickly reproduce the resulting critical temperature for the uniform condensate. For simplicity we shall omit any contributions due to internal states such as spin states.

There is in average one quantum state per volume $(2\pi\hbar)^3$ of the phase space. The region of the momentum space where the particle has a momentum of magnitude p or less is $4\pi p^3/3$, and the relation between the energy and momentum is that of a free particle $\epsilon = p^2/2m$. The total number of states with energy of ϵ or less is thus given by $G(\epsilon)$:

$$G(\epsilon) = V\frac{2^{1/2}}{3\pi^2}\frac{(m\epsilon)^{3/2}}{\hbar^3}, \tag{2.10}$$

with V being the volume of the system. If $G(\epsilon)$ is the total number of states with energy equal of less than ϵ, then the number of states with energy between ϵ and $\epsilon + d\epsilon$ is simply $g(\epsilon) = dG(\epsilon)/d\epsilon$:

$$g(\epsilon) = \frac{Vm^{3/2}}{2^{1/2}\pi^2\hbar^3}\epsilon^{1/2}. \tag{2.11}$$

In possession of the density of the states, the number of particles populating excited states is given by the integral

$$N_{ex} = \int_0^\infty d\epsilon g(\epsilon) n(\epsilon), \tag{2.12}$$

where $n(\epsilon)$ is the occupation number of states with energy ϵ and is given by Eq.(2.5). In the critical temperature all particles (except for a vanishing small quantity in comparison with the total number) can be accommodated in the excited states and the chemical potential vanishes, so the integral becomes:

$$N = \frac{Vm^{3/2}}{2^{1/2}\pi^2\hbar^3}\Gamma(3/2)\zeta(3/2)\left(k_B T_C\right)^{3/2}, \tag{2.13}$$

which upon solving for T_C gives the same result of Eq.(2.9) for $\gamma = 2$.

We now turn to problem of calculating the critical temperature in a trapped condensate, specifically, let us assume the harmonic oscillator in three dimensions potential:

$$V(\boldsymbol{r}) = \frac{1}{2}m(\omega_x x^2 + \omega_y y^2 + \omega_z z^2), \tag{2.14}$$

where ω_x, ω_y and ω_z denotes the trapping frequencies in the x, y and z directions respectively. The solution to the single particle Schrödinger equation subject to this potential prescribes the particle energy levels to be given by three integer quantum numbers, n_x, n_y and n_z (10):

$$\epsilon(n_x, n_y, n_z) = (n_x + 1/2)\,\hbar\omega_x + (n_y + 1/2)\,\hbar\omega_y + (n_z + 1/2)\,\hbar\omega_z. \tag{2.15}$$

To determine the total number of states consistent with an energy of ϵ, we first neglect the zero point motion, i.e, the factors of 1/2 in Eq.(2.15). Next, we shall treat the variables n_x, n_y and n_z as continuous, rather than discrete numbers. This approximations are reasonable if ϵ is large compared to $\hbar\omega_i$, $i = x, y, z$. Then we define a new coordinates system given by $\epsilon_i = \hbar\omega_i n_i$, in terms of which a surface of constant energy ϵ is the plane $\epsilon = \epsilon_x + \epsilon_y + \epsilon_z$. The total number of states is thus the volume in the first octant (because the integers must be positive) bounded by the plane,

$$G(\epsilon) = \frac{1}{\hbar^3\omega_x\omega_y\omega_z}\int_0^\epsilon d\epsilon_x \int_0^{\epsilon-\epsilon_x} d\epsilon_y \int_0^{\epsilon-\epsilon_x-\epsilon_y} d\epsilon_z = \frac{\epsilon^3}{6\hbar^3\omega_x\omega_y\omega_z}. \tag{2.16}$$

Since $g(\epsilon)$ is the derivative of the equation above, we obtain for the density of states:

$$g(\epsilon) = \frac{\epsilon^2}{2\hbar^3\omega_x\omega_y\omega_z}. \tag{2.17}$$

This result can be generalized to d dimensions (11):

$$g(\epsilon) = \frac{\epsilon^{d-1}}{(d-1)!\Pi_i\hbar\omega_i}. \tag{2.18}$$

As is illustrated by the previous cases, the density of states often take the form

$$g(\epsilon) = C_\alpha\epsilon^{\alpha-1}. \tag{2.19}$$

For instance, for the $3D$ harmonic oscillator, $\alpha = 3$ and $C_3 = 1/\left(2\hbar^3\omega_x\omega_y\omega_z\right)$, while for a free gas in $3D$ $\alpha = 3/2$ and $C_{3/2} = Vm^{3/2}/2^{1/2}\pi^2\hbar^3$. The corresponding critical temperature is then given by the same procedure, by taking the density of states and integrating like Eq.(2.12).

Before moving to the next section, there is an important remark to be made: for a free two dimensional Bose gas, $\alpha = 1$. This implies that the density of states is independent of the energy and therefore the integral Eq.(2.12) diverges, implying that Bose-Einstein condensation only happens at the absolute zero, $T_C = 0$. This, however, is not necessarily true for a *trapped* condensate. For instance, for a gas trapped by a $2D$ harmonic oscillator potential, $\alpha = 2$ and the integral does not diverge. The same can be said if the topology of the system is different, for instance, if the particles are constricted to occupy the surface of a sphere (12, 13).

2.1.3 Off-diagonal long range order

The relevant framework for introducing a more formal definition of a BEC is a field theory. We shall assume that $\hat{\Psi}^\dagger(\boldsymbol{r})$ ($\hat{\Psi}(\boldsymbol{r})$) is the field operator creating (annihilating) a boson particle at position $\boldsymbol{r}$. These operators are themselves written as combinations of single particle wave functions ψ_m:

$$\hat{\Psi}^\dagger(\boldsymbol{r}) = \sum_m a_m^\dagger\psi_m(\boldsymbol{r}), \tag{2.20}$$

$$\hat{\Psi}(\boldsymbol{r}) = \sum_m a_m\psi_m(\boldsymbol{r}), \tag{2.21}$$

where $a_m^\dagger$ (a_m) is the usual raising (lowering) operator. They obey the usual commutation relations:

$$\left[\hat{\Psi}(\boldsymbol{r}), \hat{\Psi}^\dagger(\boldsymbol{r}')\right] = \delta\left(\boldsymbol{r} - \boldsymbol{r}'\right), \left[\hat{\Psi}(\boldsymbol{r}), \hat{\Psi}(\boldsymbol{r}')\right] = \left[\hat{\Psi}^\dagger(\boldsymbol{r}), \hat{\Psi}^\dagger(\boldsymbol{r}')\right] = 0, \tag{2.22}$$

where $\delta\left(\boldsymbol{r}-\boldsymbol{r'}\right)$ is the $3D$ Dirac Delta function. Then we may define an object called the one-body density matrix as:

$$n^{(1)}(\boldsymbol{r},\boldsymbol{r}') = \left\langle \hat{\Psi}^{\dagger}(\boldsymbol{r})\hat{\Psi}(\boldsymbol{r}')\right\rangle . \tag{2.23}$$

This is a very general definition which applies to any system, independently of statistics, and it can be made valid in systems out of equilibrium if the functions depends on time. The object is normalized by integrating the diagonal density as $N = \int n^{(1)}(\boldsymbol{r},\boldsymbol{r})d\boldsymbol{r}$. If the system occupies a pure state described by the N-body wave function $\psi_n(\boldsymbol{r}_1,...,\boldsymbol{r}_N)$ the average given in Eq.(2.23) is defined using the standard rules from quantum mechanics, and we can write:

$$n_n^{(1)}(\boldsymbol{r},\boldsymbol{r}') = N\int d\boldsymbol{r}_2...d\boldsymbol{r}_N\psi_n^*(\boldsymbol{r},\boldsymbol{r}_2,...,\boldsymbol{r}_N)\psi_n(\boldsymbol{r}',\boldsymbol{r}_2,...,\boldsymbol{r}_N), \tag{2.24}$$

where it is assumed that the N-body wave function is normalized to unity. If the system does not occupy the pure state, then if p_n is the probability that the system occupies the pure state n, the average in Eq.(2.23) is defined as

$$n^{(1)}(\boldsymbol{r},\boldsymbol{r}') = \sum_n p_n n_n^{(1)}(\boldsymbol{r},\boldsymbol{r}'). \tag{2.25}$$

The one-body density matrix is a useful way of treating many particle systems, instead of dealing directly with the many-body wave function or the Fock states.

For defining Bose-Einstein condensation it is convenient to write the one-body density matrix as a transformation of its momentum representation. In the case of a homogeneous ideal Bose gas, the spatial dependency of $n^{(1)}$ has to be of the form $s = |\boldsymbol{r}-\boldsymbol{r}'|$ due to to translational symmetry. So

$$n^{(1)}(s) = \frac{1}{V}\int d\boldsymbol{p}n(\boldsymbol{p})e^{i\boldsymbol{p}\cdot\boldsymbol{s}/\hbar}, \tag{2.26}$$

with $n(\boldsymbol{p})$ being the momentum distribution or the diagonal one-body density matrix in the momentum representation. For arbitrary large values of s the behavior of $n^{(1)}(s)$ depends on the momentum distribution $n(\boldsymbol{p})$. This always vanishes for $p\to\infty$, and usually it also vanishes if $p\to 0$ so that $n^{(1)}(s\to\infty)\to 0$. However, if the system has a momentum distribution of the form

$$n(\boldsymbol{p}) = N_0\delta(\boldsymbol{p}) + \tilde{n}(\boldsymbol{p}), \tag{2.27}$$

with $\tilde{n}(\boldsymbol{p}\to 0)\to 0$, we see that

$$n^{(1)}(s\to\infty)\to N_0/N. \tag{2.28}$$

Equation (2.28) implies that the system displays correlations between points that are far a part in space. This phenomenon was called off-diagonal long range order, because it involves off-diagonal components $\boldsymbol{r} \neq \boldsymbol{r}'$ of the one-body density matrix. The quantity N_0/N is called the condensate fraction. In an ideal gas at $T = 0$, $N_0/N = 1$, but the presence of a higher temperature or interaction between atoms can decrease this fraction.

It is easy to show, in this formalism, that the condensate state is a coherent state. Indeed, we can rewrite the sum of Eq.(2.28) separating the ground state from the excited states:

$$\hat{\Psi}(\boldsymbol{r}) = \psi_0(\boldsymbol{r})\hat{a}_0 + \sum_{i\neq 0} \psi_i(\boldsymbol{r})\hat{a}_i. \tag{2.29}$$

Note that in a condensed system the vast majority of the particles will populate the ground state, so we can effectively disregard the second term in Eq.(2.29). Moreover, the action of the operator $\hat{a}_0$ in the Fock state $|N_0\rangle$ is to subtract a particle from the state, i.e, $\hat{a}_0 |N_0\rangle = \sqrt{N_0}\, |N_0 - 1\rangle$. However, since $N_0 >> 1$ this is effectively the same state as $|N_0\rangle$, and thus

$$\hat{\Psi}(\boldsymbol{r}) |N_0\rangle \approx \sqrt{N_0}\psi_0(\boldsymbol{r}) |N_0\rangle \equiv \psi |N_0\rangle . \tag{2.30}$$

Equation (2.30) is the very definition of a coherent state, and it also shows that the field operator $\hat{\psi}(\boldsymbol{r})$ can be treated as a c-number when the system is condensed. The eigenvalue ψ is called the order parameter, or simply wave function of the condensate.

2.2 Interactions

In most situations of interest the atomic cloud is not an ideal gas because the interaction between atoms cannot be neglected. It is possible, in principle, to make the interaction effectively zero, but this is not a very interesting situation because the effects of superfluidity can only be realized in interacting gases. The typical interatomic interaction is complicated and hard to model. It depends on the spin states of the valence electrons coupled to the nuclear angular momentum and has different short and long range behaviors. Luckily, in low energy collisions in alkali atoms, the whole collision process can be characterized by a single parameter: the s-wave scattering length a_s, which we shall abbreviate as the scattering length. Moreover if the molecular bound state of the two atoms has a different magnetic moment than the free atoms state, it is possible to tune the value (and even the sign!) of the scattering length by applying an external magnetic field. This is known as a Fesbach or Fano-Fesbach resonance.

In this section we review the theory of interacting Bose gas. Because the scattering length is about an order of magnitude larger than typical atomic separation in ultracold gases, we will only discuss two body processes as higher orders are strongly suppressed. We begin by arguing that in a low energy collision the wave function must assume an isotropic, asymptotic form that depends only on the scattering length, a_s. The scattering length is related to the phase shifts and the scattering amplitude, and the connection between these quantities will also be discussed. Typically, the many-body wave function varies slowly in space, but there are rapid variations when two atoms are nearby. It is convenient, thus, to use an effective interaction so as to not evaluate short-range correlations in the wave function, "integrating out" the short wavelengths degrees of freedom. This leads us to express the interatomic potential as a delta function with strength proportional to the scattering length, an invaluable tool for latter constructing the Gross-Pitaevskii equation. Finally, the properties of the scattering length depends on the short range part of the interatomic potential, and we provide a qualitative explanation on how this parameter can change with an applied magnetic field. The discussions on this sections draw heavily from references (3, 14–16), studies that should be checked by readers interested in a more complete treatment of the subject.

2.2.1 Scattering theory

We begin with the standard scattering problem: two structureless free atoms approach each other from infinity, scatter and move away to infinity once more. We shall describe the problem with respect to the relative coordinate $\boldsymbol{r}$ between the atoms and the centre of mass coordinate $\boldsymbol{R}$. We shall also assume that the interaction between the atoms is described by the potential $V(\boldsymbol{r})$ depending only in the coordinate $\boldsymbol{r}$ which goes to zero as $r \to \infty$. In this situation the problem factors out into the motion of the center of mass and the relative motion between the atoms. The center of mass motion is a free particle that have a plane wave solution with total momentum given by the sum of the momentum of the individual atoms, and it shall not affect anymore of our discussion.

The wave function for the relative motion, on the other hand, can be written as a superposition of the incoming wave (normalization factor omitted) and an outgoing spherical wave:

$$\psi(\boldsymbol{r}) = e^{i\boldsymbol{k}\cdot\boldsymbol{r}} + \psi_{sc}(\boldsymbol{r}) = e^{ikz} + f(\theta)\frac{e^{i\cdot\boldsymbol{k}'}}{r}, \tag{2.31}$$

where the initial relative wave vector was $\boldsymbol{k}$ and the final one is $\boldsymbol{k}'$ (with $k = k'$) and we have taken $\boldsymbol{k}$ along the z axis due to to the azimutal symmetry of the problem along this direction. The function $\psi_{sc}(\boldsymbol{r})$ represents the scattered wave, it must be a outgoing spherical wave $\frac{e^{i\boldsymbol{k}'\cdot\boldsymbol{r}}}{r}$ with an amplitude $f(\theta)$ called the scattering amplitude that depends only on the polar angle because of the spherical symmetry of the problem and the fact that at infinity the particles are free. What we will also show is that in the low energy limit, $f(\theta) \to -a_s$, the scattering length, so that

$$\psi = 1 - \frac{a}{r} \tag{2.32}$$

is the expected asymptotic behavior of the wave function. We recall the reader that the function $f(\theta)$ fully captures the scattering process, as it determines the cross section: if the differential cross section $d\sigma/d\Omega$ is defined as the current of probability per unit solid angle in the outgoing wave and the current of probability per unit area in the incoming wave, then since the latter is given by $\hbar k/m_r$ (m_r is the system's reduced mass, $m_r \equiv m_1 m_2/(m_1 + m_2)$ for the particles of mass m_1 and m_2) and the former $(\hbar k/m_r)|f(\theta)|^2/r^2$ per unit area or $(\hbar k/m_r)|f(\theta)|^2$ per unit solid angle,

$$\frac{d\sigma}{d\Omega} = |f(\theta)|^2 \, . \tag{2.33}$$

We can expand the wave function as a product of a radial function $R_{k\ell}(r)$ and the Legendre polynomials $P_l(\cos\theta)$:

$$\psi = \sum_{\ell=0}^{\infty} A_\ell P_\ell(\cos\theta) R_{k\ell}(r). \tag{2.34}$$

Due to to the isotropy of the potential $V(r)$,the Legende polynomials are the solution to the Schrödinger equation and the radial equation becomes

$$R''_{k\ell}(r) + \frac{2}{r} R'_{k\ell}(r) + \left[k^2 - \frac{\ell(\ell+1)}{r^2} - \frac{2m_r}{\hbar^2} V(r) \right] R_{k\ell}(r) = 0, \tag{2.35}$$

with the primes denoting derivatives with respect to the argument and ℓ the separation constant which is an integer number. For $r \to \infty$ this equation has the solution (17)

$$R_{k\ell}(r) \approx \frac{1}{kr} \sin\left(kr - \ell\pi/2 + \delta_\ell\right), \tag{2.36}$$

where the constant δ_ℓ is called the phase shift. We can relate δ_ℓ with the scattering amplitude $f(\theta)$ by expanding Eq.(2.31) in Legendre polynomials (see for instance (10)). One finds then that $A_\ell = i^\ell (2\ell+1) e^{i\delta_\ell}$ and

$$f(\theta) = \frac{1}{2ik} \sum_{\ell=0}^{\infty} (2\ell+1)(e^{i2\delta_\ell} - 1) P_\ell(\cos\theta). \tag{2.37}$$

The details of the phase shift, such as its dependency on the momentum, is a function of the central potential $V(\boldsymbol{r})$. However, its low-energy behavior is quite simple if we are dealing with finite range potentials or potentials of the form r^{-n} (the Van der Waals potential that originates from induced dipole interactions between atoms, for instance, vary as r^{-6}) and low energy processes. Specifically, the phase shift vary as $k^{2\ell+1}$

for finite range potentials as $k \to 0$, and the same is true for potentials of the form r^{-n} provided $\ell < (n-3)/2$. If this inequality is not satisfied then $\delta_\ell \sim k^{n-2}$; this can be seen by connecting the wave function behavior in regions where $r < \xi$, $\xi \ll r \ll 1/k$, $kr \sim 1$ and $kr \gg 1$, where ξ is the range of the potential (17). Therefore for potentials that behave as r^{-6} all phase shifts become small as k approaches zero, and the $\ell = 0$ mode is the dominant term. By Eq.(2.37) the corresponding scattering amplitude for $\ell = 0$ is $f = \delta_0/k$, which is angle-independent as stated. Also, if we take the $\ell = 0$ then Eq.(2.36) can be written as

$$R_0 \approx c_1 \frac{\sin kr}{kr} + c_2 \frac{\cos kr}{r} \approx c_1 + \frac{c_2}{r} \tag{2.38}$$

to order kr, the constants c_1 and c_2 being determined by the potential. This shows that

$$\tan \delta_0 = \frac{kc_2}{c_1}, \tag{2.39}$$

and by comparison with Eq.(2.32):

$$\delta_0 = -ka, \tag{2.40}$$

with

$$a = -\left.\frac{c_2}{c_1}\right|_{k\to 0}. \tag{2.41}$$

2.2.2 The effective potential

So far we have established that for low energy collisions, the whole scattering process can be described by a single parameter, the s-wave scattering length. We now proceed to argue that we can also treat the interaction between particles using an effective potential which avoids the evaluation of short wavelength correlations in the many-body wave function.

The starting point is the Schrödinger equation in its integral form for the potential $V(\boldsymbol{r})$ (see, for instance, (10)):

$$\psi(\boldsymbol{r}) = \psi_0(\boldsymbol{r}) - \frac{m_r}{2\pi\hbar^2} \int \frac{e^{ik|\boldsymbol{r}-\boldsymbol{r}'|}}{|\boldsymbol{r}-\boldsymbol{r}'|} V(\boldsymbol{r}')\psi(\boldsymbol{r}')d^3r', \tag{2.42}$$

where $k = \sqrt{2mE}/\hbar$, E is the particle's energy and ψ_0 is the solution of the free particle Schrödinger equation. If $V(\boldsymbol{r}')$ is a finite range potential, i.e, a potential localized at

$\boldsymbol{r}' = 0$, the scattering centre, and we are interested in calculating $\psi(\boldsymbol{r})$ in points far from the scattering centre, we may approximate:

$$|\boldsymbol{r} - \boldsymbol{r}'|^2 \approx r^2 \left(1 - 2\frac{\boldsymbol{r} \cdot \boldsymbol{r}'}{r^2}\right), \tag{2.43}$$

$$|\boldsymbol{r} - \boldsymbol{r}'| \approx r - \hat{r} \cdot \boldsymbol{r}', \tag{2.44}$$

with $\hat{r} = \boldsymbol{r}/r$. Taking $\boldsymbol{k} = k\hat{r}$ and the incoming free wave as $\psi_0(\boldsymbol{r}) = e^{ikz}$, Eq.(2.42) becomes:

$$\psi(\boldsymbol{r}) = e^{ikz} - \frac{m_r}{2\pi\hbar^2}\frac{e^{ikr}}{r} \int e^{-i\boldsymbol{k}\cdot\boldsymbol{r}'} V(\boldsymbol{r}')\psi(\boldsymbol{r}')d^3r'. \tag{2.45}$$

By comparing Eq.(2.45) with Eq.(2.31) it is apparent that

$$f(\theta) = -\frac{m_r}{2\pi\hbar^2} \int e^{-i\boldsymbol{k}\cdot\boldsymbol{r}'} V(\boldsymbol{r}')\psi(\boldsymbol{r}')d^3r'. \tag{2.46}$$

We now make use of the first Born approximation, which is the supposition that the incoming wave function is not substantially altered by the potential $V(\boldsymbol{r})$:

$$\psi(\boldsymbol{r}') \approx \psi_0(\boldsymbol{r}') = e^{ikz'} = e^{i\boldsymbol{k}'\cdot\boldsymbol{r}'}, \tag{2.47}$$

with $\boldsymbol{k}' = k\hat{z}$. Then Eq.(2.46) becomes:

$$f(\theta) = -\frac{m_r}{2\pi\hbar^2} \int e^{-i(\boldsymbol{k}-\boldsymbol{k}')\cdot\boldsymbol{r}'} V(\boldsymbol{r}')d^3r'. \tag{2.48}$$

The final approximation is to note that $\hbar(\boldsymbol{k} - \boldsymbol{k}')$ is essentialy the momentum transfer in the collision, which in the low energy process under consideration, is small. So we may take the exponential factor in the integral to approximately one and write:

$$f(\theta) = -\frac{m_r}{2\pi\hbar^2} \int V(\boldsymbol{r})d^3r. \tag{2.49}$$

We see, then, that Eq.(2.49) gives a result consistent with $f(\theta) = -a$ provided the potential is of the form

$$V(\boldsymbol{r}) = \frac{2\pi\hbar^2 a}{m_r}\delta(\boldsymbol{r}). \tag{2.50}$$

We will only be concerned with gases formed by a single atomic species, in which case $m_r = m/2$, and returning to coordinate space (where $\boldsymbol{r}$ and $\boldsymbol{r}'$ now represents the position of two atoms) we see that

$$V_{\text{eff}}(\boldsymbol{r}, \boldsymbol{r}') = \frac{4\pi\hbar^2 a}{m}\delta(\boldsymbol{r} - \boldsymbol{r}') \equiv g_{3D}\delta(\boldsymbol{r} - \boldsymbol{r}'). \tag{2.51}$$

The parameter g_{3D}, called the interaction parameter, has dimension of energy times volume and is proportional to the scattering length, it is a measure of the strength of the interaction between the atoms. We use the index $3D$ as a remainder that we are dealing with 3 translational degrees of freedom, a situation that will change in future discussions.

2.2.3 Fesbach resonance

The final ingredient in our discussion is an explanation about how magnetic fields can be used to tune the value of the scattering length, that as we have already discussed, determine the physics of the scattering process.

In the previous sections we have always assumed the atoms to have no internal degrees of freedom, such as spin. The basic structure of the theory does not change drastically if we relax this assumption, but the coupling between states with different internal degrees of freedom is precisely that which is responsible for the effect of an external magnetic field over the scattering length.

Let α and β stand for two sets of quantum numbers that label the internal degrees of freedom of the atoms, such as total angular momentum and its projection along a given quantization axis. A particular choice of the numbers α and β is called a *channel*. We may label the initial internal state as $|\alpha\beta\rangle$ and the final state as $|\alpha'\beta'\rangle$. Then, the scattered wave function is given by a generalization of Eq.(2.31):

$$\psi = e^{i\boldsymbol{k}_{\alpha\beta}\cdot\boldsymbol{r}}\,|\alpha\beta\rangle + \sum_{\alpha',\beta'} f_{\alpha\beta}^{\alpha'\beta'}(\boldsymbol{k}_{\alpha\beta},\boldsymbol{k}'_{\alpha'\beta'})\frac{e^{ik'_{\alpha'\beta'}r}}{r}\,|\alpha'\beta'\rangle\,, \tag{2.52}$$

where the second term sums over all possible final states.

The Hamiltonian for the relative motion of the system can be separated as following:

$$H = H_{kin} + H_\alpha + H_\beta + V, \tag{2.53}$$

where $H_{kin} = \boldsymbol{p}^2/2m$ is the kinetic energy operator, V is the atomic potential and $H_{\alpha,\beta}$ the Hamiltonian corresponding to the internal degrees of freedom. The internal eigenvalues are given by $H_{\alpha,\beta}\,|\alpha,\beta\rangle = \epsilon_{\alpha,\beta}\,|\alpha,\beta\rangle$, so the energy associated with the Hamiltonian Eq.(2.53) is:

$$E_{\alpha\beta}(k_{\alpha\beta}) = \frac{\hbar^2 k_{\alpha\beta}^2}{2m_r} + \epsilon_\alpha + \epsilon_\beta. \tag{2.54}$$

Because of energy conservation, the kinetic energy of the particles in the final state

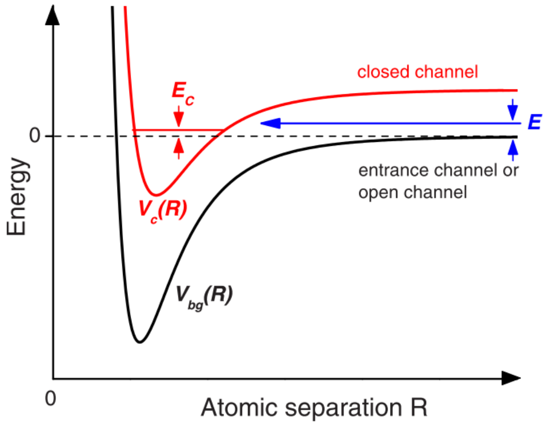

Figure 2 – Schematic potentials as a function of the distance R between the atoms.
Source: CHIN(14)

.

must be

$$\frac{\hbar^2 k'^2_{\alpha\beta}}{2m_r} = \frac{\hbar^2 k^2_{\alpha\beta}}{2m_r} + \epsilon_\alpha + \epsilon_\beta - \epsilon_{\alpha'} - \epsilon_{\beta'}. \tag{2.55}$$

If this situation is attainable, i.e, if $\frac{\hbar^2 k^2_{\alpha\beta}}{2m_r} + \epsilon_\alpha + \epsilon_\beta \leq \epsilon_{\alpha'} + \epsilon_{\beta'}$, the channel $|\alpha'\beta'\rangle$ is called an *open channel*, otherwise it is called a *closed channel*. In a closed channel, the particles do not have enough energy to be at rest at infinity, so this process is energetically forbidden. However, even if this final state is not realizable, a closed channel can be relevant to a scattering process if the potential creates some coupling between the closed and open channels.

Consider two alkali atoms with valence electrons in a s-wave state. The electrons from both atoms can form either a triplet or a singlet configuration. These different configurations can lead to different “bare” interaction potentials between the atoms. For instance, if the electrons are in the triplet state, the total spin is 1, the potential displays a hard core repulsion because the electron clouds overlap, and a long range interaction due to to effects such as dipole induction. In the singlet configuration, however, there’s a deep well originating from the covalent binding between the two electrons. The long range Van der Waals interaction is still present, but it is much weaker at close range than the covalent bonding. In Figure (2) we can see schematically two hypothetical “bare” potentials that could govern the interactions between the atoms in the triplet (red curve, $V_C(R)$) and singlet (black curve, $V_{bg}(R)$) states. Of course, the interaction between atoms actually mix the states, and this mixing is the heart of matter.

We denote the states by $|E\rangle = \phi_{bg}(R, E)\,|bg\rangle$ and $|C\rangle = \phi_C(R)|c\rangle$, where ϕ_{bg},ϕ_C are solutions of Eq.(2.35) with $V(r) = V_{bg}(r)$ and $V(r) = V_C(r)$. The state $|bg\rangle$ is the state of the atoms before scattering and $|C\rangle$ is a bound state in a closed channel with eigenenergy E_c. Typically the closed channel has little influence in the scattering process, but if the energy of the collision approaches the energy of the bound state E_C, a Fesbach resonance occurs. The scattering length then picks up a contribution due to to the closed channel and we can write:

$$a(E) = a_{bg}(E) + a_{res}(E), \tag{2.56}$$

where a_{bg} is the scattering length in a bare potential V_{bg}. The resonant term takes up a standard Breit-Wigner form (14):

$$a_{res}(E) = -\tan^{-1}\left(\frac{\frac{1}{2}\Gamma(E_C)}{E - E_C - \delta E(E_C)}\right). \tag{2.57}$$

In this expression, there is a coupling potential W between the closed and open channel, which determines the width of the resonance $\Gamma(E) = 2\pi \left|\langle C| W(R) |E\rangle\right|^2$ and the shift

$$\delta E(E) = \mathcal{P}\int_{-\infty}^{\infty} \frac{\left|\langle C| W(R) |E'\rangle\right|^2}{E - E'} dE', \tag{2.58}$$

where $\mathcal{P}$ denotes the principal value of the integral.

In particular, if there is a difference in magnetic moment in the formed molecule and the free atoms, the energy of the closed channel relative to the channel energy of the separated atoms can be written as $E_C = \delta\mu(B - B_c)$, and it can be shown that the scattering length assumes the form

$$a(B) = a_{bg}\left(1 - \frac{\Delta}{B - B_0}\right), \tag{2.59}$$

where $\Delta = \Gamma/\delta\mu$ and $B_0 = B_c - \delta E/\delta\mu$. Depending on the direction we approach the resonant value B_0, the scattering length can assume any value $\in (-\infty, \infty)$. In this way, interatomic interaction can be finely controlled and treated with great theoretical simplicity.

2.3 The Gross-Pitaevskii equation

The Gross-Pitaevskii equation is, perhaps, the most important equation in the theory of Bose-Einstein condensation. It is an equation of motion for the order parameter ψ or wave function of the condensate. It is also a zero temperature theory, and therefore only applicable when the condensate fraction is large.

As a starting point, we suppose the system comprises N identical interacting particles of mass M, and write its many-body Hamiltonian as:

$$H = \sum_{i=1}^{N} \left(-\frac{\hbar^2}{2M} \nabla_i^2 + V(\boldsymbol{r}_i) \right) + g_{3D} \sum_{i>j} \delta(\boldsymbol{r}_i - \boldsymbol{r}_j). \tag{2.60}$$

The first term in Eq.(2.60) is the kinetic energy, the second is the potential energy due to the trapping potential and the third is the effective interaction term (see section 2) and involves a sum over all i and j with $i > j$ so as to avoid double countings.

We do like to compute the expected value of this many-body Hamiltonian by supposing the system to have a bosonic wave function:

$$\Psi(\boldsymbol{r}_1, ..., \boldsymbol{r}_N) = \prod_{i=1}^{N} \psi(\boldsymbol{r}_i), \tag{2.61}$$

where the ψ are single-particle wave functions, which we suppose to be normalized to unity $\int |\psi(\boldsymbol{r}_i)|^2 d\boldsymbol{r}_i = 1$. The expected value of Eq.(2.60) is then given by the standard rules of quantum mechanics:

$$E = \sum_{i=1}^{N} \int d\boldsymbol{r}_1 ... d\boldsymbol{r}_N \left[-\frac{\hbar^2}{2M} \psi^*(\boldsymbol{r}_1)...\psi^*(\boldsymbol{r}_N) \nabla_i^2 \psi(\boldsymbol{r}_1)...\psi(\boldsymbol{r}_N) + |\psi(\boldsymbol{r}_1)...\psi(\boldsymbol{r}_N)|^2 V(\boldsymbol{r}_i) \right.$$
$$\left. + g_{3D} \sum_{i>j} |\psi(\boldsymbol{r}_i)|^2 |\psi(\boldsymbol{r}_j)|^2 \delta(\boldsymbol{r}_i - \boldsymbol{r}_j) \prod_{k \neq i,j} |\psi(\boldsymbol{r}_k)|^2 \right] \tag{2.62}$$

The first two terms in Eq.(2.62) are easy to treat: except for the particle coordinate value i all other ψ's can be integrated to unit. This process will happen once for every particle, so there will be N terms that are equal. So the first two terms can be written as:

$$N \int d\boldsymbol{r} \left[-\frac{\hbar^2}{2M} \psi^*(\boldsymbol{r}) \nabla^2 \psi(\boldsymbol{r}) + |\psi(\boldsymbol{r})|^2 V(\boldsymbol{r}) \right]. \tag{2.63}$$

For the last term in Eq.(2.62), the single particle wave functions $|\psi(\boldsymbol{r}_k)|^2$ can be immediately integrated to unity. There are $N(N-1)/2$ ways of choosing pairs of different particles in a sample of N particles with $i > j$, so this term becomes:

$$g_{3D} \frac{N(N-1)}{2} \int d\boldsymbol{r} d\boldsymbol{r}' |\psi(\boldsymbol{r})|^2 |\psi(\boldsymbol{r}')|^2 \delta(\boldsymbol{r} - \boldsymbol{r}') \approx \frac{g_{3D}}{2} N^2 \int d\boldsymbol{r} |\psi(\boldsymbol{r})|^4, \tag{2.64}$$

where we have used the fact that $N >> 1$. Using this results and renormalizing the wave function as $\tilde{\psi}(\boldsymbol{r}) = \sqrt{N} \psi(\boldsymbol{r})$ (and dropping the $\sim$ for clarity) we obtain:

$$E = \int d\boldsymbol{r} \left[-\frac{\hbar^2}{2M} \psi^*(\boldsymbol{r}) \nabla^2 \psi(\boldsymbol{r}) + |\psi(\boldsymbol{r})|^2 V(\boldsymbol{r}) + \frac{g_{3D}}{2} |\psi(\boldsymbol{r})|^4 \right]. \tag{2.65}$$

The (time-independent) Gross-Pitaevskii equation is obtained by demanding the energy E to be stationary under first order variations in the order parameter ϕ^*. More precisely, since we need the number of particles to remain a constant, we demand $E-\mu N$ to be stationary, where μ is at the moment a Lagrange multiplier. So, by demanding $\delta(E-\mu N)=0$ we obtain:

$$\mu\psi(\boldsymbol{r}) = -\frac{\hbar^2}{2M}\nabla^2\psi(\boldsymbol{r}) + V(\boldsymbol{r})\psi(\boldsymbol{r}) + g_{3D}\left|\psi(\boldsymbol{r})\right|^2\psi(\boldsymbol{r}). \tag{2.66}$$

The Lagrange multiplier μ is given by $\partial E/\partial N$, so the eigenvalue of Eq.(2.66) is not the energy but the chemical potential μ.

A time dependent version of Eq.(2.66) can be obtained by an action principle, using the Lagrangian

$$L = \int d\boldsymbol{r}\frac{i\hbar}{2}\left(\psi^*\frac{\partial\psi}{\partial t} - \psi\frac{\partial\psi^*}{\partial t}\right) - E, \tag{2.67}$$

with E given by Eq.(2.65). Then the action principles becomes

$$\delta\int_{t_1}^{t_2} Ldt = 0 \tag{2.68}$$

and the resulting equation for ψ is

$$i\hbar\frac{\partial\psi(\boldsymbol{r},t)}{\partial t} = -\frac{\hbar^2}{2M}\nabla^2\psi(\boldsymbol{r},t) + V(\boldsymbol{r})\psi(\boldsymbol{r},t) + g_{3D}\left|\psi(\boldsymbol{r},t)\right|^2\psi(\boldsymbol{r},t). \tag{2.69}$$

Consistency between Eqs.(2.66) and (2.69) requires that the the wave function evolves in time as $\psi(\boldsymbol{r},t) = e^{-i\mu t/\hbar}\psi(\boldsymbol{r})$. This reflects the fact that microscopically, ψ is the matrix element of the annihilation operator $\hat{\psi}$:

$$\psi(\boldsymbol{r},t) = \langle N-1|\,\hat{\psi}(\boldsymbol{r})\,|N\rangle \propto \exp\left[-i\left(E_N - E_{N-1}\right)t/\hbar\right], \tag{2.70}$$

since the states $|N\rangle$ and $|N-1\rangle$ evolves in time as $e^{-iE_N t/\hbar}$ and $e^{-iE_{N-1}t/\hbar}$ respectively. For large N the difference in energy is essentially $\partial E/\partial N = \mu$.

2.3.1 Solutions for strong and weak interactions

The presence of the mean field non-linear term in the GP equation, Eq.(2.66), means that an analytical solution is in most situations, impossible. There are two very important situations, however, where it is possible to obtain an exact solution as we now proceed to discuss.

The first case is simply when the interaction strength is zero or when its energy scale is much smaller than any other energy relevant to the problem. In this case, we set $g_{3D} = 0$ and Eq.(2.66) becomes a Schrödinger equation with eigenvalue μ. If the trapping potential is of a harmonic oscillator type, $V(r) = \frac{M}{2}\left(\omega_x x^2 + \omega_y y^2 + \omega_z z^2\right)$, then the equation is separable in each coordinate, and the ground state solution of Eq.(2.66) is simply a Gaussian:

$$\psi(x, y, z) = Ae^{-x^2/2a_x^2} e^{-y^2/2a_y^2} e^{-z^2/2a_z^2}, \tag{2.71}$$

where A is a normalization constant ensuring $\int |\psi|^2 d^3r = 1$. The quantities $a_q = (\hbar/M\omega_q)^{1/2}$, $q = x, y, z$ are length scales originating from the binding of the particles by the harmonic oscillator potential.

Another important class of solutions is obtained when the kinetic energy is small comparable to the other energies in the problem, leading to a class of solutions called Thomas-Fermi profiles. Before presenting the solution, we shall elaborate upon the conditions they hold. If R is the typical dimension of a condensate trapped in a harmonic oscillator type potential, then the trap energy is of order $M\omega^2 R^2$, where ω is the trapping frequency. The kinetic energy is of order $\hbar^2/2MR^2$ and the interaction energy is $ng_{3D} \sim Ng_{3D}/R^3$. Due to the R^{-3} dependency of the interaction energy in comparison to the R^{-2} dependency of the kinetic energy, a minimum in the total energy will be a matter of balancing the interaction and trapping energy. This energies are of same order when

$$R \sim d\left(\frac{Na_s}{a_q}\right)^{1/5}, \tag{2.72}$$

with an energy per particle of

$$\frac{E}{N} \sim \hbar\omega\left(\frac{Na_s}{a_q}\right)^{2/5}, \tag{2.73}$$

The quantity Na_s/a_q is a dimensionless measure of the strength of the interaction, and typically it is greater than unity, so that $R > d$. For instance, for $a_s \sim 10$ nm, $a_q \sim 1\,\mu$m and N between 10^4 and 10^6, R/a_q ranges from 2.5 to 6. When R is of order of Eq.(2.72), both the interaction and trapping energies are of order $M\omega^2 R^2$, while the kinetic energy is of order R^{-2}. This means that the ratio of the kinetic energy and the other energies is proportional to $(a_q/Na_s)^{4/5}$; if $\frac{Na_s}{a_q} << 1$, the gas is essentially an ideal gas and the interaction energy can be disregarded, the minimum configuration being essentially attained as a combination of the kinetic and potential energy. On the other hand, if $\frac{Na_s}{a_q} >> 1$ then the interaction energy is dominant and the kinetic energy is negligible.

If $\frac{Na_s}{a_q} >> 1$, therefore, we disregard the kinetic energy in the total energy, which is tantamount to neglecting the Laplacian term in Eq.(2.66). Without this term, the

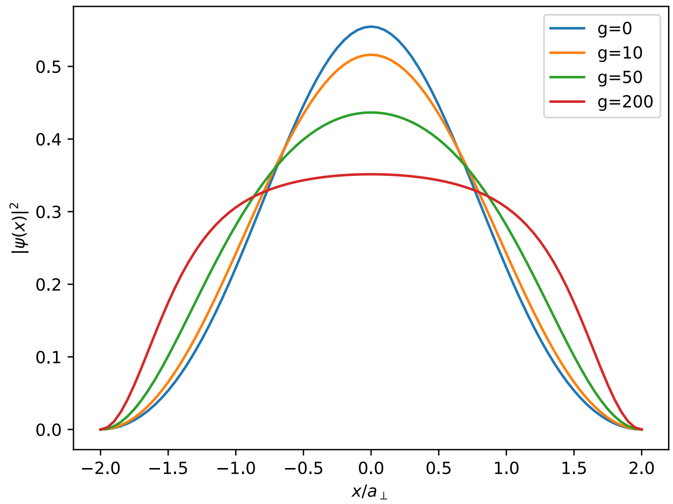

Figure 3 – Numerical $1D$ solutions to Eq.(2.66) for a harmonic oscillator potential, $V(x) = \frac{1}{2}M\omega^2 x^2$, and various adimensionalized interaction strengths parameters g_{3D}. The unit of distance is the harmonic oscillator length scale, $a_\perp = a_q = (\hbar/M\omega)^{1/2}$. For weak interactions the density profile is essentially Gaussian, but as g_{3D} increases the profile resembles a parabola.
Source: By the author.

differential equation becomes an algebraic equation for the particle density $|\psi|^2$, with a solution:

$$n(r) = \frac{\mu - V(r)}{g_{3D}}, \tag{2.74}$$

if $|\psi|^2 \geq 0$ or $n(r) = 0$ otherwise. The roots of Eq.(2.74) gives the boundaries of the gas. If $V(r)$ is a simple harmonic oscillator potential, the resulting radii are of the form:

$$R_i = \frac{1}{\omega_i}\sqrt{\frac{2\mu}{M}}, \tag{2.75}$$

where $i = x, y, z$, and the chemical potential can be expressed in terms of the interaction strength by the normalization of the wave function. The corresponding density profile is an inverted parabola, since it depends quadratically in each of the coordinates x, y and z.

Displayed in Figure 3 are density profiles obtained by solving Eq.(2.69) numerically, for four different values of the interaction strength g_{3D}. The profiles are pretty much Gaussian for small g_{3D}, but they approach parabolas in the central region as g_{3D} increases. Close to the boundaries the solution deviates from the simple Thomas-Fermi solution given by Eq.(2.74) because the kinetic energy becomes relevant to soften the structure of the wave function. Nevertheless, Eq.(2.74) remains a good approximation for the bulk of the condensate.

2.4 Hydrodynamic equations

One very appealing consequence of the time-dependent Gross-Pitaevskii equation, Eq.(2.69), is a relation to the equations of hydrodynamic theory. To see this, we perform a Madelung transform on the wave function, writing:

$$\psi = \sqrt{n(\boldsymbol{r},t)}e^{iS(r,t)}, \tag{2.76}$$

where n and $S \in \mathbb{R}$. If we insert Eq.(2.76) into Eq.(2.69), multiply it by ψ^* and separate the real and imaginary part of the equation, we will obtain two equations. The first one is

$$\frac{\partial n}{\partial t}(\boldsymbol{r},t) + \nabla \cdot (n(\boldsymbol{r},t)\boldsymbol{v}(\boldsymbol{r},t)) = 0, \tag{2.77}$$

with

$$\boldsymbol{v} = \frac{\hbar}{M}\nabla S(\boldsymbol{r},t). \tag{2.78}$$

Equation (2.77) is clearly a continuity equation, where the quantity $n(\boldsymbol{r},t)$ is a density (of particles) and so $\boldsymbol{v}$ must be a velocity. Notice that this is consistent with $\int |\psi|^2 d\boldsymbol{r} = \int n(\boldsymbol{r},t)d\boldsymbol{r} = N$. This interpretation is further substanciated by the second equation, which is:

$$\frac{\partial \boldsymbol{v}(\boldsymbol{r},t)}{\partial t} = -\frac{1}{Mn(\boldsymbol{r},t)}\nabla p - \nabla\left(\frac{v^2(\boldsymbol{r},t)}{2}\right) + \frac{1}{M}\nabla\left(\frac{\hbar^2}{2M\sqrt{n(\boldsymbol{r},t)}}\nabla^2\sqrt{n(\boldsymbol{r},t)}\right) - \frac{1}{M}\nabla V(\boldsymbol{r}). \tag{2.79}$$

The last equation is very similar to a standard equation from hydrodynamics theory, the Euler equation:

$$\frac{\partial \boldsymbol{v}}{\partial t} - \boldsymbol{v} \times (\nabla \times \boldsymbol{v}) = -\frac{1}{Mn}\nabla p - \nabla\left(\frac{v^2}{2}\right) - \frac{1}{M}\nabla V, \tag{2.80}$$

where the zero temperature Gibbs-Duhem relation $dp = nd\mu$ was used to relate the pressure p with the chemical potential. There are two differences between Eq.(2.80) and Eq.(2.79): the absence of the curl term $\boldsymbol{v} \times (\nabla \times \boldsymbol{v})$ in Eq.(2.79) and the presence of a term proportional to $\nabla^2\sqrt{n(\boldsymbol{r},t)}$ in the same equation, which is absent in Eq.(2.80). The first different is due to the fact that in Eq.(2.79), $\boldsymbol{v}$ is related to the gradient of a scalar function, ∇S, as defined in Eq.(2.78), and therefore is a irrotational field in all non-singular points. This last remark is no mere mathematical curiosity, and it shall become very important when we discuss a rotating condensate. As for the term proportional to $\nabla^2\sqrt{n}$, it originates from the fact that the zero-point in a quantum system exerts pressure and possess an energetic content, so that it affects the system's dynamics. It is not relevant in the classical Euler equation, Eq.(2.80), since this is not so in classical mechanics. This term will be disregard in most analysis, because it is usually much smaller than the usual pressure term: if the length scale of variation of the condensate is l, then the pressure term is of order ng_{3D}/Ml (because in an uniform condensate Eq.(2.66) implies $\mu = ng_{3D}$), while the quantum pressure term is of order $\hbar^2/M^2l^3$. Thus quantum pressure dominates in length scales smaller than

$$\xi \sim \frac{\hbar}{\sqrt{Mng_{3D}}} \tag{2.81}$$

which is called the *coherence length*.

A classical fluid, when treated microscopically, is a complicated system with many degrees of freedom. Macroscopically, however, it can be specified by a small set of macroscopic variables: the fluids local density, local temperature and local velocity. At zero temperature, thus, there are four degrees of freedom (three components of the velocity and the local density). The wave function of the condensate is also characterized by four degrees of freedom: the local density of particles and the three components of the gradient of the phase. The mathematical similarity to the classical Euler's equation is due to the fact that Eq.(2.77) is an expression of particle number conservation (as is the classical continuity equation, which is an identical equation), while Eq.(2.79) expresses momentum conservation in the condensate, as the classical Euler equation expresses momentum conservation in the fluid.

2.5 Rotation

In the last section we argued that the condensate can be thought of as a fluid obeying the continuity and Euler equation, with density given by $n = |\psi|^2$ and the velocity given by Eq.(2.78). This last equation has as an immediate consequence that

$$\nabla \times \boldsymbol{v} = 0, \tag{2.82}$$

because $\boldsymbol{v} \sim \nabla S$, the gradient of a scalar function. This means that the phase of the wave function does not change along a closed curve:

$$\Delta S \equiv \oint \nabla S \cdot d\boldsymbol{l} = 0, \tag{2.83}$$

where $\boldsymbol{l}$ is some tangent vector to the closed curve. The fluid is thus irrotational.

A possibility that was overlooked in this argumentation is the presence of singularities in the velocity field. In this case, the phase of the wave function will not necessarily be zero along a closed loop, but it will still need to be some integer multiple of 2π since the wave function must be single-valued. This implies that more generally:

$$\Delta S = \oint \nabla S \cdot d\boldsymbol{l} = 2\pi\nu,\ \nu \in \mathbb{Z}. \tag{2.84}$$

For instance, we can consider a purely azimuthal velocity field. In this case the phase must vary as $e^{i\nu\theta}$, and the velocity field must have a tangential component:

$$v_\theta = \nu \frac{\hbar}{m\rho}, \tag{2.85}$$

where $\rho = \sqrt{x^2 + y^2}$ and x, y are the usual Cartesian coordinates. This velocity field is consistent both with Eq.(2.84) and Eq.(2.78) for $\rho \neq 0$. This would implie that the curl of the velocity field is:

$$\nabla \times \boldsymbol{v} = 2\pi\nu \frac{\hbar}{M} \delta(\rho)\hat{z}, \tag{2.86}$$

where $\hat{z}$ is the unit vector along the z direction, M is the particle's mass and $\delta(\rho)$ is the Dirac delta function peaked at the origin $\rho = 0$.

Note that because $v_\theta \sim 1/\rho$, the kinetic energy will diverge as $\rho \to 0$ unless the density $n \to 0$ rendering the phase undefined at $\rho = 0$. This implies that in this particular example there is really a *line* in the z direction, along which the density vanishes and around which the phase of the condensate changes by $2\pi\nu$. This is called a (charge-ν) *vortex*, a phenomenon already familiar in the context of superconductor physics (18). The connection to the angular momentum is clear: taking z to be the axis of rotation, then in polar coordinates $\hat{L}_z = -i\hbar\frac{\partial}{\partial\theta}$, so

$$\hat{L}_z\psi = \nu\hbar\psi. \tag{2.87}$$

We see, thus, that $\nu\hbar$ is the angular momentum per particle. The quantization of the velocity circulation, in this case, coincides with the quantization of the angular momentum per particle.

If we have more than one vortex the wave function will not be an eigenstate of the angular momentum, except if the condensate's density is symmetric with respect to the axis of rotation. Then $\nu\hbar$ will not necessarily be the angular momentum per particle, and Eq.(2.86) will involve a sum over all poles represented by the delta functions on the right hand side, and the system will contain a *vortex array*, sometimes also called *vortex lattice*.

If one imprints angular momentum to the condensate cloud, the angular momentum per particle increases and therefore one expects the formation of one or more vortices. This is indeed what is experimentally observed (see Figure 4).

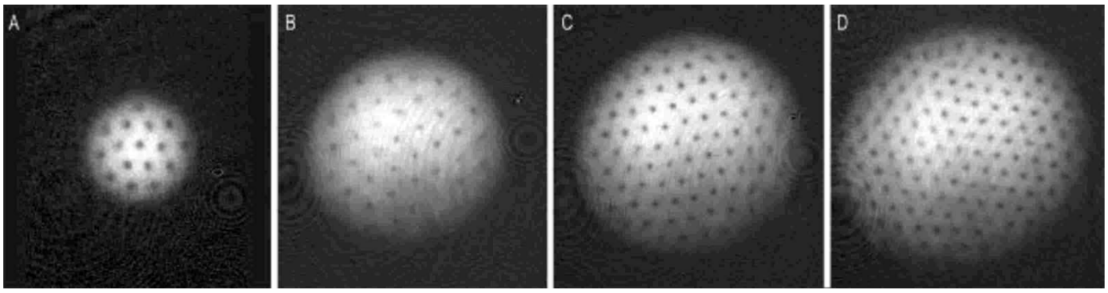

Figure 4 – Observation of vortices lattices in harmonically trapped Bose-Einstein condensates. The number of vortices is approximately 16 (A), 32 (B), 80 (C) and 130 (D). Not only the number of vortices, but also the radius of the cloud increase with increasing angular momentum.
Source: ABO-SHAEER(19)

2.5.1 The structure of a vortex

Let us suppose the wave function to be of the form $\psi = fe^{i\varphi}$, and the condensate to be in its ground state in a uniform medium (except for the presence of the vortex, which we shall align with the z axis). Then by substituting this wave function in the Gross-Pitaevskii equation, Eq.(2.66), and assuming a purely azimuthal velocity field of the form Eq.(2.85), we obtain:

$$-\frac{\hbar^2}{2M}\left[\frac{1}{\rho}\frac{\partial}{\partial\rho}\left(\rho\frac{\partial f}{\partial\rho}\right)\right]+\frac{\hbar^2}{2M\rho^2}\nu^2 f+g_{3D}f^3=\mu f. \tag{2.88}$$

For $\rho \to 0$, the dominant term is the centrifugal term proportional to ν^2, since the interaction term does not depend on ρ and the derivative term goes to 0 because $f \to 0$. On the other hand, for $\rho \to \infty$ the interaction term dominates providing an amplitude $f_0^2 = \mu/g_{3D}$. The length scale ξ that sets the regime where the two terms are comparable is given by

$$\frac{\hbar^2}{2M\xi^2}q^2 f = g_{3D}f^3, \tag{2.89}$$

or recalling that $f^2 = n$, the density of the condensate

$$\xi = \left(\frac{\hbar^2}{2Mng_{3D}}\right)^{1/2}. \tag{2.90}$$

Note that the length scale given by Eq.(2.90) is the same as the one given by Eq.(2.81): it is called the *healing length*, or *coherence length*.

The structure of Eq.(2.88) is greatly simplified if we express length scales in terms of the coherence length $x = \rho/\xi$ and the amplitude of the condensate in terms of its

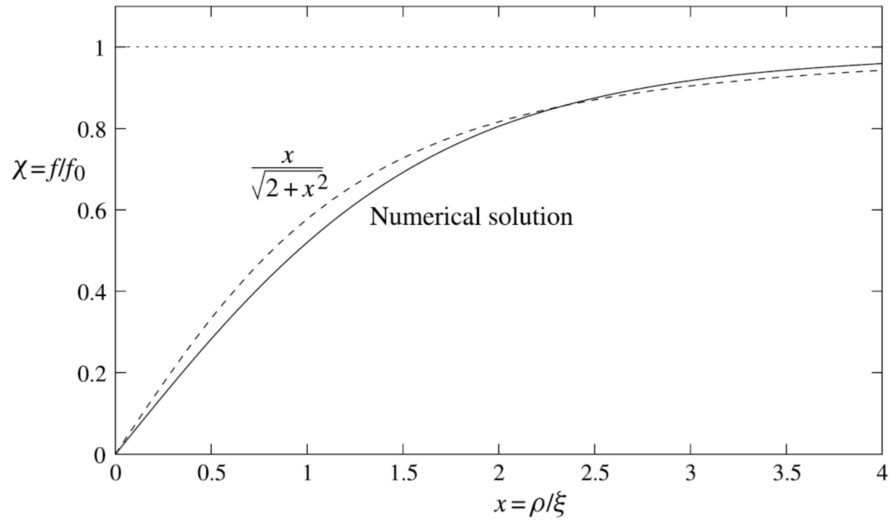

Figure 5 – Numerical solution (solid line) of Eq.(2.91), with $\nu = 1$ and the boundary conditions $\chi(x = 0) = 0$ and $\chi(x \to \infty) = 1$. Also shown is the approximation $\chi = x/\sqrt{2 + x^2}$ in the dashed line.
Source: PETHICK(3)

asymptotic value, $\chi = f/f_0$. The equation then becomes:

$$-\frac{1}{x}\frac{d}{dx}\left(x\frac{d\chi}{dx}\right) + \frac{\nu^2\chi}{x^2} + \chi^3 - \chi = 0. \tag{2.91}$$

This equation can then be solved numerically, and its numerical solution for $\nu = 1$ is shown in Figure 5.

2.5.2 Energy of a vortex

In our previous discussions about the formation of the vortex lattice it was assumed that with increasing angular momentum vortices will always form with a charge 1. So for a total angular momentum per particle of $\nu\hbar$, the system prefers to form ν charge one vortices instead of a single charge ν vortex or any other configuration.

We now argue that this should always be true for a vortex in a uniform condensate. If the condensate is uniform, then in the order parameter $\psi = fe^{i\varphi}$, n is constant, and the velocity field has the azimuthal dependency given by Eq.(2.85). If we take the z axis to be along the vortex, then the total energy per unit length is given by

$$\varepsilon = \int_0^\infty 2\pi\rho d\rho \left[\frac{\hbar^2}{2M}\left(\frac{df}{d\rho}\right)^2 + \frac{\hbar^2\nu^2}{2M}\frac{f^2}{\rho^2} + \frac{g_{3D}}{2}f^4\right]. \tag{2.92}$$

However, this quantity represents the total energy of the condensate. To get the energy of the vortex, we need to subtract from this quantity the energy of a gas in the absence of a vortex. This energy per unit volume is simply $\bar{n}^2 g_{3D}/2$, where $\bar{n} = \alpha/\pi D^2$ is the average density, with α being the number of particles per unit length and D the radius of a cylinder where we suppose the condensate is contained, with $D >> \xi$. This number is given by

$$\alpha = \int_0^D 2\pi\rho d\rho f^2 = \pi D^2 f_0^2 - \int_0^D 2\pi\rho d\rho \left(f_0^2 - f^2\right). \tag{2.93}$$

Hence the energy per unit length in a uniform system is given by

$$\epsilon_0 \approx \frac{1}{2}\pi D^2 f_0^4 g_{3D} - f_0^2 g_{3D} \int_0^D 2\pi\rho d\rho \left(f_0^2 - f^2\right), \tag{2.94}$$

where the last term in α^2 proportional to the square of the integral was disregarded, because it is of order $f_0^4 g_{3D}\xi^4/D^2$, which is negligible since $D >> \xi$. The total energy of the vortex is obtained by subtracting Eq.(2.94) from Eq.(2.92), where we also stop the integration at the cylinder radius D:

$$\varepsilon_V = \int_0^D 2\pi\rho d\rho \left[\frac{\hbar^2}{2M}\left(\frac{df}{d\rho}\right)^2 + \frac{\hbar^2\nu^2}{2M}\frac{f^2}{\rho^2} + \frac{g_{3D}}{2}\left(f_0^2 - f^2\right)^2\right], \tag{2.95}$$

or reescaling the quantities by making $x = \rho/\nu\xi$ and $\chi = f/f_0$:

$$\varepsilon_V = \frac{\pi\hbar^2}{M} n \int_0^{D/\nu\xi} x dx \left[\left(\frac{d\chi}{dx}\right)^2 + \nu^2\frac{\chi^2}{x^2} + \frac{1}{2}\left(1 - \chi^2\right)^2\right]. \tag{2.96}$$

In this last expression, for $\rho >> \xi$ the dominant contribution is the second term, since the condensate approaches uniformity far away from the vortex (so that $d\chi/dx = 0$) and $\chi = 1$ is the asymptotic value of the amplitude. Thus to leading order the energy of the vortex is

$$\varepsilon_V = \pi n \frac{\hbar^2}{M}\nu^2 \ln\left(\frac{D}{\nu\xi}\right). \tag{2.97}$$

Hence in a uniform condensate, the energy depends on the charge of the vortex *squared*, and therefore ν charge 1 vortices are always energetically preferable than a single charge ν vortex.

The argument would change, in principle, if we compute the interaction energy between the vortices. However, one can show that if $\xi << d << D$, this is of order $\nu_1\nu_2 \ln D/d$ with d being the separation between the vortices, and if $d \sim \xi$ it is of order $\nu_1\nu_2 \ln D/\xi$. Hence the total energy of a number of parallel vortices is of order $\sum_i(\nu_i)^2 \ln D/\xi$ if $d \sim \xi$, which is of same order as a charge ν vortex. In a uniform setting, therefore, it is always preferable to have singly charged vortices instead of a multiply quantized vortex.

If the condensate is trapped, however, the preferred configuration depends on the trapping potential. If the trapping is harmonic the proffered configuration is, as in the uniform case, singly quantized vortices. This is easy to see in the Thomas-Fermi regime, where the coherence length ξ is given by

$$\frac{\hbar^2}{2M\xi^2} = \mu = n(0)g_{3D}, \tag{2.98}$$

where $n(0)$ is the density at the center of the condensate and μ is the chemical potential. The chemical potential, on the other hand, is related to the Thomas-Fermi radius R by $\mu = m\omega_\perp^2 R^2/2$ so that combining this results

$$\frac{\xi}{R} = \frac{\hbar\omega_\perp}{2\mu}, \tag{2.99}$$

which shows that $\xi << R$. In this case, the same results as a bulk uniform condensate applies and the kinetic energy is the dominant factor in the vortex energy, which is given by Eq.(2.97) up to a numerical factor in the logarithm. This shows that once more a vortex lattice is energetically preferred as opposed to a single multicharged vortex.

The situation is harder to analyze in the weakly interacting regime. If we consider the rotation to take place around the z axis with angular velocity Ω, then the single particle states are the well known $2D$ harmonic oscillator states $\varphi_{n_r,\nu}$, with eigenvalues:

$$\varepsilon_{\nu,n_r} = \hbar\left(\omega_\perp - \Omega\right)\nu + \hbar\omega_\perp\left(1 + n_r\right), \tag{2.100}$$

where n_r is the radial quantum number, ν is the angular momentum quantum number and $\omega_\perp$ is the trapping frequency in the xy plane. We also suppose that the motion in the z direction is frozen, for instance, by supposing that the potential in z is harmonic with frequency $\omega_z >> \omega_\perp$. We further assume $n_r = 0$ since this is the lowest energy possibility for a fixed angular momentum per particle $\hbar\nu$. If $\Omega < \omega_\perp$ the lowest energy state is given by $\nu = 0$; when $\Omega = \omega_\perp$ all states $\varphi_{0,\nu}$ are degenerate. The presence of the interaction between particles now lifts this degeneracy and the critical frequencies $\Omega_{c\nu}$ split apart and assume values less than $\omega_\perp$.

The general wave function for the $2D$ harmonic oscillator can be written as a linear combination of states $\varphi_{0,\nu}$:

$$\psi(\boldsymbol{r}) = \sum_m c_m \varphi_{0,m}(\boldsymbol{r}). \tag{2.101}$$

with the coefficients of the combination c_m appropriately normalized, $\sum_m c_m = 1$. A single charge ν vortex corresponds to $\psi = \varphi_{0,\nu}$, but numerical as well as analytical analysis suggest that for fixed angular momentum per particle $\nu\hbar$, the system always prefers to form some linear combination of the form of Eq.(2.101) with at least one $c_m \neq 0$ for $m \neq \nu$

(20). As a result and once more, the system prefers to form a lattice of charge 1 vortices than a singly charged ν macrovortex.

However, if the single particle energy given by Eq.(2.100) depends more strongly than linear with angular momentum, this conclusion is no longer valid. In this case, for a positive (albeit possibly very small) interaction strength g_{3D}, the pure state $\psi = \varphi_{0,\nu}$ will have lower energy than any linear combination of the form Eq.(2.101) and the system will therefore occupy a state with a multiply quantized vortex. This result applies whenever the single particle states depends on the angular momentum stronger than linearly (21). The exact angular frequency and interaction strength at which the transition takes place depends on a balance of the potential energy, on one hand, that have its contribution minimized by pure states $\varphi_{0,\nu}$, and the kinetic and interaction term on the other hand, with contributions minimized by linear combinations of the form Eq.(2.101). The potential energy wants a compact condensate, strongly peaked around the potential minimum, and this is best attained for a multiply quantized vortex. The interaction and kinetic energy, on the other hand, wants a voluminous condensate so that the mean atomic separation is large, and a slow, smooth variation of the phase of the wave function, both features best realizable when the angular momentum is distributed over many vortices instead of a singly quantized one.

Figure 6 shows that the behavior of the condensate's vortices when varying the interaction strength $g = g_{3D}$ and the angular frequency Ω for a condensate under a quartic potential $V = \frac{1}{2}m\omega^2 r^2 \left(1 + \lambda \frac{r^2}{{a_\perp}^2}\right)$, where $a_\perp = (\hbar/M\omega)^{1/2}$ is the length scale associated with the harmonic oscillator potential and λ is the quartic term strength. As expected, we see that for a fixed angular speed and increasing interaction, the tendency is for a multiply quantized vortex to break into singly quantized vortices. Note that because of the quartic term, $\Omega/\omega > 1$ is a well confined state of the system. Care must be taken when thinking about this results for very large interactions, since in this regime the wave function is no longer appropriately described by harmonic oscillator wave functions.

2.6 Collective Modes

As a motivation for discussing collective modes, we show in Figure 7 how a vortex is expected to enter the cloud as the angular momentum per particle is increased. We see that as L/N increases, the system loses its rotational symmetry about the z axis, and the surface of the cloud is disturbed. This process gets more dramatic as L/N increases, up to the point where $L/N = 1$ when a vortex is formed at the axis of rotation and the symmetry of the system is restored.

When the angular momentum per particles is less than 1, the system's angular momentum is carried by the perturbation of the cloud structure. These deformations of the cloud structure, which are not restricted to the particular example we just showed, are

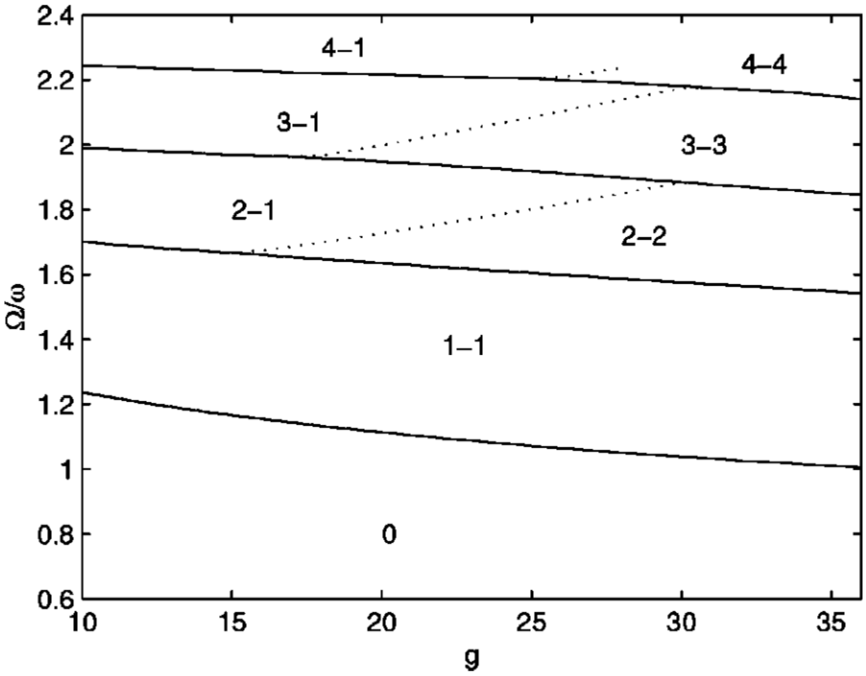

Figure 6 – Phase diagram for a quartically confined two dimensional condensate at angular velocity Ω and interaction parameter $g = g_{3D}$. The region marked by 0 is the state with no vortices, while the region marked by $m - n$ represents that there m circulation quanta distributed over n phase singularities (for instance, $3 - 1$ denotes that there is a singly quantized charge 3 vortex, while $3 - 3$ denotes 3 charge 1 vortices). The lines mark the transition between the different phases and are the result of a energy balance argument.
Source: LUNDH(21)

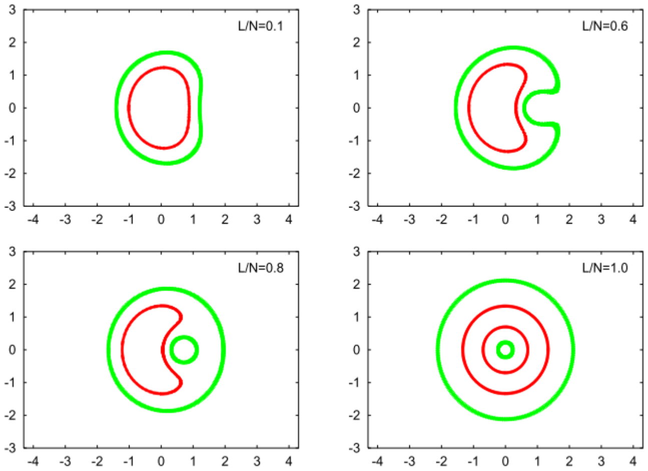

Figure 7 – Lines of constant density for the total angular momentum per particle, $L/N = 0.1, 0.6, 0.8$ and 1 in a plane perpendicular to the z axis. This picture shows how a vortex enters the cloud as the angular momentum per particle is increased.
Source: KAVOULAKIS(20)

called *collective modes*, because they are modes that manifest the many body character of the system, as opposed to single particle modes. Collective modes can be as simple as a radial expansion and contraction, called the breathing or monopole mode, an oscillation of the center of mass motion (called the dipole mode) or rather complex, with eigenstates involving many different orders of the spherical harmonics.

There are many alternatives for the theoretical treatment of this modes. We begin by discussing the modes in a uniform setting. Our methodology will be that of linearizing the hydrodynamics equation; then we proceed to discuss them in a trap. Finally, we introduce another technique for the calculation of the modes, the sum rules technique, which shall be suitable to calculate the frequencies of collective modes in a ring trap.

2.6.1 Uniform condensate

In a uniform medium, we consider the density of the modes to be of the form $n = n_0 + \delta n$, where $n_0 \equiv cte$ is the background density and δn is a small departure from homogeneity caused by the existence of the mode. The velocity field will also be considered small, with no background value, such that $\boldsymbol{v}$ should be treated as a small quantity. Then, by retaining only first order terms in Eqs.(2.77) and (2.79) we obtain:

$$\frac{\partial \delta n}{\partial t} = -\nabla \cdot \left(n_0 \boldsymbol{v}\right), \tag{2.102}$$

$$M \frac{\partial \boldsymbol{v}}{\partial t} = -\nabla \delta \tilde{\mu}, \tag{2.103}$$

where $\delta\tilde{\mu}$ is the linearization of

$$\tilde{\mu} = V + n g_{3D} - \frac{\hbar^2}{2M\sqrt{n}} \nabla^2 \sqrt{n}. \tag{2.104}$$

By taking the time derivative of Eq.(2.102) and using Eq.(2.103) to eliminate the time derivative of the velocity field, we obtain

$$M \frac{\partial^2 \delta n}{\partial t^2} = \nabla \cdot \left(n_0 \nabla \delta \tilde{\mu}\right). \tag{2.105}$$

Now we suppose that the density perturbation δn is a plane wave characterized by a frequency ω and a wave vector $\boldsymbol{k}$, $\delta n = \exp\left(i\boldsymbol{k} \cdot \boldsymbol{r} - i\omega t\right)$. Then we see that

$$\delta\tilde{\mu} = \left(g_{3D} + \frac{\hbar^2 k^2}{4Mn}\right) \delta n \tag{2.106}$$

and Eq.(2.105) becomes

$$M\omega^2 \delta n = \left(n_0 g_{3D} k^2 + \frac{\hbar^2 k^4}{4M}\right) \delta n. \tag{2.107}$$

The physical meaning of Eq.(2.107) is made clear by considering two limiting cases, for large and small k. For large k, the second term is dominant and

$$\hbar\omega = \frac{\hbar^2 k^2}{2M}, \tag{2.108}$$

which is a free particle spectrum. The small wavelength limit of Eq.(2.107) is therefore that of an individual particle with energy $\hbar^2 k^2/2M$.

The other limit, for small k has a frequency given by

$$\omega = ck, \tag{2.109}$$

with $c = \sqrt{n_0 g_{3D}/M}$ being the speed of sound in the condensate. The long wavelength limit is characterized, therefore, by sound waves.

In a general sense we can think that Eq.(2.107) represents the spectrum of a free particle and a mean field correction that is proportional to the interaction strength. The transition between the linear and quadratic behavior takes place when the kinetic energy of a particle $\hbar^2 k^2/2M$ becomes comparable to the interaction energy, $n_0 g_{3D}$, or in other words, when the quantum pressure term and the usual pressure term are roughly equal. This occurs at a length scale given by the coherence length, ξ, which can be related to the sound velocity c using Eq.(2.81): $\xi = \hbar/\sqrt{2}Mc$. So in length scales larger than ξ the atoms move collectively with a sound wave like behavior, while in shorter length scales they move as free particles.

2.6.2 Harmonic oscillator

The hydrodynamic treatment for modes in a condensate trapped in a harmonic oscillator type potential is more complicated because there is an additional length scale in the problem: the spatial extension of the cloud, whereas in the uniform case only the coherence length and the wavelength of the mode are relevant scales. A rather simple result is still possible, however, provided we limit ourselves to condensates with a sufficiently large number of atoms such that the interaction energy is much larger than the kinetic energy. We also need to limit ourselves only to modes that have an extension larger than $\delta = (\hbar\omega/\mu)^{2/3}R/2$, which characterizes the distance from the cloud surface where the kinetic energy becomes important (3), and with spatial variations occurring in length scales larger than the coherence length ξ.

With the above limits taken into consideration, we can neglect the quantum pressure term and thus the quantity $\tilde{\mu}$ becomes $\tilde{\mu} = ng_{3D} + V$, which upon the same linearization scheme used in the last section turns into $\delta\tilde{\mu} = g_{3D}\delta n$. Equation (2.105) still aplies, and applying the time derivative to a plane wave like perturbation of frequency ω we obtain

$$-\omega^2\delta n = \frac{g_{3D}}{M}\left(\nabla n_0 \cdot \nabla\delta n + n_0\nabla^2\delta n\right). \tag{2.110}$$

With the set of assumptions that we had taken for this problem, the background density is a Thomas-Fermi profile, i.e,

$$n_0 = \frac{\mu - V(r)}{g_{3D}}, \tag{2.111}$$

so that Eq.(2.110) becomes

$$\omega^2\delta n = \frac{1}{M}\left[\nabla V \cdot \nabla\delta n - (\mu - V)\,\nabla^2\delta n\right] \tag{2.112}$$

Because of the spherical symmetry of the problem imposed by the potential $V = m\omega_0^2 r^2/2$ it is convenient to use spherical coordinates (r, θ, φ), with θ and φ denoting the polar and azimutal angle, respectively. Moreover, in the Thomas-Fermi approximation the radius of the condensate can be related to the chemical potential by imposing that the radius of the condensate is a hard border, where the density must vanish: $\mu = m\omega_0^2 R^2/2$. Then Eq.(2.112) becomes:

$$\omega^2\delta n = \omega_0^2 r\frac{\partial}{\partial r}\delta n - \frac{\omega_0^2}{2}\left(R^2 - r^2\right)\nabla^2\delta n. \tag{2.113}$$

Again, due to the symmetry of the problem, we can express any density deviation of the background Thomas-Fermi density as the product of a radial function and the spherical harmonics:

$$\delta n = D(r)Y_{\ell m}(\theta, \varphi), \tag{2.114}$$

where as usual ℓ is the quantum number for the total angular momentum and m is its projection along the polar axis. For making contact with known equations, we redefine the radial function as $G(r) = D(r)/r^\ell$ so as to separate the centrifugal barrier term $\ell(\ell+1)/r^2$ in the Laplacian, and reescale the frequency of the mode $\epsilon = \omega^2/\omega_0^2$ and the r coordinate $u = r^2/R^2$. Then Eq.(2.113) turns into

$$u(1-u)G''(u) + \left(\frac{2\ell+3}{2} - \frac{2\ell+5}{2}u\right)G'(u) + \frac{\epsilon - \ell}{2}G(u) = 0, \tag{2.115}$$

where the primes denote r derivatives. This has the same form as the hypergeometric equation for the function $F(\alpha,\beta;\gamma;u)$ (22):

$$u\,(1-u)\,F''(u)+\left[\gamma-(\alpha+\beta+1)\,u\right]F'(u)-\alpha\beta F(u)=0. \tag{2.116}$$

For the function to be regular, either α or β must be a negative integer. Because the function is symmetrical under interchange of α and β, we take $\alpha=-n\in\mathbb{Z}$ without loss of generality, and identify $\beta=\ell+n+3/2$, $\gamma=\ell+3/2$, so that $\epsilon-\ell=2n(\ell+n+3/2)$ or

$$\omega^2=\omega_0^2\left(\ell+3n+2n\ell+2n^2\right). \tag{2.117}$$

We mention two modes which shall be important in this work: the first one is the mode corresponding to $n=1$ and $\ell=0$. This mode is spherically symmetric and its velocity field has the same sign everywhere. The mode therefore must correspond to a radial expansion or contraction of the condensate with frequency $\omega=\sqrt{5}\omega_0$. This is known as the *breathing mode*. Note, however, that this results are valid in three dimensions and for nodeless wave functions.

Another important class of modes are the ones for which $n=0$. This modes with frequency $\omega=\sqrt{\ell}\omega_0$ behave like $\delta n=r^\ell Y_{\ell m}$ and are called *surface modes*, because they are localized more strongly in the surface of the condensate as ℓ increases. A surface mode we shall be particularly interested in this work is the quadrupole mode $\ell=2$, for which

$$\omega=\sqrt{2}\omega_0. \tag{2.118}$$

2.6.3 Sum rules

The hydrodynamic method presented in the previous section is a formidable tool for problems where the background density is sufficiently simple, and the symmetry of the problem allows for further simplifications. In this work, however, we shall be concerned with condensates where the background density is not in a simple Thomas-Fermi regime, and moreover, they will contain one or more vortices. The analytical treatment of this situation would then require us to preserve the term proportional to $\nabla\times\boldsymbol{v}$ in the Euler equation, and include a sum of delta functions in the background density characterizing the position of the vortices. This would yield an analytical solution intractable. We can also consider coarse grain averages, where the density n and the velocity field $\boldsymbol{v}$ are defined as mean values over many vortices, such that the mean velocity field mimicks a rigid body rotation at angular speed Ω, i.e, $\nabla\times\boldsymbol{v}\sim 2\boldsymbol{\Omega}$. For this approach to be successful, however, the number of vortices must be large and the mean vortex separation must also be large.

In order to circumvent these limitations we shall work with the sum rules methodology. This methods allows for the estimation of an upper bound for the frequencies of the collective modes, and the constrain turns into an equality if we choose the correct perturbation operator and the correct number of modes excited by the perturbation to which the system is submitted. This method involves only calculating expected values of the ground state wave function and commutators between the system's Hamiltonian and the perturbation operator. It is, therefore, a very general method.

Our starting point is to the define the strength function for a perturbation operator F and a given frequency ω:

$$S(\omega) \equiv \sum_{k>0} \left|\langle k| F |0\rangle\right|^2 \delta\left(\hbar\omega - \hbar\omega_k\right), \tag{2.119}$$

where $\hbar\omega_k = E_k - E_0$ is the excitation energy of a state with energy E_k relative to the ground state energy E_0, and $|k\rangle$ are the eigenstates of the system's Hamiltonian H. We shall also take the states to be ordered, i.e, $E_0 \leq E_1 \leq ... \leq E_{k-1} \leq E_k \leq ....$ The discrete sum presupposes the system is in a bound state, but changing the sum to an integral generalises it to the continuum. This function encodes how strongly the perturbation operator F excites the system. We also define the p moments of the strength function:

$$m_p \equiv \int_0^\infty S(\omega)\left(\hbar\omega\right)^p d\omega = \sum_{k>0} \left|\langle k| F |0\rangle\right|^2 \left(\hbar\omega_k\right)^p. \tag{2.120}$$

Using the fact that $\hbar\omega_k = E_k - E_0$, we can write

$$\begin{aligned} m_p &= \sum_{k>0} \langle 0| F^\dagger |k\rangle \langle k| F |0\rangle \left(E_k - E_0\right)^p \\ &= \sum_{k>0} \langle 0| F^\dagger |k\rangle \sum_{n=0}^{p} \binom{p}{n} \left(-1\right)^n E_k^n E_0^{n-p} \langle k| F |0\rangle, \end{aligned} \tag{2.121}$$

If the expected value of the perturbation is zero in the ground state, i.e, $\langle 0| F |0\rangle = 0$ and we consider only $p > 0$ moments, since $E_k^n = \langle k| H^n |k\rangle$ we obtain, using the completeness relation $\sum_k |k\rangle \langle k| = 1$:

$$m_p = \langle 0| F^\dagger \left(H - E_0\right)^p F |0\rangle. \tag{2.122}$$

The knowledge of an infinite set of the moments m_p determines completely the strength function Eq.(2.119). In practice, this sum rule approach is useful when the strength function is dominated by a small number of moments which can be calculated, such as in resonant phenomena. It can be easily shown that the moments can be expressed in terms of commutators and anti-commutators between F and H :

$$m_0 = \frac{1}{2} \langle 0| \{F, F\} |0\rangle - \langle 0| F |0\rangle^2, \tag{2.123}$$

$$m_1 = \frac{1}{2} \langle 0| \left[F, [H, F]\right] |0\rangle , \tag{2.124}$$

$$m_2 = \frac{1}{2} \langle 0| \left\{[F, H], [H, F]\right\} |0\rangle , \tag{2.125}$$

$$m_3 = \frac{1}{2} \langle 0| \left[[F, H], [H, [H, F]]\right] |0\rangle . \tag{2.126}$$

The relation between the modes and the frequency of the collective modes depends on how many modes are needed to characterize the strength function. The simplest situation is a two mode picture: since the states are ordered, $\omega_1 \leq \omega_k$ for $k \geq 2$ the following inequality holds:

$$\omega_1^2 \leq \omega_1^2 \frac{|\langle 1| F |0\rangle|^2 + \sum_{k\neq 1} |\langle k| F |0\rangle|^2 \left(\frac{\omega_k}{\omega_1}\right)^3}{|\langle 1| F |0\rangle|^2 + \sum_{k\neq 1} |\langle k| F |0\rangle|^2 \frac{\omega_k}{\omega_1}}. \tag{2.127}$$

In the limit where this is saturated, we obtain:

$$\hbar\omega_0 = \sqrt{m_3/m_1}. \tag{2.128}$$

Equation (2.128) gives exactly the frequency of the collective mode excited by the operator F if that excites exactly a single state of the condensate; otherwise it provides an upper bound for the collective mode frequency.

As a simple example, let us use this method to calculate the frequency of the quadrupole mode in a harmonic oscillator type potential in two dimensions. We suppose the perturbation operator F to be of the form:

$$F = M/2 \sum_i \left\{ \left[(\omega_0 + \delta\omega)^2 - \omega_0^2\right] x_i^2 + \left[(\omega_0 - \delta\omega)^2 - \omega_0^2\right] y_i^2 \right\} \approx M\omega_0\delta\omega \sum_i \left(x_i^2 - y_i^2\right) , \tag{2.129}$$

since the change in the trapping frequency $\delta\omega$ is small. In forming the ratio in Eq.(2.128) any overall numerical factors cancel out, so we can take F to be

$$F = \sum_{i=1}^{N} x_i^2 - y_i^2. \tag{2.130}$$

It is then a straightforward calculation to show that

$$m_1 = \frac{16\hbar^2}{M^2\omega_0^2} \langle U\rangle , \tag{2.131}$$

$$m_3 = \frac{32\hbar^4}{M^2} \left(\langle T\rangle + \langle U\rangle\right) , \tag{2.132}$$

where $\langle T\rangle$ ($\langle U\rangle$) is the expected value of the kinetic (potential) energy. It follows that the frequency of the mode is given by

$$\omega = \omega_0\sqrt{2\left(1+\langle T\rangle / \langle U\rangle\right)}. \tag{2.133}$$

In the Thomas-Fermi limit, the kinetic energy is negligible and $\langle T\rangle / \langle U\rangle << 1$, so the last term in Eq.(2.133) can be disregarded and we obtain $\omega = \omega_0\sqrt{2}$. This is in agreement with the hydrodynamical treatment of the last section, viz. Eq.(2.118). On the other hand, if the two energies contribute equally, then $\langle T\rangle / \langle U\rangle = 1$ and $\omega = 2\omega_0$, which is the expected result for the frequency in this regime (23). We have therefore arrived at the same results from the hydrodynamics method, but without requiring the analytical knowledge of the background density.

The definition of the modes given by Eq.(2.120) is appropriate when we are dealing with non-rotating systems. In the presence of rotation, however, we need to define quantities with positive and negative angular momentum. So the generalized definition of the strength function is:

$$S_{\pm}(\omega) \equiv \sum_n \left|\langle n|\, F_{\pm}\, |0\rangle\right|^2 \delta(\hbar\omega - \hbar\omega_n), \tag{2.134}$$

where F_+ (F_-) is the perturbation operator with angular momentum parallel (anti-parallel) to the rotation. The moments are generalized to:

$$m_p^{\pm} \equiv \int_0^{\infty} d\omega \left(S_+(\omega) \pm S_-(\omega)\right)(\hbar\omega)^p . \tag{2.135}$$

The moments can be cast in a similar form as Eq.(2.122):

$$m_p^{\pm} = \frac{1}{2}\left(\langle 0|\, F_+ \left(H - E_0\right)^p F_-^{\dagger}\, |0\rangle \pm \langle 0|\, F_-^{\dagger}\left(H - E_0\right)^p F_+\, |0\rangle\right)$$

and the first few moments can be shown to be:

$$m_0^- = \langle [F_-, F_+]\rangle , \tag{2.136}$$

$$m_1^+ = \langle [F_-, [H, F_+]]\rangle , \tag{2.137}$$

$$m_2^- = \langle [[F_-, H], [H, F_+]]\rangle . \tag{2.138}$$

In this formalism, it can be shown that in the high interaction limit where the hydrodynamic treatment is applicable, the strength function is exhausted by two modes of frequencies ω_+ and ω_-, which serves as a measurement of the angular momentum because (24):

$$\hbar\left(\omega_+ - \omega_-\right) = m_2^- / m_1^+, \tag{2.139}$$

or

$$\omega_+ - \omega_- = \frac{\langle L_z \rangle}{\langle U \rangle} \omega_0^2, \tag{2.140}$$

so that it can be seen that the splitting of the modes is proportional to the expected value of the angular momentum operator.

3 BUBBLE TRAP

The main objective of this chapter is to explain the scientific value in studying and understanding the bubble trap, and to connect it to the more simple models we shall be working in this thesis, the shifted harmonic oscillator or ring trap and the Mexican Hat Potential. We begin by discussing rapidly rotating condensates: as was already mentioned in a previous chapter, a rotating condensate in a harmonic trap develops one or more vortices in its bulk. When the rotation speed approaches the trapping frequency of the potential, we enter a regime called the rapidly rotating regime. In this situation, centrifugal forces makes the condensate expand in the plane of rotation, while shrinking along the axis of rotation. The system becomes less dense and effectively two dimensional. Since inter vortex spacing scales as $1/\Omega^{1/2}$ (25), eventually the distance between two vortices becomes of order of the coherence length of the system. Moreover, because rotation introduces a centrifugal term in the Hamiltonian, as the rotation increases the system's Hamiltonian approaches the same form as the Hamiltonian of an electron in two dimensions subject to a uniform magnetic field. The physics of this system is described by a set of states called Landau Levels, and when the interaction is small enough we say the system occupies the Lowest Landau Level (LLL). In the LLL, the wave function can be completly described by the product of a gaussian and a polynomial, where the roots in the plane of rotation gives the location of the vortices cores.

However, attaining the LLL is challenging from an experimental point of view when using simple harmonic traps, since as the rotation speed approaches the trapping frequency, the condensate deconfines. Therefore, it is impossible to surpass this limiting trapping frequency. This has prompted research in anharmonic potentials, capable of withstanding ever increasing rotation speeds. One potential which we already discussed that is capable of such an extension is the quartic potential. It was found that as rotation increases beyond the harmonic trapping frequency a hole forms in the center of the condensate confined in the quartic trap, and eventually all vortices in the bulk migrate to the central region, forming a multiply quantized giant vortex. Another potential which can be used to study the rapidly rotating regime is the bubble trap potential, which holds the condensate in the surface of an ellipsoid.

The bubble trap is, however, quite a complicated potential to model. Because of this, we shall adopt two simplified models to study it: the ring or shifted harmonic oscillator potential which is a simplified form of the bubble potential that retains the feature of possessing a hole even in the absence of rotation, and the Mexican Hat potential which might possess a hole at zero rotation, but more generally it has a depletion in the center that eventually forms a hole dynamically provided the rotation rate or the anharmonicity parameter are high enough. These potentials can be related to the bubble trap in some situations. In the presence of a gravitational field, the atoms in a bubble trap pools at the bottom of the ellipsoid. As the rotation speed increases, they climb the wall of the ellipsoid and form a ring. This state of equilibrium can be mapped to the ground state of a ring trap potential. If the atoms at the bottom of the bubble are raised to some height, using light planes for instance, then their configurations will also resemble the ground state of a ring trap potential. Finally, it is possible to use a time-averaged adiabatic potential which, when superimposed to the bubble trap, turns the potential into a ring trap potential. As for the Mexican Hat, it approximates the potential if the gas is strongly confined near the origin of the coordinate system.

3.1 Rapidly rotating condensates

Let us picture a condensate rotating with angular speed Ω around the z axis, trapped by a harmonic oscillator type potential with frequency $\omega_\perp$ in the xy plane and ω_z in the z direction. The many body system Hamiltonian can be written as:

$$H=\sum_{i=1}^{N}\frac{p_i^2}{2M}+\frac{1}{2}M\omega_\perp^2\rho_i^2+\frac{1}{2}M\omega_z^2 z_i^2-\Omega L_{z_i}+\frac{g_{3D}}{2}\sum_{j\neq i}\delta(\boldsymbol{r}_i-\boldsymbol{r}_j), \tag{3.1}$$

where $\rho_i=\sqrt{x_i^2+y_i^2}$ and L_{z_i} is the z component of the angular momentum of the i-th particle. The N particles are assumed to have the same mass M, and to interact via a hard core potential given by the delta function $\delta(\boldsymbol{r}_i-\boldsymbol{r}_j)$ with a strength given by g_{3D}.

Note that with the rotation along the z axis,

$$\frac{p_i^2}{2M}-\Omega L_{z_i}=\frac{(\boldsymbol{p}_i-M\boldsymbol{\Omega}\times\boldsymbol{r}_i)^2}{2M}-\frac{1}{2}M\Omega^2\rho_i^2, \tag{3.2}$$

so that Eq.(3.1) becomes

$$H=\sum_{i=1}^{N}\frac{(\boldsymbol{p}_i-M\boldsymbol{\Omega}\times\boldsymbol{r}_i)^2}{2M}+\frac{1}{2}M\left(\omega_\perp^2-\Omega^2\right)\rho_i^2+\frac{1}{2}M\omega_z^2 z_i^2+g_{3D}\sum_{j\neq i}\delta(\boldsymbol{r}_i-\boldsymbol{r}_j). \tag{3.3}$$

As it can be seen, when $\omega_\perp\to\Omega$, the trapping potential in the xy plane becomes vanishing small. Since the trapping potential in the z direction is unaffected, this has the consequence that the system expands in the plane of rotation, becoming effectively two dimensional. If the frequency in the z direction, ω_z is much higher than the frequency on the plane, $\omega_\perp$, we can think that the dynamics have been frozen out in the z direction and concern ourselves only with motion on the plane. Also, because the system expands the mean particle distance increases and the interaction energy decreases. We can thus focus on the simplified Hamiltonian:

$$H = \sum_{i=1}^{N} \frac{(\boldsymbol{p}_i - M\boldsymbol{\Omega} \times \boldsymbol{r}_i)^2}{2M}, \tag{3.4}$$

which is valid in the limit $\Omega \to \omega_\perp$, $\omega_z >> \omega_\perp$.

Equation (3.4) has the same form of the Hamiltonian seen in a completely phenomenon, the area of the Quantum Hall Effect. (26) It has the same mathematical form of the Hamiltonian of a charge +1 particle in two dimensions moving under the effect of a uniform magnetic field with vector potential $\boldsymbol{A} = M\boldsymbol{\Omega} \times \boldsymbol{r}_i$, which would entail $\boldsymbol{B} = 2M\omega_\perp$. Note, however, that unlike the Quantum Hall physics (QH), this fictitious vector potential has no gauge freedom and the charge is settled to +1, as opposed to $-e$. Because of this, simply quoting the results applicable in the context of QH effect physics would not be appropriate.

The situation can be treated, however, and some results are quite similar. (27) In particular, one very useful results for us are the eigenvalues, that are given by two quantum numbers n_+ and n_-, representing the number of excitations rotating counterclockwise or clockwise to the rotation speed Ω:

$$\epsilon(n_+, n_-) = n_+\hbar(\omega_\perp - \Omega) + n_-\hbar(\omega_\perp + \Omega). \tag{3.5}$$

This shows that when $\Omega \to \omega_\perp$ the energy levels become independent of n_+, and a large degeneration occurs. The index n_- then becomes the Landau-level index, with the different levels separated by a gap of about $2\hbar\omega_\perp$. The structure of the levels, however, is better illustrated with a different set of quantum numbers, $n = n_+ + n_-$ related to the total energy, and $m = n_+ - n_-$ related to the net angular momentum. In terms of this numbers, the energy levels are given by

$$\epsilon(n, m) = n\hbar\omega_\perp - m\hbar\Omega. \tag{3.6}$$

For $\Omega = 0$, the energy depends on n and all levels with different m values are degenerate. Since m ranges from $-n$ to n, there are $2n + 1$ degenerate energy levels. As Ω increases, the degeneracy is lifted, with levels of different angular momentum forming a ladder like structure, as can be seen in the middle panel of Figure 8. Finally, when Ω approaches $\omega_\perp$, the levels agregate into sets separated by a gap of about $2\hbar\omega_\perp$. The energy difference between two levels in the same set is much smaller than the gap between the sets, and indeed the difference is zero if $\Omega = \omega_\perp$. The lowest set of levels in this structure is called the Lowest Landau Level (LLL).

Figure 8 – Energy levels structure as given by Eq.(3.6). Note that m ranges from $-n$ to n, and as the rotation increases the gap between two sets of levels becomes about $2\hbar\omega_{\perp}$.
Source: FETTER(27)

When the system occupies the LLL, its wave function can be described as a (normalized) linear combination of the form:

$$\psi = \sum_m c_m \phi_m, \tag{3.7}$$

where the functions ϕ_m are LLL wave functions:

$$\phi_m = \frac{1}{\sqrt{\pi m! a_{\perp}^{m+1}}} \rho^m e^{im\theta} e^{-\rho^2/2a_{\perp}^2}. \tag{3.8}$$

For the Hamiltonian given by Eq.(3.4), any linear combination of the form Eq.(3.7) results in the system having the same energy. The system is agnostic with respect to its angular momentum. When we take interactions into consideration, their effect is to break this degeneracy and choose some particular combination of Eq.(3.7) (provided the energy scale of interactions is much smaller than the gap between two sucessive Landau levels, so as to avoid contamination of higher levels in the wave function). For finite m, this results in a polynomial in $x + iy$, since $\rho^m e^{im\theta} = (x + iy)^m$, where the roots gives the location of the vortices in the plane of rotation. Remarkably, even though the wave function is the product of a Gaussian and a polynomial, if we average the density profile over the vortices, the resulting function is the inverted-parabola, the Thomas-Fermi profile (28–31).

The linear combination Eq.(3.7) was originally proposed by Ho (32). Another realization from the same work is the connection between the *particle* density and the *vortex* density. To see this, we note that taking the log of Eq.(3.7) multiplied by its complex conjugate results in:

$$\ln n_{LLL}(\rho) = -\frac{\rho^2}{a_{\perp}^2} + 2\sum_j \ln|\boldsymbol{r} - \boldsymbol{r}_j|, \tag{3.9}$$

where $\boldsymbol{r}_j$ is the position of the jth vortex in the plane. The two dimensional Laplacian of this equation yields

$$\nabla^2 \ln n_{LLL}(\rho) = -\frac{4}{a_\perp^2} + 4\pi \sum_j \delta\left(\boldsymbol{r} - \boldsymbol{r}_j\right), \tag{3.10}$$

because $\nabla^2 \ln |\boldsymbol{r} - \boldsymbol{r}_j| = 2\pi\delta\left(\boldsymbol{r} - \boldsymbol{r}_j\right)$. But the sum over the delta function $\delta\left(\boldsymbol{r} - \boldsymbol{r}_j\right)$ is precisely the vortex density n_v, so we can rewrite this last equation as:

$$\nabla^2 \ln n_{LLL}(\rho) = -\frac{4}{a_\perp^2} + 4\pi n_v. \tag{3.11}$$

This remarkable result is interpreted by Ho (32) as a Gauss law for the 2D system, with the charge being the vortices.

Another important consequence of the simple wave function given in Eq.(3.7) is that it can be used as a functional space to obtain variational results of wave functions for a given interaction strength and rotation rate. One simply writes the total energy associated to a function given by Eq.(3.7) and find its minimum with respect to the coefficients c_m, constrained to some total angular momentum m. The coefficients c_m completely determine the polynomial and therefore the wave function. This idea, originally proposed by Butts (7) in the context of a weakly interacting, slowly rotating BEC can also be used in the rapidly rotating regime (29,30,33). The reason this works differs, however: in the context of a slowly rotating and weakly interacting BEC, the wave functions are linear combinations as in Eq.(3.7) because the overall density profile resembles a harmonic oscillator, which is the solution in the laboratory frame for a non-interacting BEC in a harmonic trap. In the rapidly rotating regime, on the other hand, the linear combination Eq.(3.7) works if the interaction is not large enough to excite higher Landau Levels, since the system is expected to populate only the LLL.

3.2 The bubble trap

The rich physics of rapidly rotating condensates is remarkable, and provides great incentive to its experimental verification. There are hard experimental challenges, however, because of the already mentioned fact that in a harmonically trapped BEC, the effective potential goes to zero as $\Omega \to \omega_\perp$, resulting in the deconfinement of the gas (see Eq.(3.3)). This is one of the reasons that lead to the proposals of traps with stronger than harmonic confinements. Other reasons included the vigorous theoretical debate behavior of BECs in lower dimensions (**?**, 34–37), which as we mentioned in a previous chapter, precludes the very existence of a BEC in a homogeneous setting but is possible if the gas is trapped. This discussions lead to the proposal of the bubble trap potential by Garraway and Zobay in a seminal work from 2001 (6). Here we give a basic, schematic explanation

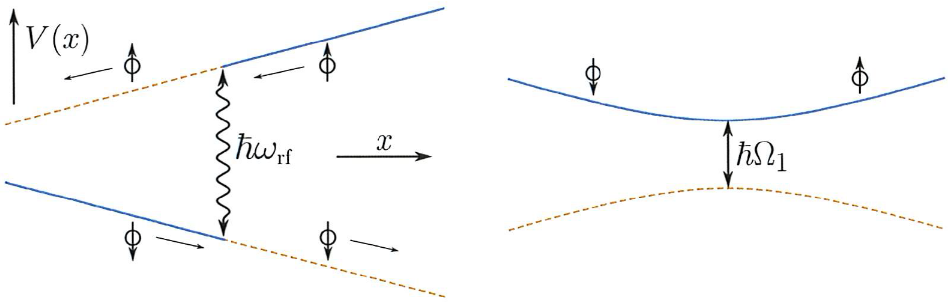

Figure 9 – Schematic representation of the trapping of a particle in an inhomogeneous magnetic field, superimposed to a radiofrequency field ω_{rf}. The left panel show the bare potentials felt by the individual atoms as they move about the resonance: atoms in the blue solid region are attracted toward the resonance and can be trapped, while atoms in the yellow doted region are expelled from the resonance; the right panel shows the dressed or effective potential.
Source: HERVE(38)

about the trap, and briefly discuss how some properties of the condensate, such as the frequencies of the collective modes, are expect to change in this trap.

The basic idea of a bubble trap is to superimpose to a gas with constituents possessing a fine structure, trapped in an inhomogeneous magnetic field, a radiofrequency such that, because of the spatial inhomogeneity of the magnetic field, it will be resonant with the transition frequency of the Zeeman levels at some region of the space. For simplicity, it is useful to imagine a semiclassical picture, imagining the atom as a two-level system labeled by the projection of their angular momentum along a quantization axis $|+\rangle$ and $|-\rangle$, moving through space. If an inhomogeneous magnetic field is applied to this atoms, because of the coupling to magnetic field:

$$H_Z = \frac{g_F \mu_B}{\hbar} \boldsymbol{B} \cdot \hat{\boldsymbol{F}}, \tag{3.12}$$

the up state $|+\rangle$ (assuming $g_F > 0$) will be attracted towards regions of low magnetic fields (called *low-field seekers*), while the down state $|-\rangle$ will be attracted to regions of high magnetic field (such states are called *high-field seekers*). If $g_F < 0$, then the $|-\rangle$ is the low field seeker, while $|+\rangle$ is the high-field seeker. Here, $\hat{\boldsymbol{F}}$ is the total angular momentum operator, $\boldsymbol{B}$ is the magnetic field, g_F is the Landè factor of the state and μ_B is the Bohr magneton. This means that high field seekers will pool around the field's maximum, while low field seekers, accumulates around the field's minimum. But Wing's theorem states that there can be no magnetic field maxima in a current free region, (39) so effectively the high field seekers are expelled from the trap while the low field seekers pool around the minimum.

If we now introduce a magnetic field with frequency ω_{rf} together with the background inhomogeneous magnetic field, we can change this equilibrium position. The basic mechanism to be explored is nuclear magnetic resonance (40), illustrated in Figure 9: low (high) field seekers move around seeking regions of low (high) background magnetic field. Because of this field, there's a splitting of their energy levels proportional to the field's strength. Then there comes a region of space where the applied radiofrequency is equal to the Zeeman splitting between the level, and when the atom passes this region, it changes its state from up to down or vice-versa. But then the potential landscape gets inverted: what was a low field seeker is now a high field seeker, which shall seek regions of high magnetic field and therefore it will be once more attracted towards the region where the radiofrequency is resonant with the background field. Upon passing, its spin is once more inverted and the situation gets repeated. The atoms experience an effective potential with a minimum in the resonant region (see right panel of Figure 9). There are some conditions for this scenario to work: the atoms need to cross the resonance slowly enough in order to their state to follow adiabatically the eigenstates of the Hamiltonian. For a complete description, the reader is referred to (41). In most experiments there are more than two relevant atomic states and the field polarization is also relevant, but the basic ideia is the same as discussed here.

Because the Zeeman splitting is a function of the magnetic field, this region of resonance will be an isomagnetic region. In this situation, it can be shown that the trapped atoms experience a potential landscape given by (41):

$$V(\boldsymbol{r}) = m\hbar\sqrt{\delta^2(\boldsymbol{r}) + \Omega^2(\boldsymbol{r})}, \tag{3.13}$$

where $\delta(\boldsymbol{r})$ is the detuning involving the applied radiofrequency and the local Lamor frequency at a given position $\boldsymbol{r}$, $\Omega(\boldsymbol{r})$ is the local Rabi coupling between the states that are flipped by the radio frequency and m is the spin projection along a given quantization axis. The exact form of δ and Ω depends on the background magnetic field, its polarization and variation in space, as well as the states of the atoms involved. In the absence of gravity, a schematic form which approximates the situation for a Ioffe-Pritchard trap with a linearly polarized RF field is given by:

$$V(\boldsymbol{r}) = \frac{M\omega^2}{2}a^2\sqrt{(r^2 - \Delta)^2 + \Omega^2}, \tag{3.14}$$

where r is the $3D$ spatial radial coordinate in units of $a = (\hbar/M\omega)^{1/2}$ and now Δ and Ω are the dimensionless detuning and Rabi frequency. Another common form is the dressed quadrupole trap for an atomic state with $m = F$, valid for two Helmholtz coils in anti-parallel configuration with a circularly polarized radio frequency, where the potential is

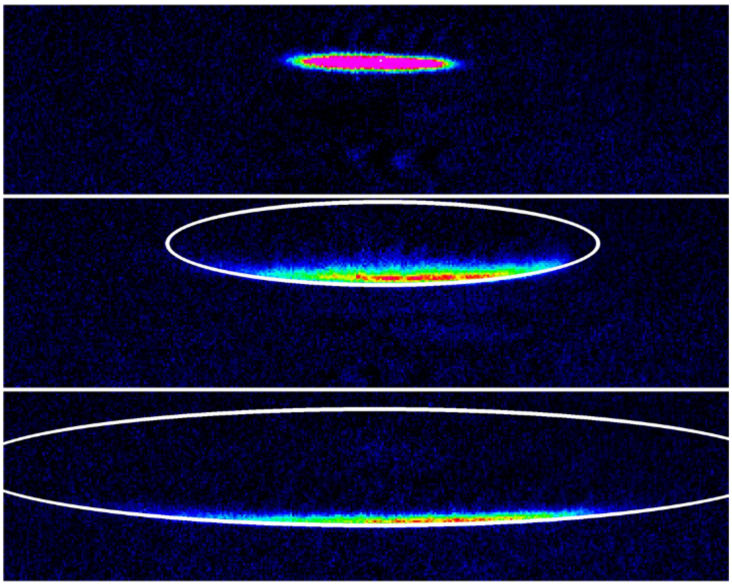

Figure 10 – Absorption images of cold rf-dressed rubidium atoms in the hyperfine state $F = 2$ confined in a bubble trap with addition of gravity. Top panel shows only atoms confined by an Ioffe-Pritchard trap, while middle possesses a rf frequency of 3 MHz and bottom of 8 MHz. The white lines shows the isomagnetic region resonant with the Larmour frequency of the atomic states.
Source: COLOMBE(42)

given by:

$$V(\boldsymbol{r}) = F\hbar\sqrt{(\alpha\ell - \omega_{rf})^2 + \frac{\Omega_0^2}{4}\left[1 - \frac{2z}{\ell}\right]^2}, \tag{3.15}$$

where $\ell = \sqrt{\rho^2 + 4z^2}$ is the distance to the center of the quadrupole trap, α is a parameter proportional to the atomic state's Landè factor and the magnetic field gradient and Ω_0 is the maximum Rabi frequency.

The analysis is substantially the same if we add to the trapping potential a term due to gravity of form Mgz. In this case, the atoms will pool at the bottom of the bubble (see Figure 10). This is in practice the situation in any experiment made in Earth, but the possibility of microgravity experiments aboard the Cold Atom Laboratory at the International Space Station (43) maintains relevant experimental discussions without gravity.

3.3 Ring traps and Mexican Hat from dressed traps

As clean as the expressions given by Eqs.(3.13-3.15) might be, they are still quite hard to tackle in many theoretical problems of interest. Because of that, it is convenient to work with a more practical, although approximated form of the bubble trap potential: the ring trap, or shifted harmonic oscillator, an idea originally proposed by Lesanovsky (44). Rings traps are also interesting by their own merits, such as Sagnac interferometry

(45), studying persistent flows with a pinned vortex (46) and providing a geometry prolific to study solitons (47).

We shall discuss four situations where such a simplification can be achieved with a ring trap potential:

$$V(\boldsymbol{r}) = \frac{1}{2}M\omega_\perp(r - r_0)^2, \tag{3.16}$$

Those situations are a thin shell, a rapidly rotating condensate in a bubble trap with gravity, using light planes to lift the condensate from the bottom of the bubble and time averaged potentials.

Another specially simple way of dealing with the bubble trap potential is to model it as a Mexican Hat potential. Depending of the anharmonicity parameter and interaction strength of the system there is a significant depletion of in the central region of the condensate, further enhanced by centrifugal effects.

3.3.1 Thin shell and Mexican Hat

Consider the situation as given by Eq.(3.14), i.e, an Ioff-Pritchard trap with a linearly polarized RF field in the absence of gravity. If $\Delta = \Omega = 0$ the potential is that of a harmonic oscillator, $V = M\omega^2 a^2 r^2/2$ and the ground state of the system has a spherical volume. On the other hand, for large values of Δ and Ω the ground state is dislocated for finite r values, which implies that the condensate rests in a spherical surface.

The expression Eq.(3.14) has a minimum in $r = \sqrt{\Delta}$. If we restrict ourselves only to points around this minimum value (for instance, by using strong confining frequencies or weakly interacting atoms), then the potential can be expanded around its minimum value as:

$$V(\boldsymbol{r}) = \frac{1}{2}M\omega^2 a^2\Omega + \frac{M\omega^2 a^2}{2}\frac{1}{2}\frac{\Delta}{\Omega}\left(r - \sqrt{\Delta}\right)^2 + O(r - \sqrt{\Delta})^3. \tag{3.17}$$

It is therefore clear that up to a constant term, the potential close to the minimum $r = \sqrt{\Delta}$ can be approximated by the shifted harmonic oscillator potential

$$V_{\mathrm{SHO}}(\boldsymbol{r}) = \frac{1}{2}M\omega_{\mathrm{SHO}}^2(r - r_0)^2, \tag{3.18}$$

with $r_0 = \sqrt{\Delta}$ and $\omega_{\mathrm{SHO}} = \sqrt{\Delta/2\Omega}\omega$. This can be clearly seen in Figure 11, where the shifed harmonic oscillator trap potential added to the constant term $\frac{1}{2}M\omega^2 a^2\Omega$ is plotted together with Eq.(3.14) for $\sqrt{\Delta} = \sqrt{\Omega} = 3$.

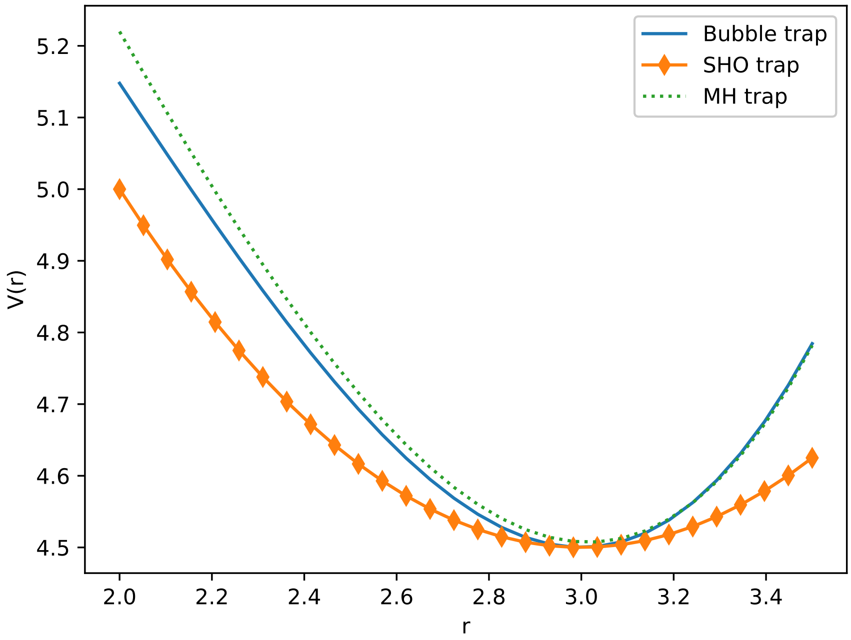

Figure 11 – Comparison of the bubble trap, the SHO trap approximation and the MH approximation, for $r_0 = \sqrt{\Delta} = 3$, $\lambda = 0.05$ and $\Delta = \Omega$ in Eq.(3.14). Added to the SHO is the zero value of the expansion of the bubble trap around the minimum, which yields a constant term of 9/2, while to the MH we added the constant value of 6.78. Notice that the values of λ and ρ_0 are well related by Eq.(3.21). We used harmonic oscillator units (a for distance and $\hbar\omega$ for energy).
Source: By the author.

On the other hand, by expanding Eq.(3.14) around $r = 0$ we obtain, apart from a constant term:

$$V\left(\boldsymbol{r}\right) = -\frac{M}{2}\frac{\omega^2\Delta}{\sqrt{\Delta^2+\Omega^2}}a^2r^2 + \frac{M}{2}\frac{\omega^2\Delta}{\sqrt{\Delta^2+\Omega^2}}\frac{\Omega^2}{2\Delta\left(\Delta^2+\Omega^2\right)}a^2r^4 + O\left(r^6\right) \tag{3.19}$$

then

$$V_{\mathrm{MH}}(\boldsymbol{r}) = -\frac{1}{2}M\omega_{\mathrm{MH}}^2r^2 + \frac{1}{2}M\omega_{\mathrm{MH}}^2\lambda r^4, \tag{3.20}$$

with $\omega_{\mathrm{MH}}^2 \equiv \omega^2\Delta/\sqrt{\Delta^2+\Omega^2}$ being the frequency of the Mexican Hat potential and $\lambda \equiv \Omega^2/2\Delta\left(\Delta^2+\Omega^2\right)$ being the anarmonicity parameter. It is important to notice that the two different potentials can be related: for a thin annulus, when the condensate is strongly confined to the potential minimum at r_0, the relation between the radius of the shifted

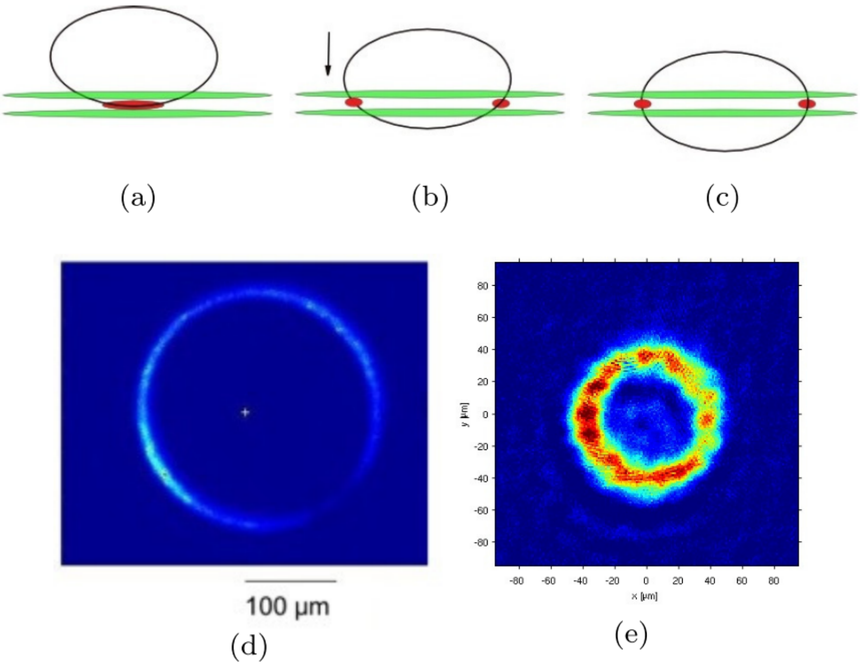

(a) (b) (c)

(d) (e)

Figure 12 – Top row: schematic representation of the loading of a ring trap, strating from atoms pooling at the bottom of a dressed quadrupole trap. (a) Two light planes (in green) are switched on in order to confine the initial oblate atomic cloud (in red) between the two light maxima. (b) The light planes are then dislocated so that the atoms occupy some fixed height (or alternatively, the resonant surface is translated downwards while the light planes stay fixed). (c) The maximum ring radius and trapping frequency is obtained when the atoms occupy the equatorial plane of the ellipsoid. Bottom row: atoms confined in the ring trap. (d) Radius 130 μm obtained for a low magnetic gradient of $b = 55.4$ G $\cdot$ cm^{-1} amd a rf frequency of 1 MHz. (e) Radius 40 μm associated with the larger gradient $b = 218$ G $\cdot$ cm^{-1} and a dressing rf frequency of 600 kHz.
Source: PERRIN(41)

harmonic oscillator and the anarmonicity parameter from the MH is (48):

$$r_0 = a/\sqrt{2\lambda} \tag{3.21}$$

3.3.2 Light sheets

Another way of generating an annular condensate is to start from a quadrupolar magnetic field dressed with a circularly polarized rf field (as in Eq.(3.15)) and gravity, and then intersect this trap with two light sheets detuned from the resonant frequency. The atoms will get trapped between the planes, and if the planes are then lifted to some finite z value, the resulting configuration will appear as a ring (see Figure 12). For definiteness let us consider the atoms are lifted until the equator, but any other height would be possible.

If this procedure is followed, the radius of the ring will be given by the radius of the ellipsoid, which in turn is characterized by the radio frequency and the static trap. For instance, if the trap is a quadrupole field generated by two Helmholtz coils with anti-parallel currents:

$$\boldsymbol{B}_0(\boldsymbol{r}) = b\left(x\boldsymbol{e}_x + y\boldsymbol{e}_y - 2z\boldsymbol{e}_z\right), \tag{3.22}$$

the local Larmour frequency would be

$$\omega_0(\boldsymbol{r}) = \alpha\sqrt{x^2 + y^2 + 4z^2}, \tag{3.23}$$

where (x, y, z) are the Cartesian coordinates, b is the magnetic field gradient, $\alpha = |g_F|\,\mu_B b/\hbar$ (g_F is the Landè factor of the atomic state, μ_B the Bohr magneton) and $(\boldsymbol{e}_x, \boldsymbol{e}_y, \boldsymbol{e}_z)$ are unit vectors along the three Cartesian axis. The ellipsoid would then be the surface

$$x^2 + y^2 + 4z^2 = r_0^2, \tag{3.24}$$

with $r_0 = \omega_{rf}/\alpha$. So as stated, the radius of the ring could be adjusted by changing the radio frequency and the magnetic field.

If the atoms are at the equator, the radial confinement is purely due to the adiabatic potential, and it can be related to the bubble parameters by (41):

$$\omega_r = \alpha\sqrt{\frac{F\hbar}{M\Omega_0}}, \tag{3.25}$$

while the vertical confining frequency depends upon the light sheets parameters. It is also important to use a circularly polarized rf field, so as not to break the circular symmetry of the trap. It is, however, possible to use linearly polarized light so as to induce rotation in the ring.

3.3.3 Time averaged adiabatic potentials

The quadrupole field given by Eq.(3.22) has a global minimum at $\boldsymbol{r} = 0$. As was already discussed, the low-field seekers will be driven to that position. Since the Zeeman levels are splitted accordingly to the strength of the magnetic field, they will be progressively less spaced as the atoms approach the minimum, and therefore any small instability in the atoms can change the atomic state, promoting a low-field seeker to a high-field seeker and leading to losses from the trap.

A way to circumvent this problem is to introduce a bias oscillating field component to the static magnetic field, generating an oscillation of the field's minimum. If the frequency of this bias field is high enough, the atoms experience a time averaged potential,

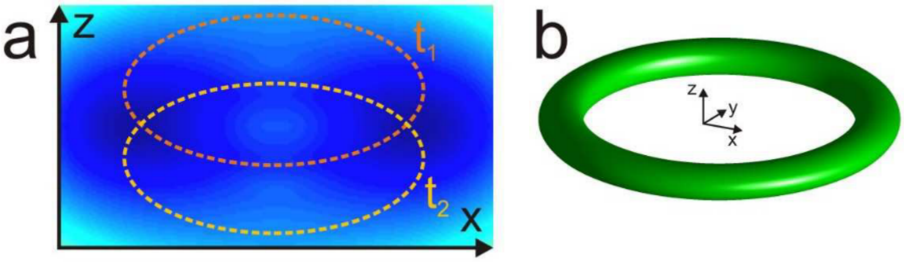

Figure 13 – Generation of a ring trap from a TAAP. (a) Density plot of the TAAP in the xz-plane. The dashed line displays the equipotential of the potential minimum at different times t_1 and t_2. Color intensity is the resulting average in time. (b) A 3D visualisation of an equipotential shown in (a).
Source: LESANOVSKY(44)

where the minimum value of the (time averaged) potential is now finite. This technique is called Time Orbiting Potential, or TOP trap. The same idea can be used to create a ring trap from an adiabatic trap, a technique originally suggested by Lesanovsky and von Klitzing (44), with the caveat that the oscillating field cannot change fast enough in order to promote non-adiabatic transitions. This combined idea is called time averaged adiabatic potential, or TAAP, and a rough representation can be seen in Figure 13.

To see this idea more concretely, let us start by adding to the static magnetic field Eq.(3.22) a oscillating field with frequency ω_m in the z direction:

$$\boldsymbol{B}_0(\boldsymbol{r},t) = b\left(x\boldsymbol{e}_x + y\boldsymbol{e}_y - 2z\boldsymbol{e}_z\right) + B_m \sin\left(\omega_m t\right)\boldsymbol{e}_z. \tag{3.26}$$

The immediate consequence of such an addition is that the center of the quadrupole now oscillates in time. Its coordinate is $(0,0,z_0(t))$ with

$$z_0(t) = \frac{B_m}{2b}\sin\left(\omega_m t\right). \tag{3.27}$$

This oscillation of the resonant surface implies that the Larmor frequency is now also time dependent, Eq.(3.23) now becoming

$$\omega_0(\rho,z,t) = \alpha\sqrt{\rho^2 + 4\left[z - z_0(t)\right]^2}. \tag{3.28}$$

This system will interact with a radio frequency, that we shall take to be time dependent:

$$\boldsymbol{B}_1(t) = B_1(t)\cos\left(\omega_{\mathrm{rf}}(t)t\right)\boldsymbol{e}_z. \tag{3.29}$$

In this way, Eq.(3.13) can be written as

$$V = F\hbar\sqrt{\left[\omega_0(\rho,z,t) - \omega_{\mathrm{rf}}(t)\right]^2 + \Omega_1\left(\rho,z,t\right)^2}. \tag{3.30}$$

The local Rabi frequency can be calculated for the linear polarization of the rf field, and it is given by (41):

$$\Omega_1\left(\rho, z, t\right) = \Omega_0(t)\sqrt{1 - u_z(\rho, z, t)} \tag{3.31}$$

where $\Omega_0(t) = |g_F \mu_B B_1(t)/2\hbar|$ is the maximum Rabi frequency and u_z is the projection of the static field along the polarization:

$$u_z(\rho, z, t) = \frac{\boldsymbol{B}_0 \cdot \boldsymbol{e}_z}{|\boldsymbol{B}_0|} = -\frac{2\left[z - z_0(t)\right]}{\sqrt{\rho + 4\left[z - z_0(t)\right]^2}}. \tag{3.32}$$

Our objective now is to form a ring at $\rho = \rho_0$ and $z = 0$. Because of the bias field, the potential in Eq.(3.30) does not yield a stable isomagnetic region, since the circle at $(\rho_0, 0)$ oscillates with a frequency $2\omega_m$ due to the modulation in ω_0. This needs to be compensated by engeneering the rf field so that for all t, $\omega_0(\rho, z, t) - \omega_{\mathrm{rf}}(t) = 0$. This implies that:

$$\omega_{\mathrm{rf}}(t) = \alpha\sqrt{\rho_0^2 + 4z_0^2(t)}, \tag{3.33}$$

or defining the lowest rf frequency as $\omega_{\mathrm{rf}}^0 \equiv \alpha\rho_0$

$$\omega_{\mathrm{rf}}(t) = \omega_{\mathrm{rf}}^0\sqrt{1 - \beta_m^2 \sin^2(\omega_m t)}, \tag{3.34}$$

where $\beta_m = B_m/(b\rho_0)$ is the scale of vertical shaking relative to the size of the resonance surface.

The other parameter that needs modulation is the rf field amplitude, B_1. As the center of the surface oscilates and the quadrupole field leaves the plane $z = 0$, there is an angle of the magnetic field with respect to this plane which causes variations of the Rabi frequency given in Eq.(3.31). In $z = 0$, the Rabi frequency around the ring circle will oscillate as

$$\Omega_1(\rho_0, 0, t) = \frac{\Omega_0(t)}{\sqrt{1 + \beta_m^2 \sin^2(\omega_m t)}}. \tag{3.35}$$

We can prevent such an oscillation if we modulate the rf field amplitude as

$$B_1 \to B_1\sqrt{1 + \beta_m^2 \sin^2(\omega_m t)}, \tag{3.36}$$

in this way fixing the Rabi frequency around the trapping circle at $\Omega_0 = \left|g_F \mu_B B_1\right| / (2\hbar)$. The full Rabi frequency is then given by

$$\Omega_1(\rho, z, t) = \Omega_0 \frac{(\rho/\rho_0)\sqrt{1+\beta_m^2 \sin^2(\omega_m t)}}{\sqrt{(\rho/\rho_0)^2 + \left[2z/\rho_0 - \beta_m \sin^2(\omega_m t)\right]^2}}. \tag{3.37}$$

This choices guarantee that there will be a ring at $(\rho_0, 0)$. To verify its stability, we need to expand the potential Eq.(3.30) around this point and then take its time average. Let thus $\rho = \rho_0 + \Delta\rho$, for a small $\Delta\rho$. For the first part of the square root, we obtain:

$$\omega_0\left(\rho, z=0, t\right) - \omega_{\mathrm{rf}}(t) = \omega_{\mathrm{rf}}^0 \frac{\Delta\rho}{\rho_0} \frac{1}{\sqrt{1+\beta_m^2 \sin^2(\omega_m t)}}, \tag{3.38}$$

which is only need in first order in $\Delta\rho$ to obtain a second order term in V. The potential then becomes:

$$V(\rho+\Delta\rho, z, t) \approx F\hbar\Omega_0 \left\{1 + \frac{1}{2}\left(\frac{\omega_{\mathrm{rf}}^0}{\Omega_0}\right)^2 \left(\frac{\Delta\rho}{\rho_0}\right)^2 \frac{1}{1+\beta_m^2 \sin^2(\omega_m t)} + \ldots\right\}, \tag{3.39}$$

where we have neglected terms from the expansion of Eq.(3.37), because they are smaller by a factor of $\left(\Omega_0/\omega_{\mathrm{rf}}^0\right)^2$. The first order term coming from the spatial dependence of Eq.(3.37) simply shifts slightly the radial location of the ring trap.

We now take the time average using the fact that

$$\int_0^{2\pi/\omega_m} \frac{1}{1+\beta_m^2 \sin^2(\omega_m t)} dt = \frac{1}{\sqrt{1+\beta_m^2}} \tag{3.40}$$

and obtain

$$V(\rho_0+\Delta\rho, z) \approx F\hbar\Omega_0 \left\{1 + \frac{1}{2}\left(\frac{\omega_{\mathrm{rf}}^0}{\Omega_0}\right)^2 \left(\frac{\Delta\rho}{\rho_0}\right)^2 \frac{1}{\sqrt{1+\beta_m^2}}\right\}, \tag{3.41}$$

or in other terms,

$$V \approx V_0 + \frac{1}{2} M \omega_{ring}^2 \left(\rho - \rho_0\right)^2, \tag{3.42}$$

with $V_0 = F\hbar\Omega_0$ being the potential at the bottom of the ring trap, and

$$\omega_{ring} = \omega_r \left(1+\beta_m^2\right)^{-1/4}, \tag{3.43}$$

with ω_r being the standard transverse frequency given by Eq.(3.25).

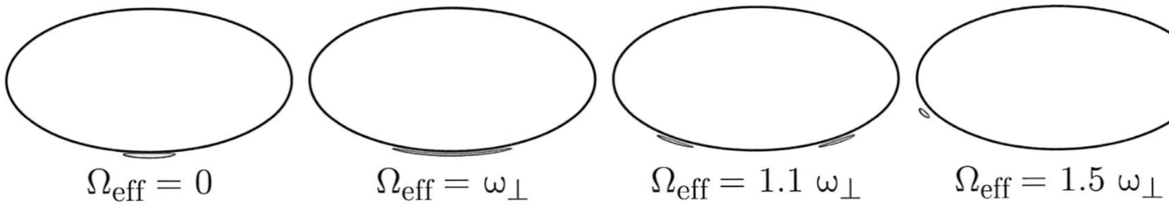

Figure 14 – The effects of rotation in the equilibrium density of the condensate at the bottom of a bubble trap. As the angular speed Ω_{eff} increases from 0 to $1.5\omega_\perp$ the condensate, driven by the centrifugal effects of the rotation, "climbs" the isomagnetic surface and rests at a finite z value, implying that the equilibrium position for ρ is also non-zero.
Source: HERVE(38)

3.3.4 Rapidly rotating condensates

Yet another way to relate the ring trap to the bubble is to consider a rapidly rotating condensate in a quadrupole trap bubble subject to a gravitational field. Without rotation, because of the gravitational sag, the condensate rests at the bottom of the bubble. Around the equilibrium position to potential is locally harmonic, with a trapping frequency given by (38):

$$\omega_\perp = \sqrt{\frac{g}{2r_0}}\left[1 - \frac{2F\hbar\Omega_0}{Mgr_0}\right]^{1/2}, \tag{3.44}$$

where g is the gravitational field acceleration, r_b is the radius of the isomagnetic surface given by Eq.(3.24) and Ω_0 is the maximum Rabi frequency.

When $\Omega > \omega_\perp$ the condensate no longer rests at the point $\rho = 0$ and $z = 0$ because due to the centrifugal forces it is propelled against the magnetic surface, and therefore it "climbs" the surface coming to rest at some finite ρ and z. The new equilibrium position, supposing the atoms to be very tightly confined to the resonant surface, can be found to be:

$$r_{eq} = r_0\sqrt{1 - \omega_\perp^4/\Omega_{rot}^4}, \tag{3.45}$$

where Ω_{rot} is the angular speed. While it is possible to obtain an expression for the trapping frequency when $\Omega_{rot} < \omega_\perp$, it is not a trivial matter to do so when $\Omega_{rot} > \omega_\perp$ (49).

4 RESULTS

In this chapter we further elaborate the methodology in our study and present our main results. We shall employ harmonic oscillators units: supposing the harmonic oscillator trapping potential in the xy plane to be

$$V = \frac{1}{2} M\omega_0^2\rho^2, \tag{4.1}$$

where M is the mass of the atoms, ω_0 is the trapping frequency and $\rho = \sqrt{x^2 + y^2}$, then we choose $a = (\hbar/M\omega_0)^{1/2}$ as unit of distance, ω^{-1} as unit of time, $\hbar\omega_0$ as a unit of energy (and consequently, $\hbar$ as unit of angular momentum).

4.1 Phase diagram

To study how the total charge and distribution of vortices change when we explore the (Ω, g_{2D}) parameter space, we employed numerical and analytical techniques. The numerical method is straight forward: with propagation in imaginary time we compute the ground state of a condensate in the rotating frame for a given Ω and g_{2D}, and from this wave function extract the relevant information about the vortices. However, in practice we found that states with different total charge and vortex distribution differs very little in energy, so that often the convergence of the numerical methods to a given ground state depends on the initial wave function used. It is therefore crucial that we can find alternatives for informing our initial choice of the wave function used as input in the numerical methods.

Analytically, we suppose the wave function to be in a linear combination of the form

$$\psi = \sum_m c_m\phi_m, \tag{4.2}$$

$$\sum_m |c_m|^2 = 1, \tag{4.3}$$

where the functions ϕ_m represents a state with total angular momentum m and its exact dependency on the coordinates are a function of the potential. To calculate the boundary between states with different total charge we suppose the system to be in a pure state, i.e, $c_{m_0} = 1$ for some m_0 and $c_m = 0$ for all $m \neq m_0$. Then the boundary is obtained by computing the total energy E_{m_0} and comparing it to E_{m_0+1}, resulting in a equation for Ω as a function of g_{2D}.

Transition to the vortex lattice states, in the order hand, is determined assuming that there's some value m_0 with $c_{m_0} \approx 1$ and two other states numbered m_1 and m_2 that are slightly populated. A stability matrix formed by the second derivative of the energy with respect to the coefficients is then constructed and its eigenvalues determines if a given region of the parameter space is stable for the state m_0 or if it will decay in a vortex lattice configuration.

Finally, the variational technique also supposes the system to occupy some combination of the form Eq.(4.2), but now we minimize numerically the energy in the rotating frame for a given Ω and g_{2D} with respect to the coefficients c_m.

4.1.1 Mexican Hat

For the Mexican Hat potential,

$$V = \frac{1}{2}\left(-\rho^2 + \lambda\rho^4\right), \tag{4.4}$$

the functions ϕ_m in Eq.(4.2) are of the form:

$$\phi_m(\rho, \varphi) = \frac{\rho^m}{\sqrt{\pi m!}} e^{im\varphi} e^{-\rho^2/2}. \tag{4.5}$$

With these functions it is easy to calculate the total energy:

$$E = \int d^2r \left[\frac{1}{2}\left|\nabla\psi\right|^2 + V\left|\psi\right|^2 + \frac{g_{2D}}{2}\left|\psi\right|^4 - \Omega\psi^* L_z\psi\right], \tag{4.6}$$

where L_z is the angular momentum operator in the z axis, that is also taken as the axis of quantization. We calculate it for a pure state m as:

$$E_m = \frac{1}{2}\lambda\left(1+m\right)\left(2+m\right) + \frac{g_{2D}}{4\pi}\frac{(2m)!}{2^{2m}\left(m!\right)^2} - m\Omega, \tag{4.7}$$

and when we compare it to E_{m+1} we obtain

$$\Omega(g_{2D}) = \lambda(1+m) - \frac{g_{2D}}{4\pi}\frac{(2m-2)!}{2^{2m-1}\,(m-1)!m!}. \tag{4.8}$$

We see that Ω as a function of g_{2D} is a line in the plane, with the slope originating from the many body interaction term and the intercept is given by the other energies.

For the second order transition we need to use a full linear combination of the form of Eq.(4.2) to compute the energy. It is then

$$E = \sum_m \left|c_m\right|^2 \epsilon_m + \sum_{m,n,\ell,k} c_m c_n c_\ell c_k \left\langle m, n\right| V \left|\ell, k\right\rangle \delta_{m+n,\ell+k}, \tag{4.9}$$

with $\epsilon_m = \frac{1}{2}\lambda\left(m+1\right)\left(m+2\right) - m\Omega$ being the single particle energy. In Eq.(4.9) we only need to retain terms that are at most bilinear in c_m for $m \neq m_0$, since the occupation of this states are small. Because of the Dirac delta function δ these numbers are constrained to be $m_1 + m_2 = 2m_0$. From Eq.(4.9) we calculate

$$\frac{\partial^2 E^{(2)}}{\partial c_{m_1} \partial c_{m_2}} = 4c_{m_0}^2 \left\langle m_1 m_2 \right| V \left| m_0 m_0 \right\rangle \delta_{m_1+m_2,2m_0}, \tag{4.10}$$

and

$$\begin{aligned} \frac{\partial^2 E^{(2)}}{\partial^2 c_{m_i}} &= 2\epsilon_{m_i} + 8c_0^2 \left\langle m_i m_0 \right| V \left| m_i m_0 \right\rangle + 4c_0^2 \left\langle m_0 m_0 \right| V \left| m_0 m_0 \right\rangle \\ &= 2\left(\epsilon_{m_i} - \epsilon_{m_0}\right) + 8c_0^2 \left\langle m_i m_0 \right| V \left| m_i m_0 \right\rangle - 4c_0^2 \left\langle m_0 m_0 \right| V \left| m_0 m_0 \right\rangle, \end{aligned} \tag{4.11}$$

where in the first line we used the fact that $8c_{m_0}^2 \left\langle m_0 m_0 \right| V \left| m_0 m_0 \right\rangle = -2\epsilon_0$, as can be seen from $\partial E / \partial c_{m_0} = 0$.

An example of this analysis is shown in Figure 17, for some triplets of numbers. Notice that some regions of the parameter space have multiple modes with negative eigenvalue. The leading order effect is then the one corresponding to the most negative eigenvalue.

In Figure 15 we can see the combination of this techniques. The solid lines represents the boundaries between macrovortex states with different total charge ν. We note that the variational results are in reasonable agreement with the perturbation theory boundaries, and we have also obtained the same ground states configurations numerically. For small Ω and g_{2D}, the predominant states are all macrovortex states. The explanation to this fact was already proposed by Lundh (21): for small g_{2D}, the energy is essentially that of a single particle wave function. For the potential Eq.(4.4), this energy scales as:

$$\epsilon_m = \frac{1}{2}\lambda\left(m+1\right)\left(m+2\right) - m\Omega, \tag{4.12}$$

which is faster than linearly with the angular momentum m. This implies that for a given m, a pure state with $c_m = 1$ and $c_n = 0$ for $n \neq m$ has a lower energy than any linear combination of the form Eq.(4.2). Hence the predominant states are all macrovortices with boundaries set by the predictions of perturbation theory, Eq.(4.8). As g_{2D} increases, however, the larger interaction energy of the multiply quantized vortex states eventually overcomes the kinetic plus trap energy, and the ground state will be again a vortex array. This also makes sense in light of the situation of a infinite, interacting uniform condensate: if the condensate is uniform, an energy argument shows that the energy of a vortex scales as m^2, so that a sum of charge 1 vortices with total charge m has lower energy than a single multiply quantized vortex of charge m. If g_{2D} is large, the healing length is small

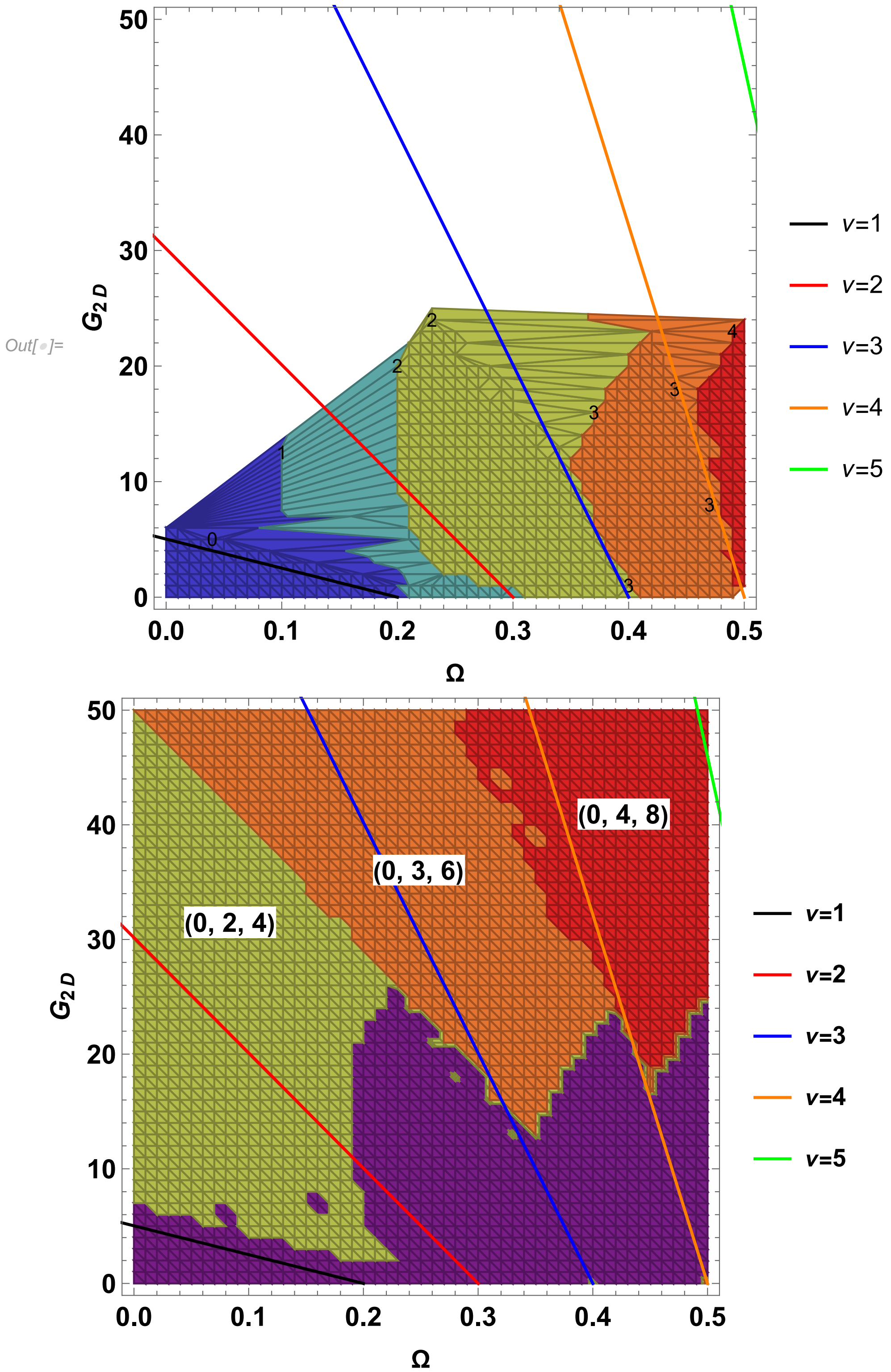

Figure 15 – Phase diagram for the Mexican Hat potential with $\lambda = 0.1$, Eq.(4.4). (Top) Macrovortex region. The solid lines indicates the predicted boundaries by using perturbation theory, while the colored region shows the resulting charge obtained in the variational method. (Bottom) Vortex lattice region. The solid lines are the boundaries between states with different total charge ν. The dark purple region is the macrovortex state, while the other colors represents vortex lattices.

Source: By the author.

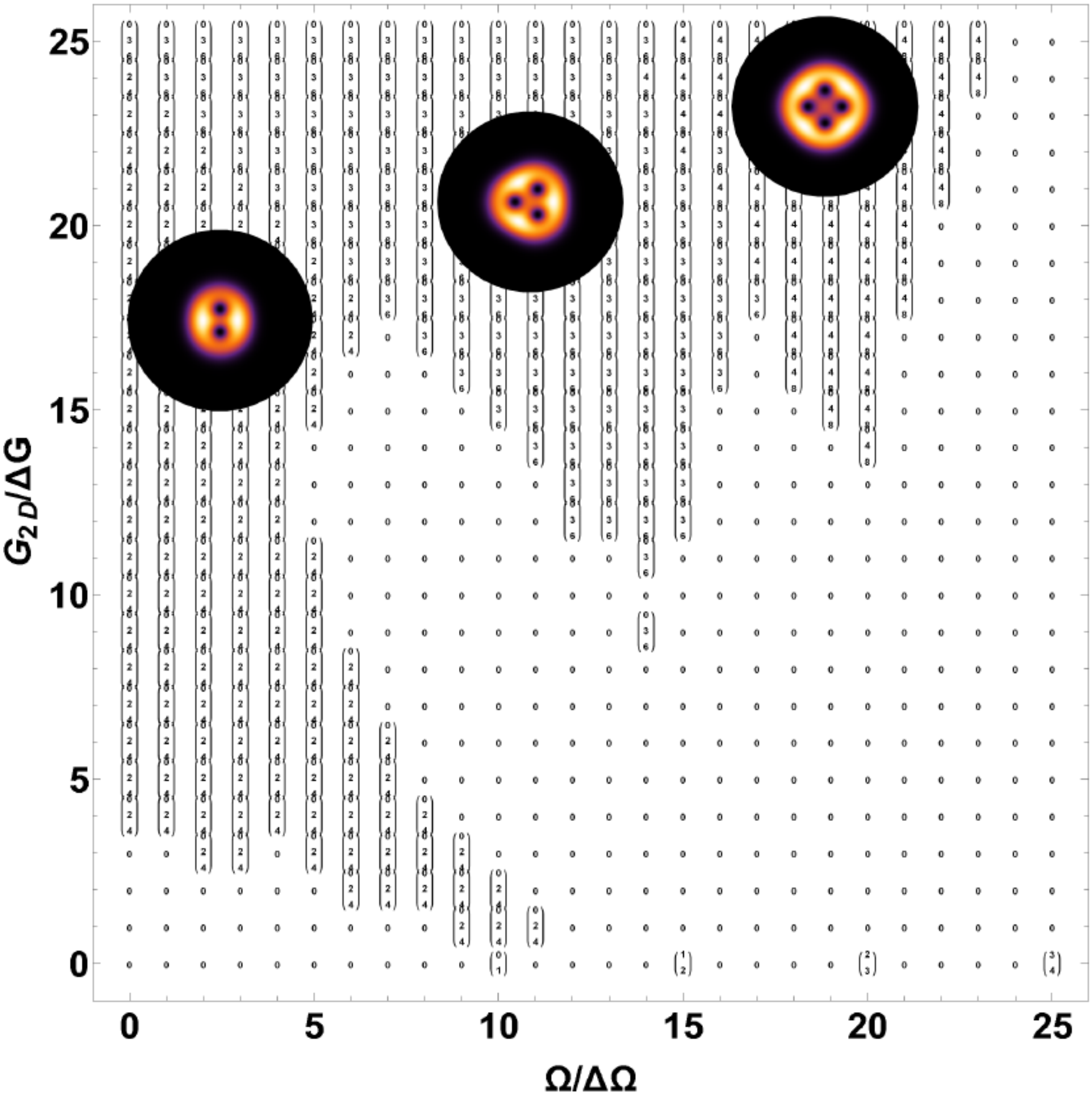

Figure 16 – Triplet of numbers c_{m_0}, c_{m_1} and c_{m_2} characterizing phase transitions to a vortex lattice. The regions marked as 0 are macrovortex regions.
Source: By the author.

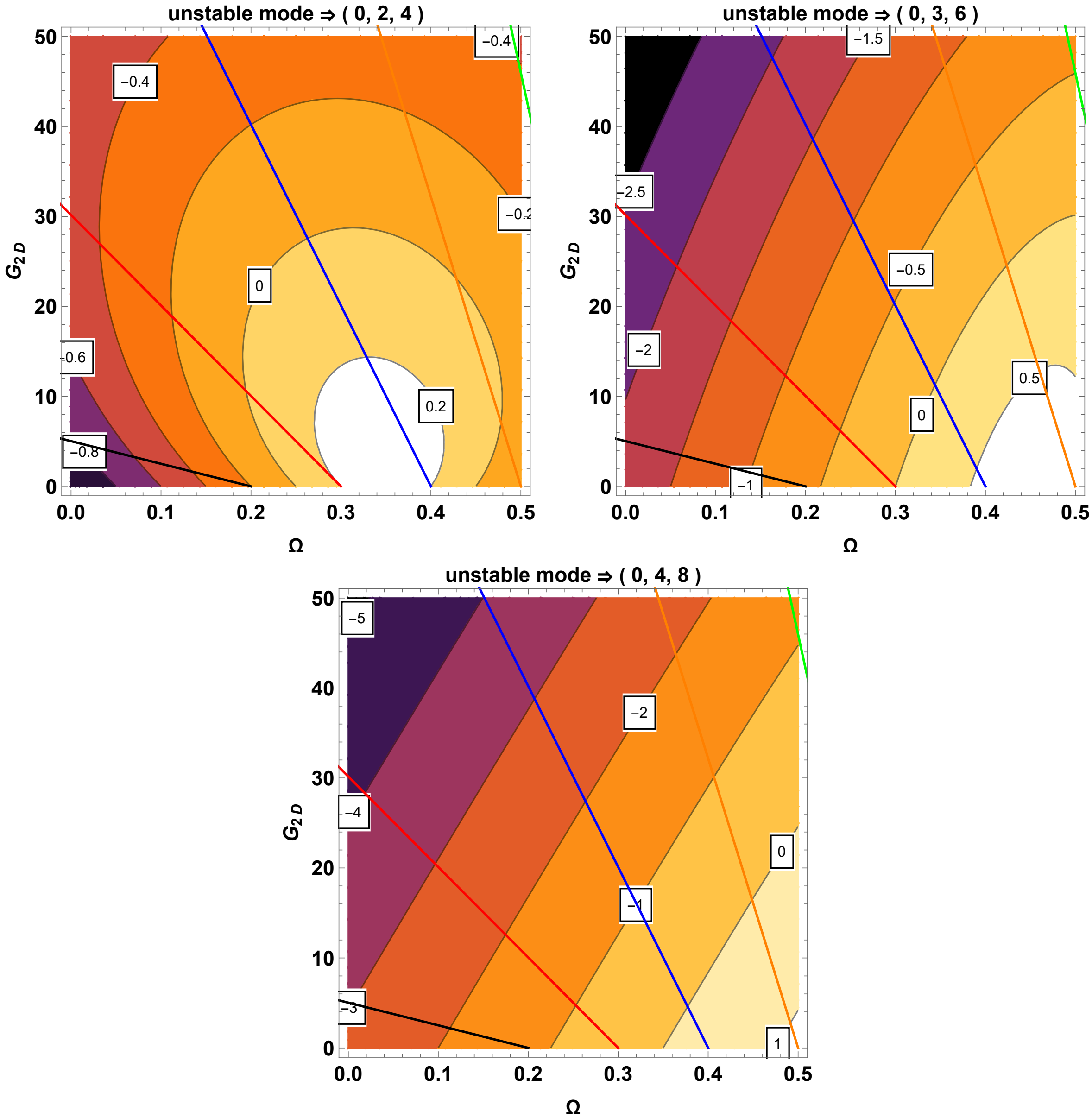

Figure 17 – Example eigenvalue analysis of the stability matrix formed by Eqs.(4.10-4.11). Regions where the eigenvalues get negatives are unstable with respect to the formation of a macrovortex.

Source: By the author.

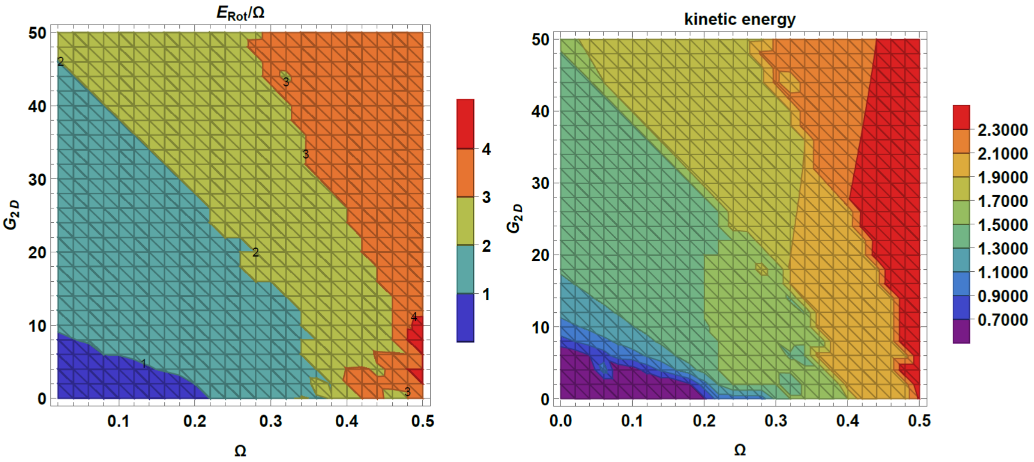

Figure 18 – Rotational and kinetic energy as a function of Ω and g_{2D}, for the MH potential with $\lambda = 0.1$.
Source: By the author.

so that the vortices cores are small. When the vortices' cores are smaller than all length scales of the problem, the vortices "see" an effectively uniform system, so the preferred configuration is that of the uniform setting: a vortex lattice. In Figure 18, which shows the kinetic and rotational energy as a function of Ω and g_{2D}, note that the rotational energy appears to track the first order transitions, while the kinetic energy marks the second order transitions.

For the lattices, we note that the predominant transition is always of the form $(m_1, m_0, m_2) = (0, m_0, 2m_0)$, as can be seen in Figure 16. This type of transition was also observed in a quadratic *plus* quartic potential (50). To understand that, it is useful to recall the fact that for a thin annulus the Mexican Hat potential can be related to the shifted harmonic oscillator, where the shift from the origin is related to the anarmonicity parameter by $R = 1/\sqrt{2\lambda}$ (48). If λ is not very small there will be a non-vanishing density at the origin, due to the overlap of the ring width. The states with $m_1 = 0$ have a non-vanishing density at the origin, since they are the only states that do not depend on ρ polynomially, and therefore they appear in lattice transitions if g_{2D} is not so large and λ not so small. As Ω increases, however, centrifugal effects depletes the density at the origin and we expect transitions with $m_1 \neq 0$.

4.1.2 Shifted Harmonic Oscillator

For the SHO potential

$$V = \frac{1}{2}\left(\rho - \rho_0\right)^2, \tag{4.13}$$

the required ϕ_m functions are different:

$$\phi_m(\rho,\varphi) = A_m \rho^m e^{im\varphi} e^{-(\rho-\xi)^2/2}, \tag{4.14}$$

where ξ is also treated as a variational parameter and A_m is a normalization constant given by

$$A_m^2 = \frac{1}{\pi\left[m!\,{}_1F_1\left(-m-\frac{1}{2};\frac{1}{2};-\xi^2\right) + 2\xi\Gamma\left(m+\frac{3}{2}\right)\,{}_1F_1\left(-m;\frac{3}{2};-\xi^2\right)\right]}, \tag{4.15}$$

where ${}_1F_1$ is the confluent hypergeometric function.

The inclusion of this additional parameter is necessary because in the SHO potential the condensate has an annular structure even with zero angular momentum, a situation that can not happen with the previously used ansatz of Eq.(4.5). The MH can also have a depleted center at zero angular momentum, but this requires very small values of the λ parameter. The energy expressions for this ansatz are then:

$$E_{kin} = \frac{\xi^2}{2} - A_m^2\left(-B_{m+1} + 2\xi B_{m+1/2} + 2mB_m - m^2 B_{m-1} - 2\xi m B_{m-1/2}\right) + m^2 A_m^2 B_{m-1}, \tag{4.16}$$

$$E_{trap} = \frac{1}{2}\rho_0^2 + \left(A_m^2 B_{m+1} - 2\rho_0 A_m^2 B_{m+1/2}\right), \tag{4.17}$$

$$E_{int} = \frac{g_{2D}}{\pi} A_m^4 D_{2m}, \tag{4.18}$$

$$E_{rot} = -m\Omega \tag{4.19}$$

where the coefficients B_m and D_m are given by:

$$B_m \equiv = \frac{1}{2}\left[\Gamma(1+m)\,{}_1F_1\left(-\frac{1}{2}-m,\frac{1}{2},-\xi^2\right) + 2\xi\Gamma\left(m+\frac{3}{2}\right)\,{}_1F_1\left(-x,\frac{3}{2},-\xi^2\right)\right] \tag{4.20}$$

and

$$D_m \equiv = \left(\frac{1}{\sqrt{2}}\right)^{2m+1}\left[\frac{\Gamma(m+1)}{2\sqrt{2}}\,{}_1F_1\left(-m-\frac{1}{2};\frac{1}{2};-\frac{\xi^2}{2}\right) + \xi\Gamma\left(m+\frac{3}{2}\right)\,{}_1F_1\left(-x;\frac{3}{2};-\frac{\xi^2}{2}\right)\right]. \tag{4.21}$$

As in the MH potential case, we equate the energy of a state with total angular momentum m with one of total angular momentum $m+1$ to extract Ω as a function of

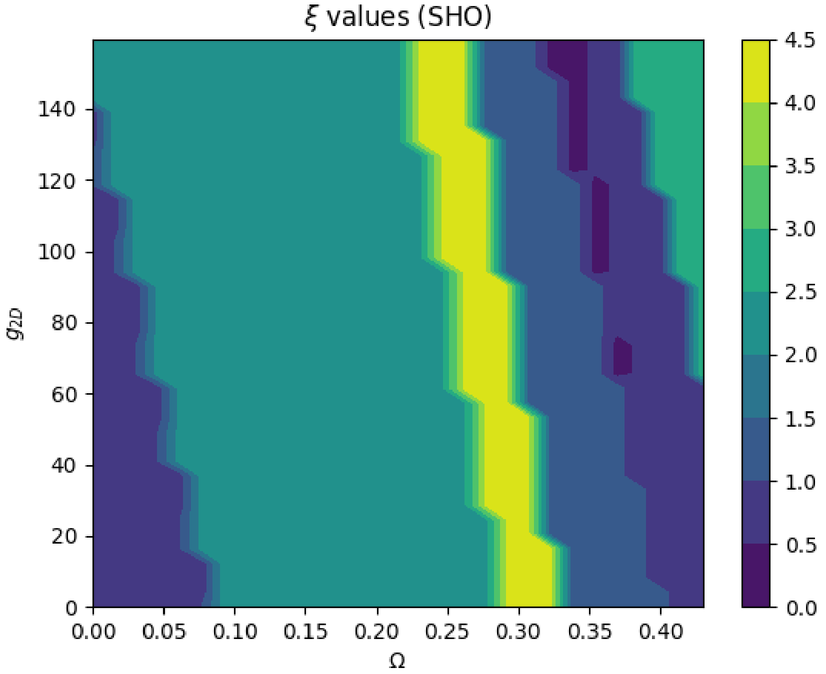

Figure 19 – ξ as a function of g_{2D} and Ω for the SHO potential with $\rho_0 = 4$.
Source: By the author.

g_{2D}. Here, we make the approximation that ξ does not depend on Ω and g_{2D}. In reality, ξ depends on both this parameters, as can be seen in Figure 19. We have tried modeling ξ as being the position of the minimum of the effective potential, or the maximum of the wave function, but we couldn't get more consistent results than by simply assuming it to be constant. With this assumption, as in the MH potential case, Ω as a function of g_{2D} will be a line:

$$\Omega_m = a_m \gamma + b_m, \tag{4.22}$$

with the slope a_m being dictate by the interaction energy:

$$a_m = -2\left(A_m^4 D_{2m} - A_{m+1}^4 D_{2(2m+1)}\right), \tag{4.23}$$

and the intercept b_m being a function of the kinetic and trap energies:

$$\begin{aligned}
b_m = &-A_{m+1}^2\left(-B_{m+2} + 2\xi B_{m+3/2} + 2(m+1)B_{m+1} - (m+1)^2 B_m - 2\xi(m+1)B_{m+1/2}\right)\\
&+ A_m^2\left(-B_{m+1} + 2\xi B_{m+1/2} + 2mB_m - m^2 B_{m-1} - 2\xi m B_{m-1/2}\right)\\
&+ (m+1)^2 A_{m+1}^2 B_m - m^2 A_m^2 B_{m-1} + \left(A_{m+1}^2 B_{m+2} - 2\rho_0 A_{m+1}^2 B_{m+3/2}\right)\\
&- \left(A_m^2 B_{m+1} - 2\rho_0 A_m^2 B_{m+1/2}\right).
\end{aligned} \tag{4.24}$$

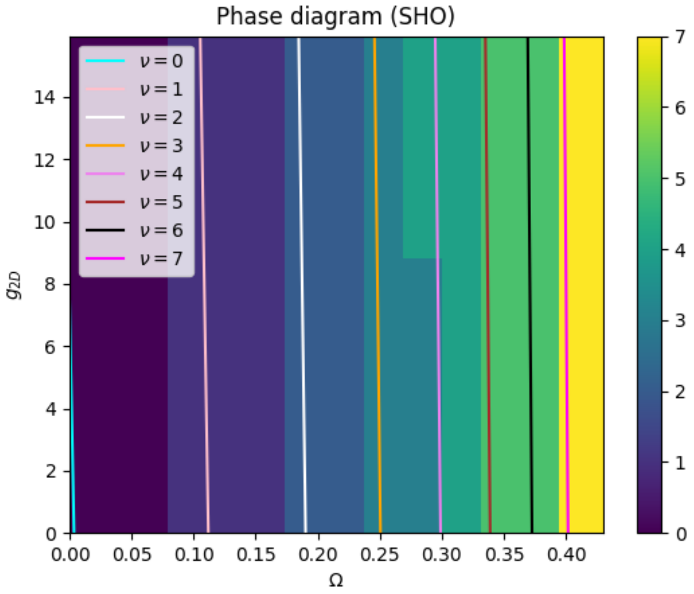

Figure 20 – Phase diagram for the SHO potential with $\rho_0 = 4$,with 1600 points. The solid lines are the resulting calculations from perturbation theory, Eq.(4.22), while the colors are the result of a variational calculation.
Source: By the author.

In Figure 20 we show the resulting lines of Eq.(4.22) together with a variational calculation. Because of the inclusion of the parameter ξ in the ansatz, the numerical methods were very unstable when using a general linear combination of the form Eq.(4.2) and good results were not obtained. To circumvent this problem, we limited ourselves to small values of g_{2D} and Ω, so that the system was surely in a macrovortex state. In this situation, we treatead the total angular momentum m together with ξ as the variational parameters of the problem, thus considering the system to occupy a pure state, and the resulting values of m are shown in the color scale of Figure 20.

Excepting for the $\nu = 0$ line, the other lines are in good agreement with the results of the variational calculation. We have also simulated a sample of points in the diagram numerically and obtained the same ground state as predicted by the variational method. Although it is not shown in the figure because of the already mentioned limitation of this variational method, we have also verified numerically that the SHO experiences a transition to a vortex lattice provided the interaction parameter g_{2D} is sufficiently large.

Having verified that the $\nu = 0$ does not agree well with the numerics, we decided to test how the results fair using the traditional harmonic oscillator ansatz given by Eq.(4.5). Using this functions, the energy of a pure state m is straightforwardly calculated as

$$E_m = 1 + m + \frac{\rho_0^2}{2} - \frac{\rho_0\sqrt{\pi}}{2}\frac{(2m+1)!}{2^{2m}(m!)^2} + \frac{g_{2D}}{4\pi}\frac{(2m)!}{2^{2m}\,(m!)^2} - m\Omega. \tag{4.25}$$

Equating the energies E_m and E_{m+1} allows us to extract the boundary lines for increasing ν values:

$$\Omega\left(g_{2D}\right)=1-\frac{\rho_0\sqrt{\pi}}{2}\frac{(2m)!}{2^{2m}(m!)^2}-\frac{g_{2D}}{2\pi}\frac{(2m-2)!}{2^{2m}\left(m-1\right)!m!}. \tag{4.26}$$

Employing Eq.(4.22) and varying the energy of the system given for combinations of coefficients c_m, we can construct a phase diagram with the corresponding boundary lines, as we did in the MH case. Because of numerical expenses, however, we used $\rho_0 = 2.5$. This lower value allowed for more stable and consistent results for higher rotation rates.

The results can be seen on Figure 21. As expected, because the ansatz given by Eq.(4.5) requires less parameters, it provided more stable results and allowed us to make the same analysis for the second order phase transition as in the MH potential. Notice the absence of a $\nu = 0$ region. This is to expected: since the SHO potential favours a depleted central region, even at zero angular momentum, and the pure harmonic oscillator functions given by Eq.(4.5) cannot form a hole with zero angular momentum, this state is energetically disfavoured. This disadvantage was the feature that prompted us to use the modified ansatz given by Eq.(4.14). Since, however, using these functions did not produce a reliable prediction for the $\nu = 0$ line, no advantage is gained and we completed our analysis with the harmonic oscillator functions given by Eq.(4.5).

A noticeable difference between the phase diagram of Figure 15 and Figure 21 is the larger region occupied by the macrovortices in Figure 21. This happens because the SHO potential acts as a stabilizer "pinning" potential of the macrovortex configuration, making it more stable across the phase space. This point will be further elaborated when we discuss the Thomas-Fermi profiles.

In the bottom of Figure 21 we can see the region occupied by lattices. This figure was produced with the same stability matrix analysis used for MH potential, with eigenvalues analysis similar to Figure 17. As in the MH situation, for a macrovortex mode given by the coefficient c_{m_0} the second order transition requires that we keep terms that are at most bilinear in c_m for $m \neq m_0$ and $m_1 + m_2 = 2m_0$, $\left|c_{m_0}\right|^2 + \left|c_{m_1}\right|^2 + \left|c_{m_2}\right|^2 \approx 1$. It is noticeable that a special case of central charge 1 symmetric lattices exists. We also found special cases of non symmetric lattice were various coefficients c_{m_i} were non-negligible. We still don't know if these configurations represent another type of transition of the system, or if it would be a prediction failure of the variational model, since these situations usually takes place in regions of the phase space of high angular velocity and interaction parameter.

Finally, Figure 22 shows the analysis of the partial energy diagrams. As in the case of the MH potential, the diagram of rotational energy normalized by Ω presented the quantized values ν referring to the respective phases of macrovortices. The kinetic

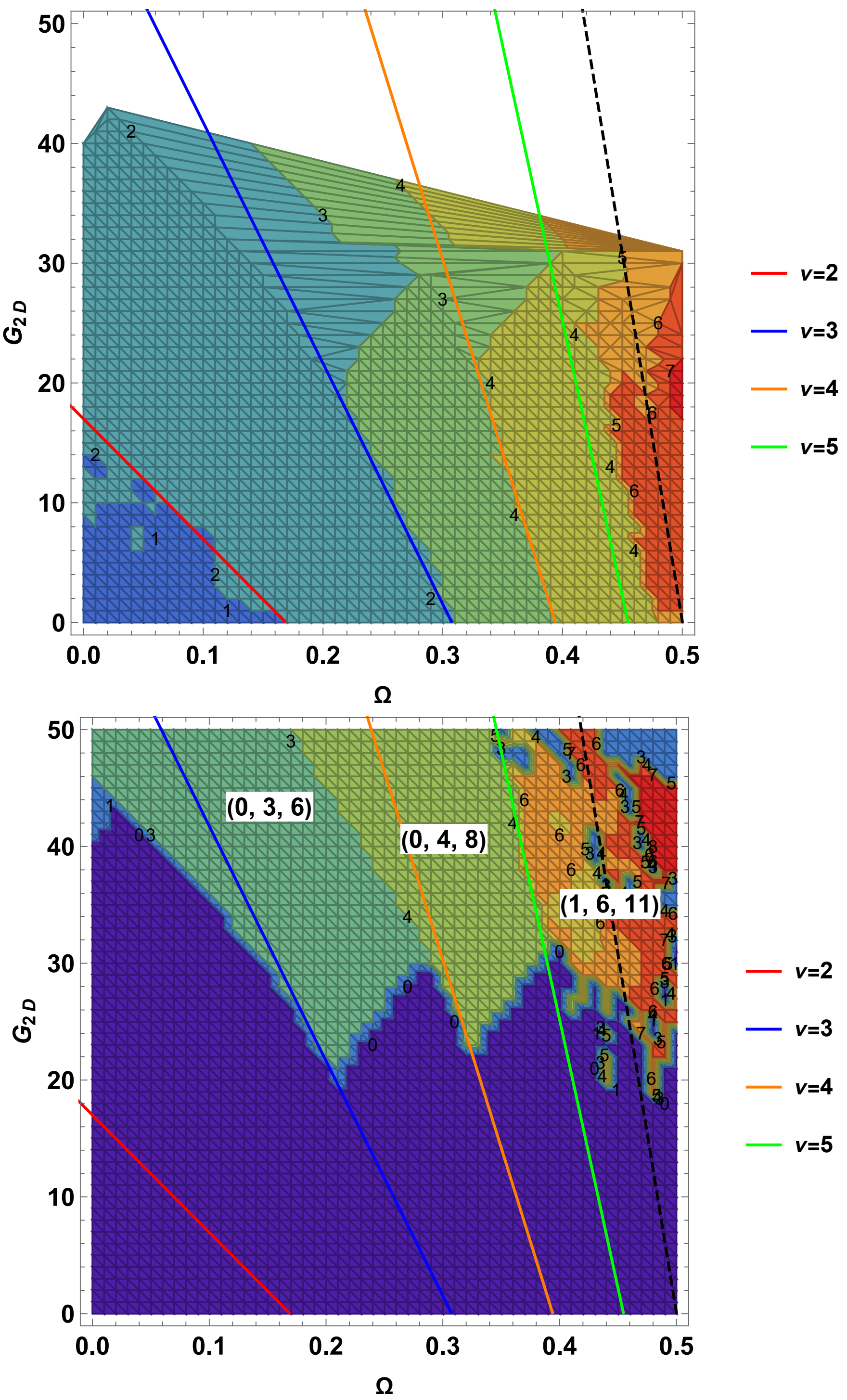

Figure 21 – Phase diagram for the SHO potential Eq.(4.13) with $\rho_0 = 2.5$. (Top) Macrovortex region. The solid lines indicates the predicted boundaries by using perturbation theory, Eq.(4.26), while the colored region shows the resulting charge obtained in the variational method. (Bottom) Vortex lattice region. The solid lines are the boundaries between states with different total charge ν. The dark purple region is the macrovortex state, while the other colors represents vortex lattices.
Source: By the author.

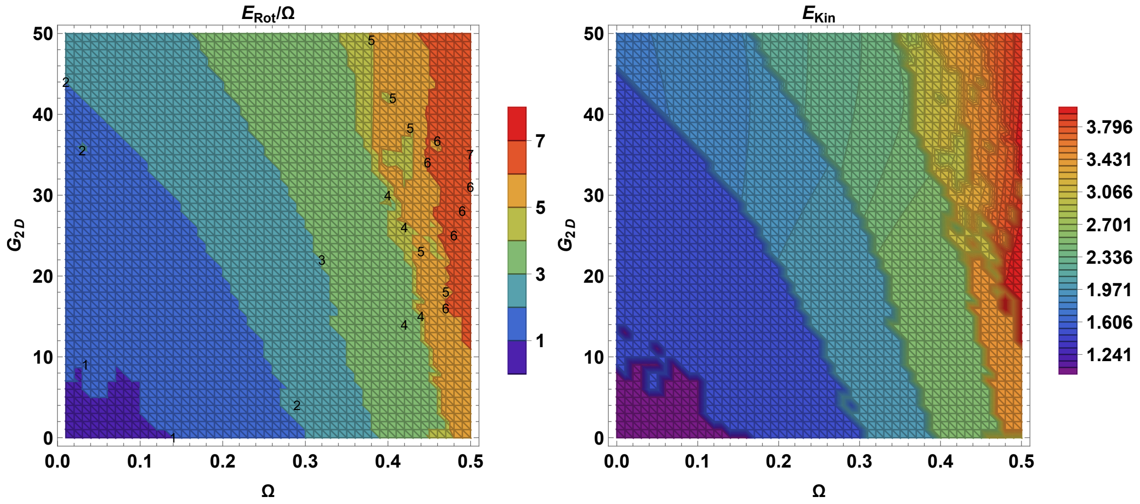

Figure 22 – Rotational and kinetic energy as a function of Ω and g_{2D}, for the SHO potential with $\rho_0 = 2.5$.
Source: By the author.

energy diagram, on the other hand, shows a suddenly decrease in energy in the region that should correspond to the lattice formation.

Up to now our analysis included only small interaction parameters, g_{2D}, since it is in those situations that the overall density function is expected to be a Gaussian. For studying higher interaction parameters, we proceed to use the Thomas-Fermi approximation, as we shall now discuss.

4.2 Thomas-Fermi

The starting point for our calculations is the energy in the rotating frame with angular velocity $\boldsymbol{\Omega}$:

$$E = \int d^2r \left[\frac{1}{2}\left|\nabla\psi\right|^2 + V_\perp(\rho)\left|\psi\right|^2 + \frac{1}{2}g_{2D}\left|\psi\right|^4 - \psi^*\boldsymbol{\Omega}\cdot\boldsymbol{r}\times\boldsymbol{p}\psi\right]. \tag{4.27}$$

For the angular momentum term, we write it as:

$$-\psi^*\boldsymbol{\Omega}\cdot\boldsymbol{r}\times\boldsymbol{p}\psi = -\psi^*\Omega L_z\psi = i\psi^*\Omega\frac{\partial\psi}{\partial\varphi}, \tag{4.28}$$

where the axis of rotation was chosen as the z axis and φ is the polar angle. We then perform a Madelung transformation to write:

$$\psi = \left|\psi\right| e^{iS}, \tag{4.29}$$

and then letting the derivative act we obtain:

$$\begin{aligned}
-\psi^* \boldsymbol{\Omega} \cdot \boldsymbol{r} \times \boldsymbol{p} \psi &= i\psi^* \Omega \left(\frac{\partial |\psi|}{\partial \varphi} e^{iS} + i \frac{\partial S}{\partial \varphi} |\psi| e^{iS} \right) \\
&= i\Omega \left(|\psi| \frac{\partial |\psi|}{\partial \varphi} + |\psi|^2 i \frac{\partial S}{\partial \varphi} \right) \\
&= \frac{1}{2} i\Omega \frac{\partial |\psi|^2}{\partial \varphi} - \Omega \frac{\partial S}{\partial \varphi} |\psi|^2 . \qquad (4.30)
\end{aligned}$$

Remember that the velocity field of the fluid in the hydrodynamic picture is $\boldsymbol{v}_s = \nabla S$, and $\nabla S|_\varphi = (1/\rho)\partial S/\partial \varphi$:

$$\Omega \frac{\partial S}{\partial \varphi} = \Omega \rho \, \nabla S|_\varphi . \qquad (4.31)$$

But taking $\boldsymbol{\Omega} = \Omega \hat{z}$ and $\boldsymbol{r} = \rho \hat{r}$,we have $\boldsymbol{\Omega} \times \boldsymbol{r} = \Omega \rho \hat{\varphi}$ so that

$$\Omega \frac{\partial S}{\partial \varphi} = \Omega \rho \, \nabla S|_\varphi = (\boldsymbol{\Omega} \times \boldsymbol{r}) \cdot \nabla S. \qquad (4.32)$$

Using $\boldsymbol{v}_{sb} = \boldsymbol{\Omega} \times \boldsymbol{r}$ and $\boldsymbol{v}_s = \nabla S$:

$$-\psi^* \boldsymbol{\Omega} \cdot \boldsymbol{r} \times \boldsymbol{p} \psi = \frac{1}{2} i\Omega \frac{\partial |\psi|^2}{\partial \varphi} - (\boldsymbol{v}_s \cdot \boldsymbol{v}_{sb}) |\psi|^2 . \qquad (4.33)$$

Note that because ψ must not be multivalued the first term in Eq.(4.33) yields no contribution when integrated over φ, and hence can be ommited.

We also write the derivative of the wave function as:

$$\nabla \psi = \nabla |\psi| e^{iS} + i \nabla S |\psi| e^{iS} = \nabla |\psi| e^{iS} + i \nabla S \psi, \qquad (4.34)$$

and now we use the Thomas-Fermi approximation: we suppose that in this derivative, the first term (the gradient of the density) is much smaller than the second term, so that:

$$|\nabla \psi|^2 \approx |\nabla S|^2 |\psi|^2 = v_s^2 |\psi|^2 , \qquad (4.35)$$

and we rewrite

$$\boldsymbol{v}_{sb}^2 \equiv (\boldsymbol{\Omega} \times \boldsymbol{r})^2 = \Omega^2 \rho^2 - (\boldsymbol{\Omega} \cdot \boldsymbol{r})^2 = \Omega^2 \rho^2, \qquad (4.36)$$

since $\boldsymbol{\Omega}$ and $\boldsymbol{r}$ are orthogonal vectors. Then

$$\frac{1}{2} |\nabla \psi|^2 - \psi^* \boldsymbol{\Omega} \cdot \boldsymbol{r} \times \boldsymbol{p} \psi = \frac{1}{2} (\boldsymbol{v}_s - \boldsymbol{v}_{sb})^2 |\psi|^2 - \frac{1}{2} \Omega^2 \rho^2 |\psi|^2 , \qquad (4.37)$$

and the free energy becomes

$$E = \int d^2r \left[\frac{1}{2} \left(\boldsymbol{v}_s - \boldsymbol{v}_{sb} \right)^2 |\psi|^2 + V |\psi|^2 + \frac{1}{2} g_{2D} |\psi|^4 - \frac{1}{2} \Omega^2 \rho^2 |\psi|^2 \right]. \tag{4.38}$$

Further elaboration of the calculations depends in the potential term V and the velocity field $\boldsymbol{v}_s$.

4.2.1 Mexican Hat

4.2.1.1 Formation of a hole

In the Mexican Hat potential, we can have a "static" hole, formed because of the trap parameters configuration, or a "dynamic" hole that is formed due to the rotation of the gas. To analyze the first scenario we begin by supposing a non-rotating condensate, with no vortices.

If we extremize Eq.(4.38) with respect to $|\psi|^2$ keeping the number of particles constant we obtain (taking $\Omega = 0$ and $\boldsymbol{v}_s = 0$).

$$|\psi|^2 = \frac{\mu + \rho^2/2 - (\lambda/2)\,\rho^4}{g_{2D}}, \tag{4.39}$$

which have the roots:

$$R_{1,2}^2 = \left(1 \mp \sqrt{1 + 8\lambda\mu} \right) / \left(2\lambda \right). \tag{4.40}$$

By defining the sum and difference squared of the radii $R_\pm^2 \equiv R_2^2 \pm R_1^2$ we obtain

$$\lambda R_+^2 = 1, \tag{4.41}$$

$$\lambda R_-^2 = \eta \equiv \left(\frac{12 g \lambda^2}{\pi} \right)^{1/3}. \tag{4.42}$$

In order for the two roots in Eq.(4.40) to be real, we must have $\mu < 0$. By imposing the normalization condition $\int d^2 r n(\boldsymbol{r}) = 1$ we obtain the following conditions

$$\mu = \frac{\eta^2 - 1}{8\lambda}. \tag{4.43}$$

Therefore, the condensate is annular provided $\eta < 1$.

4.2.1.2 Vortex lattice

In this case, $\boldsymbol{v}_s = \boldsymbol{v}_{sb}$ in the fluid so the first term in Eq.(4.38) vanishes. Since the potential is given by Eq.(4.4), upon extremization with respect to $|\psi|^2$ while keeping the number of particles constant, we obtain the Gross-Pitaevskii equation:

$$|\psi|^2 = \frac{\mu + (1/2)\left(1+\Omega^2\right)\rho^2 - (\lambda/2)\rho^4}{g_{2D}}, \tag{4.44}$$

then $n = |\psi|^2$ if $|\psi|^2 > 0$ or $n = 0$ otherwise. Equation (4.44) has the roots:

$$R_i^2 = \left(\frac{1+\Omega^2}{2\lambda}\right) \pm \sqrt{\left(\frac{1+\Omega^2}{2\lambda}\right)^2 + \frac{2\mu}{\lambda}},\ i = 1, 2. \tag{4.45}$$

If the condition $\eta < 1$ is not established and the condensate is not annular due to the trap parameters, it can still have a hole due to the centrifugal effects in place. For each λ and g_{2D} there is a critical angular velocity Ω_c, which can be determined by demanding the wave function to be normalized $\int n d^2 r = 1$ when $\mu = 0$ (so that $R_2^2 = \left(1+\Omega^2\right)/\lambda$ and $R_1 = 0$):

$$\Omega_c = \sqrt{\left(\frac{12\lambda^2 g_{2D}}{\pi}\right)^{1/3} - 1}. \tag{4.46}$$

From Eq.(4.46), we see that there exists a critical velocity provided

$$g_{2D} \geq \frac{\pi}{12\lambda^2}. \tag{4.47}$$

Below we shall work in the regime $g_{2D} \geq \frac{\pi}{12\lambda^2}$ and $\Omega \geq \Omega_c$ so that $\mu \leq 0$ and the condensate is always annular. Then there exists two radii and the density can be written as

$$n = \frac{\lambda}{2g_{2D}}\left(R_2^2 - \rho^2\right)\left(\rho^2 - R_1^2\right), \tag{4.48}$$

and imposing the normalization of the wave function we obtain:

$$\pi\lambda\left(R_2^2 - R_1^2\right)^3 = 12 g_{2D}. \tag{4.49}$$

To make contact with the literature (48) we define $\eta \equiv \left(12 g_{2D}\lambda^2/\pi\right)^{1/3}$ so that

$$\eta = \lambda\left(R_2^2 - R_1^2\right). \tag{4.50}$$

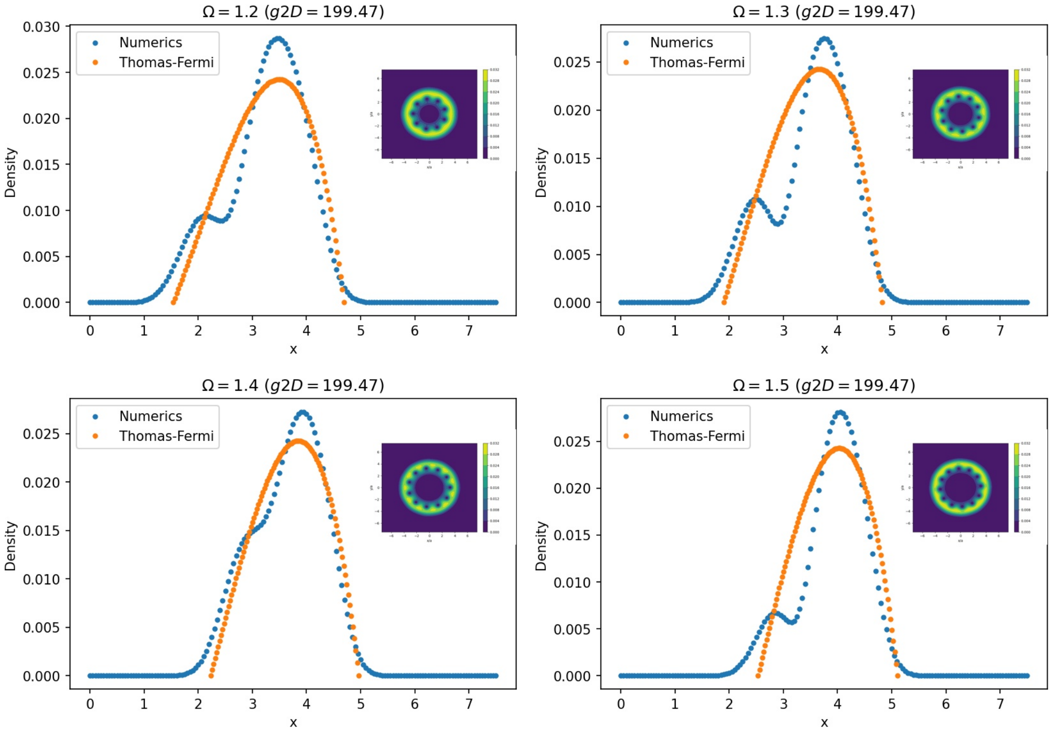

Figure 23 – Density profile for various angular speeds Ω, $g_{2D} = 199.47$ and the Mexican Hat potential with $\lambda = 0.1$. The blue dots represent the numerical profiles, extracted from a 1D cut from the full wave function (with the full numerical density displayed in the inset), while the orange dots are the Thomas-Fermi prediction given by Eq.(4.44).
Source: By the author.

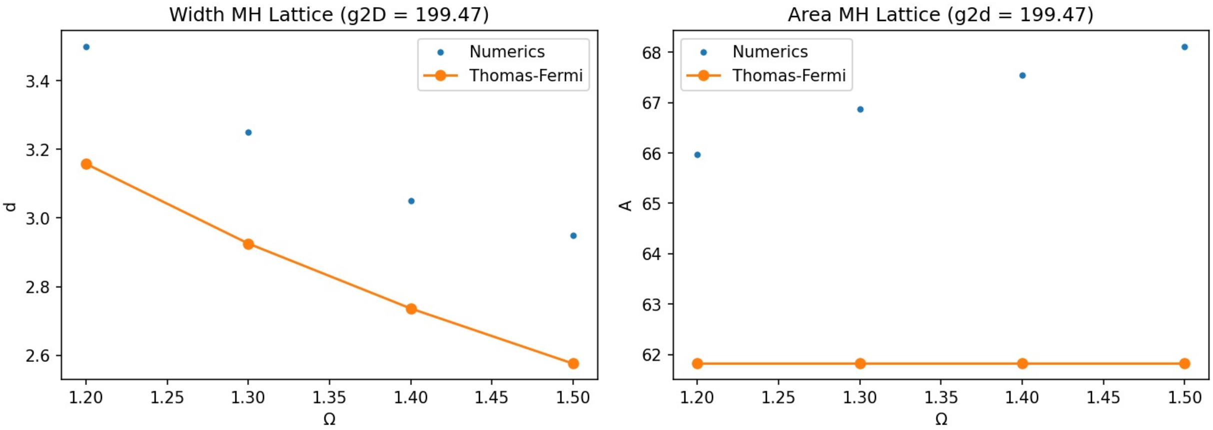

Figure 24 – Width (left) and area (right) as a function of Ω for the Mexican Hat potential with $\lambda = 0.1$ and $g_{2D} = 199.47$. The blue points represent the numerical points while the solid lines are the Thomas-Fermi predictions given by Eq.(4.50) and Eq.(4.45).
Source: By the author.

With the simple Eq.(4.50) we can extract the area of the condensate

$$A = \pi \frac{\eta}{\lambda}, \tag{4.51}$$

implying a constant area as a function of Ω. Also, using $R_2^2 - R_1^2$ from Eq.(4.45) we easily obtain an expression for the chemical potential:

$$\mu = \frac{1}{8\lambda} \left[\eta^2 - \left(1 + \Omega^2 \right)^2 \right] \, (\Omega \geq \Omega_c) \, . \tag{4.52}$$

These are all the information we need to characterize the wave function in this regime.

In Figure 23 we show the cuts along the x-axis of the numerical $1D$ profiles for various values of Ω, $\lambda = 0.1$ and $g_{2D} = 199.47$, together with the corresponding Thomas-Fermi profile given by Eq.(4.44). The bumps that can be seen in the numerical profile are due to the numerous vortices present in the condensate's ring, as shown in the insets. Typically the Thomas-Fermi peak value is slightly below the numerical peak, while the typical Thomas-Fermi width appears to be in good agreement with the numerics.

In reality, as can be seen in the left Figure 24, the Thomas-Fermi width is slightly below the numerical predictions, but the overall trend with Ω appears to be well reproduced by the model. This difference in the absolute value of the width can perhaps be traced to a difference in the values of the radii, as extract numerically and from the Thomas-Fermi predictions (see Figure 25). Numerically, the wave function does not have a rigid boundary but vanishes smootly. Therefore we need to select a threshold for which we consider the density to effectively vanish. It can be seen in Figure 25 that the best agreement between numerical data and the Thomas-Fermi prediction is attained when this threshold is select as 10^{-3}, and therefore we adopted this threshold in all subsequent analysis.

The disagreement of the area is more substantial as can be seen in the right of Figure 24. Now even the trend with Ω is different, as the Thomas-Fermi area is predicted to be constant but the numerical area appears to increase with Ω. We shouldn't be carried over by this fact, however, since the simple Thomas-Fermi profile does not account for the change of volume due to the individual vortices (it only accounts for the overall change due to the velocity field).

This is also the possible reason we see a disagreement between the predicted and simulated chemical potential, as shown in the right of Figure 26: the presence of vortices in the bulk produces a significant increase in the kinetic energy due to the density gradient, which are disregarded in the diffuse velocity field TF approximation. The energy can be seen in the left of Figure 26, and note that the energy per particle can be easily calculated

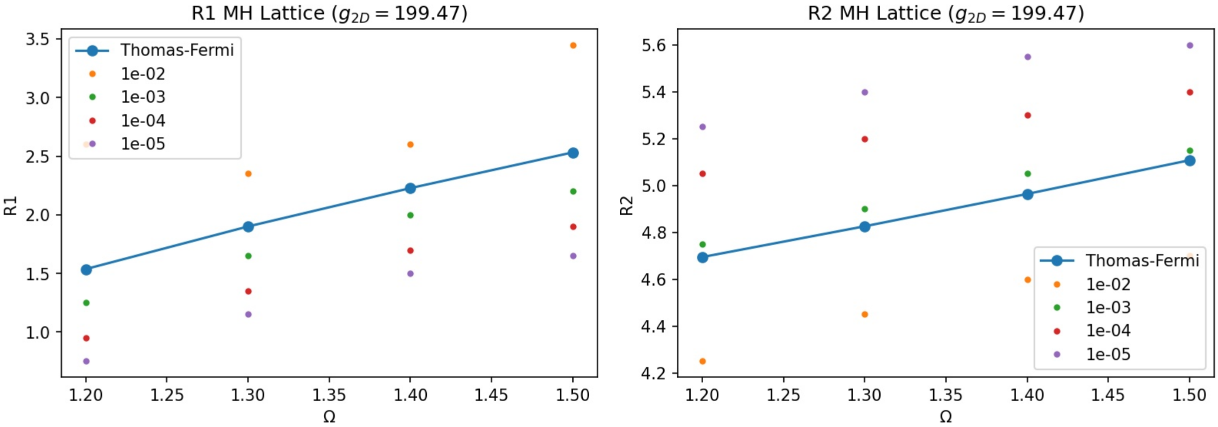

Figure 25 – Radii of the inner (left) and outer (right) boundaries of the condensate as a function of Ω, for $\lambda = 0.1$ and $g_{2D} = 199.47$. The points are extract from numerical simulations, with the different thresholds being the value for which the density was considered to vanish.
Source: By the author.

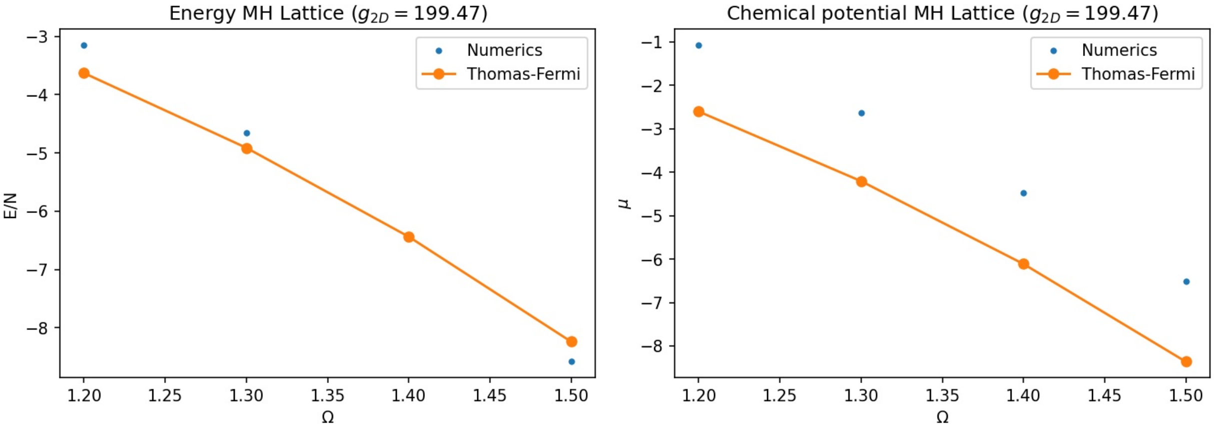

Figure 26 – Energy (left) and chemical potential (right) as a function of Ω, cf predictions of Eq.(4.52) and Eq.(4.54) as well as numerical simulations for the Mexican Hat potential Eq.(4.4) with $\lambda = 0.1$ and $g_{2D} = 199.47$.
Source: By the author.

by the thermodynamical relation:

$$\mu = \left(\frac{\partial E}{\partial N}\right)_{\Omega}, \tag{4.53}$$

resulting in

$$\frac{E}{N} = \frac{1}{8\lambda}\left[\frac{3}{5}\eta^2 - \left(1+\Omega^2\right)^2\right]. \tag{4.54}$$

4.2.1.3 Macrovortex

For a macrovortex situation the analysis gets more complicated: the fluid velocity is now characterized by

$$\boldsymbol{v}_s = \frac{\nu}{\rho}\hat{\varphi}, \tag{4.55}$$

where $\hat{\varphi}$ is the unit vector in the polar basis (ρ, φ). Then

$$\left(\boldsymbol{v}_s - \boldsymbol{v}_{sb}\right)^2 = \frac{\nu^2}{\rho^2} + \Omega^2\rho^2 - 2\nu\Omega, \tag{4.56}$$

and the energy becomes

$$E = \int d^2r \left[\left(\frac{\nu^2}{2\rho^2} - \frac{\nu\Omega}{\rho}\right)|\psi|^2 + V_{\perp}(\rho)\,|\psi|^2 + \frac{1}{2}g_{2D}\,|\psi|^4\right], \tag{4.57}$$

resulting in a density profile of the form

$$n = \frac{1}{2g_{2D}}\left[2\tilde{\mu} - \frac{\nu^2}{\rho^2} + \rho^2 - \lambda\rho^4\right], \tag{4.58}$$

with $\tilde{\mu} \equiv \mu + \nu\Omega$ if $|\psi|^2 \geq 0$ or $n = 0$ otherwise. The problem of finding the roots in Eq.(4.58) is a much more complicated problem than the roots of Eq.(4.44), because the problem is not bilinear in ρ. When two real and positive roots R_1 and R_2 exists it is therefore more convenient to work with $R_+^2 \equiv R_1^2 + R_2^2$ and $R_-^2 \equiv R_2^2 - R_1^2$. By imposing $n(R_1) = n(R_2)$ we obtain:

$$4\nu^2 = \left(R_+^4 - R_-^4\right)\left(\lambda R_+^2 - 1\right). \tag{4.59}$$

For relating the rotation rate with the vortex charge, we demand that $\partial E/\partial\nu = 0$:

$$\frac{\Omega}{\nu}\frac{\eta^3}{12\lambda^2} = \tilde{\mu}\ln\left(\frac{R_+^2 + R_-^2}{R_+^2 - R_-^2}\right) + \frac{R_-^2}{2} - \frac{\lambda}{4}R_+^2R_-^2 - \frac{2\nu^2R_-^2}{R_+^4 - R_-^4} \tag{4.60}$$

while normalization implies that

$$\tilde{\mu} = \frac{1}{8\lambda^2}\frac{\eta^3}{R_-^2} - \frac{1}{8}R_+^2 + \frac{3}{4}\frac{\nu^2}{R_-^2}\ln\left(\frac{R_+^2 + R_-^2}{R_+^2 - R_-^2}\right). \tag{4.61}$$

Approximate analytical solutions of Eqs.(4.59-4.61) can be obtained using the expansion $\lambda R_+^2 = 1 + \sum_n c_n \left(\lambda\nu\right)^{2n}$, which is appropriate provided $\lambda\nu << 1$ (48). Substituting this results we obtain:

$$\lambda R_+^2 = 1 + \frac{4}{1-\eta^2}\left(\lambda\nu\right)^2 + O\left[\left(\lambda\nu\right)^4\right], \tag{4.62}$$

$$\lambda R_-^2 = \eta + \frac{1}{\eta}\left[\frac{4}{\eta^2 - 1} + \frac{2}{\eta}\ln\left(\frac{1+\eta}{1-\eta}\right)\right]\left(\lambda\nu\right)^2 + O\left[\left(\lambda\nu\right)^4\right], \tag{4.63}$$

$$\lambda\mu = \frac{\eta^2 - 1}{8} + \frac{1}{2\eta}\ln\left(\frac{1+\eta}{1-\eta}\right)\left(\lambda\eta\right)^2 + O\left[\left(\lambda\nu\right)^4\right]. \tag{4.64}$$

With this same expansion, the energy is

$$\lambda E = -\frac{1}{8} + \frac{3}{40}\eta^2 + E_1\left(\lambda\nu\right)^2 + O\left[\left(\lambda\nu\right)^4\right], \tag{4.65}$$

where the second order term E_1 is

$$E_1 \equiv \frac{3}{4\eta^3}\left[2\eta - \left(1 - \eta^2\right)\ln\left(\frac{1+\eta}{1-\eta}\right)\right]. \tag{4.66}$$

The energy in the rotating frame is related to the lab frame by means of $E^{'}(\nu) = E(\nu) - \Omega\nu$. By using Eq.(4.65) and treating ν as a continous variable (valid if $\nu >> 1$), the ground state vorticity is attained when

$$\lambda\nu = \frac{\Omega}{2E_1}. \tag{4.67}$$

So, given a angular speed Ω and interaction parameter g_{2D}, we calculate the macrovortex charge with Eq.(4.67). With the vortex charge, R_+ and R_- can be calculated with Eq.(4.62) and Eq.(4.63), while the chemical potential is calculated with Eq.(4.64). This is all the necessary information to characterize the condensate.

In Figure 28 we plot the charge and chemical potential as a function of the angular velocity Ω and in Figure 27 we show the corresponding density profiles. Notice that we used $\lambda = 0.01$. That is because for the old value $\lambda = 0.1$, for $g_{2D} = 39.89$ we have $\eta > 1$ so that for the low angular velocities studied here the condensate did not settled in an annular form. The charge predicted by Eq.(4.67) is remarkably close to the numerical

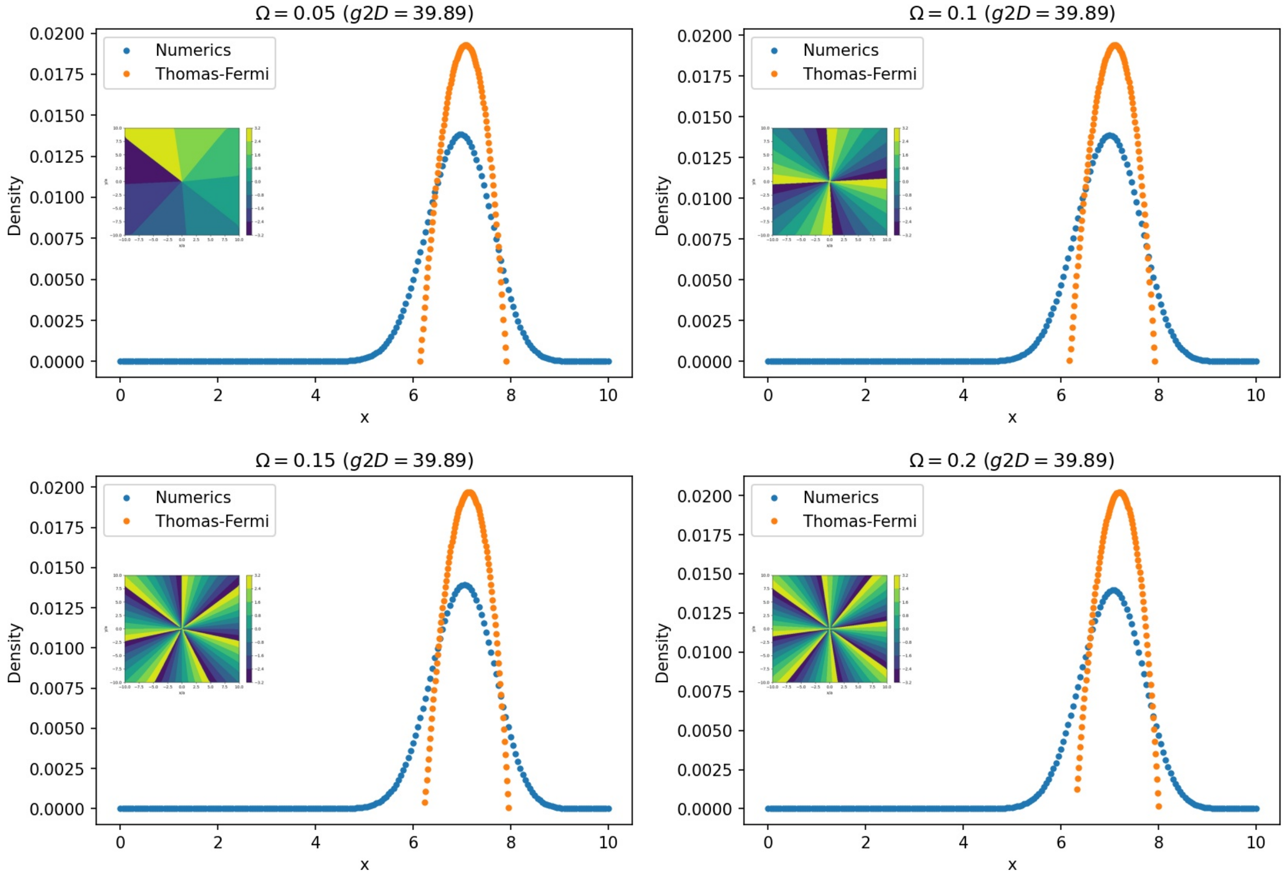

Figure 27 – Density profiles for the Mexican Hat potential with $\lambda = 0.01$ for various angular velocities and interaction parameter $g_{2D} = 39.89$. The orange points are the results of the Thomas-Fermi profiles, Eq.(4.58), while the blue points are numerical calculations. The inset shows the phase of the central macrovortex as computed numerically.
Source: By the author.

calculations, even for low angular velocities where the assumption $\nu >> 1$ does not hold. Once more we see that the chemical potential is lower than the numerics. This time we suspect that perhaps this happens due to low value of g_{2D} used in the simulation. Increasing this value was a sensible task because we could generate a lattice or break the annular form of the gas. It can also be seen in Figure 27 that the Thomas-Fermi radii as approximated by Eqs.(4.62) and Eq.(4.63) gets worse with increasing Ω.

In Figure 29 we can see how the area and width of the condensate changes as Ω increases. Once more we see that these quantities appears not to be in good agreement with the numerics when we look at the absolute value. This is to be expected, since the Thomas-Fermi radii appears to be smaller than the actual radii of the condensate, as can be seen in Figure 27. The trend with Ω appears to be of a decrease in both the width and the area, as can be seen in the bottom panels.

Finally, in Figure 30 we show the total energy as predicted by Eq.(4.65) and numer-

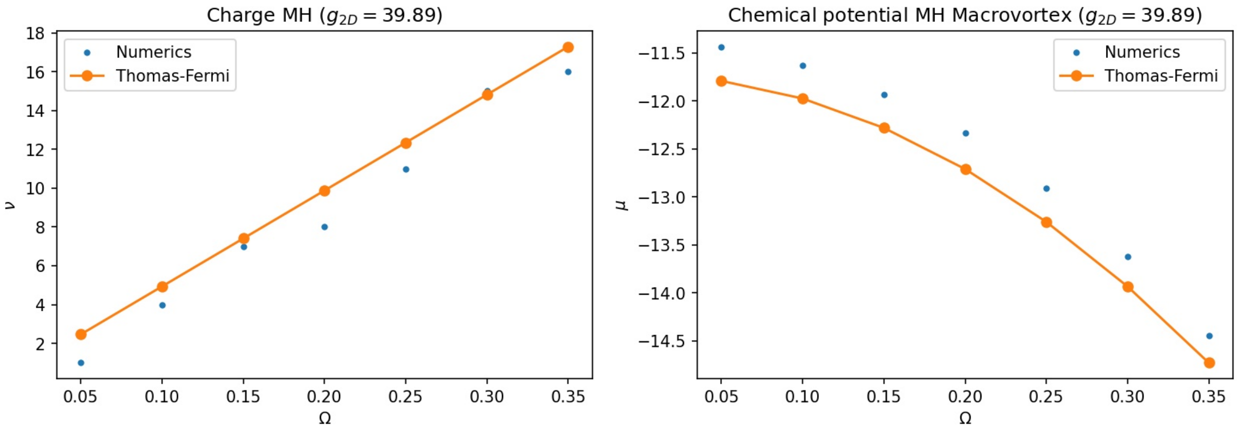

Figure 28 – Charge (left) and chemical potential (right) as a function of the angular velocity Ω, for the Mexican Hat potential with $\lambda = 0.01$ in a macrovortex configuration. The blue dots are quantities calculated numerically, while the orange dash doted lines are the Thomas-Fermi predictions of Eq.(4.67) and Eq.(4.64).
Source: By the author.

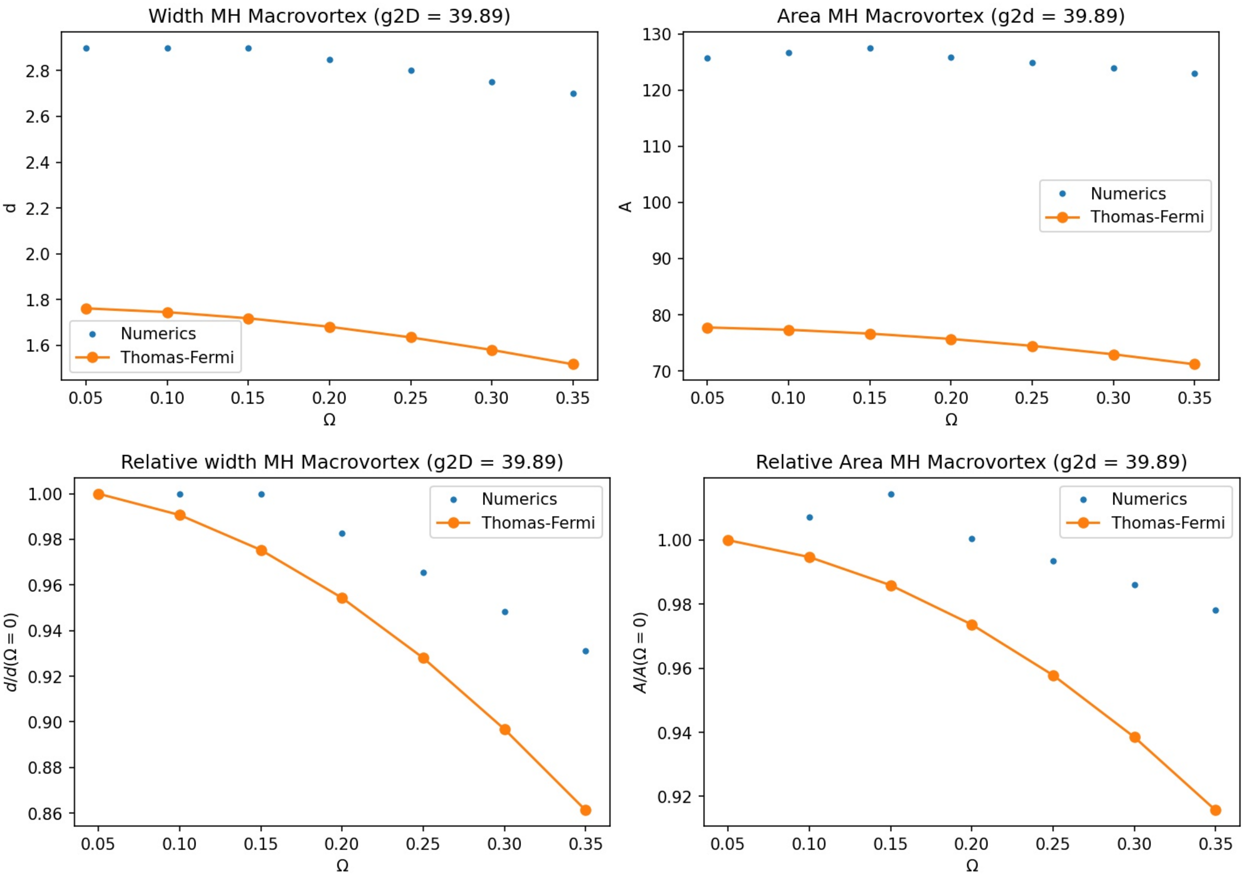

Figure 29 – Width $R_2 - R_1$ (left) and area $\pi\left(R_2^2 - R_1^2\right)$ (right) of the condensate as calculated numerically and by the Thomas-Fermi approximation given by Eqs.(4.62) and Eq.(4.63), for the Mexican Hat potential with $\lambda = 0.01$ and $g_{2D} = 39.89$.
Source: By the author.

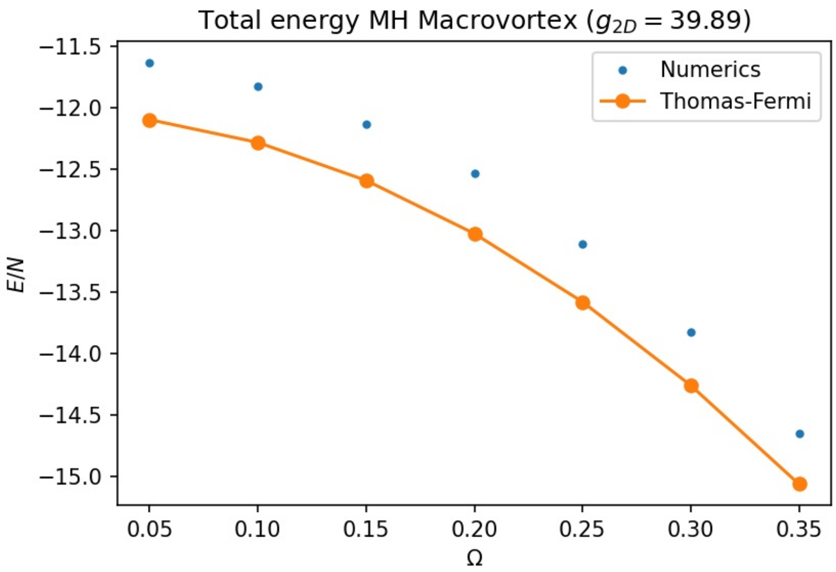

Figure 30 – Total energy as predicted by Eq.(4.65) for a condensate containing a macrovortex in the Mexican Hat potential, with $g_{2D} = 39.89$ and $\lambda = 0.01$. Source: By the author.

ical simulations. The disagreement in the chemical potential mainly drives the absolute values to be slightly off, but the overall trend is well reproduced.

4.2.2 Shifted Harmonic Oscillator

4.2.2.1 Macrovortex

For the SHO in a macrovortex configuration, as with the MH potential the velocity field of the fluid takes the form of Eq.(4.55):

$$\boldsymbol{v}_s = \frac{\nu}{\rho}\hat{\varphi}, \tag{4.68}$$

and with the SHO potential

$$V = \frac{1}{2}\left(\rho - \rho_0\right)^2, \tag{4.69}$$

the density profile becomes of the form

$$n = \frac{1}{2g_{2D}}\left[2\tilde{\mu} - \frac{\nu^2}{\rho^2} - \left(\rho - \rho_0\right)^2\right], \tag{4.70}$$

where once more $\tilde{\mu} = \mu + \nu\Omega$. If we demand the density to vanish at the boundaries R_1 and R_2 we can relate R_1, R_2 to ρ_0:

$$\rho_0 = \frac{\left(R_1 + R_2\right)\left(R_1^2 R_2^2 - \nu^2\right)}{2R_1^2 R_2^2}, \tag{4.71}$$

with $R_1^2 R_2^2 - \nu^2 > 0$. Using the mean radius and width notation, i.e ($R_2 > R_1$):

$$R = \frac{R_1 + R_2}{2}, \tag{4.72}$$

and

$$d = R_2 - R_1 \tag{4.73}$$

this can also be written as the cubic equation

$$R^3 - \left(\frac{d^2}{4} + \nu^2\right) R - \rho_0 \left(R^2 - \frac{d^2}{4}\right) = 0, \tag{4.74}$$

which can be solved for d:

$$d = 2\sqrt{\left(R^2 - \sqrt{\frac{R}{R - \rho_0}}\nu\right)}. \tag{4.75}$$

In turn, the chemical potential can be determined by imposing the boundary condition $n(R_1) = n(R_2) = 0$. In terms of R and d we have:

$$\tilde{\mu} = \frac{1}{8}\left[d^2 + 4\left((R - \rho_0)^2 + 4\nu^2 \frac{d^2 + 4R^2}{(d^2 - 4R^2)^2}\right)\right]$$

We can use Eq.(4.75) to rewrite the chemical potential in terms purely of R only:

$$\tilde{\mu} = \frac{1}{2R\,(R - \rho_0)}\,(2R - \rho_0)\left[R\left(2R^2 - 3R\rho_0 + \rho_0^2\right) - \sqrt{R\,(R - \rho_0)}\nu\right]. \tag{4.76}$$

We can also obtain an expression for $\tilde{\mu}$ by imposing the normalization condition $\int n d^2 r = 1$. If we then express this equation in terms of R and d and equate it to Eq.(4.76) we obtain the equation:

$$\frac{g_{2D}}{2\pi R d} = \frac{1}{2}R\,(R - \rho_0) + d^2\left(\frac{1}{8} - \frac{\rho_0}{24R}\right) + \frac{\nu^2}{2Rd}\ln\left(1 - \frac{2d}{2R + d}\right). \tag{4.77}$$

Equation (4.77) can be solved numerically for a given Ω and ν. The parameter Ω is setted as a parameter of the problem, and the value of ν can be related to Ω by the same procedure used in the MH situation: we demand that the equilibrium value of ν for a given Ω minimizes the free energy, obtaining:

$$\Omega\nu = \frac{\pi\nu^2}{4Rg_{2D}}\left\{4Rd\,(3\rho_0 - 2R) + \left[4R^2\,(3\rho - 2R) - d^2\,(2R - \rho_0)\right]\ln\left(1 - \frac{2d}{2R + d}\right)\right\}. \tag{4.78}$$

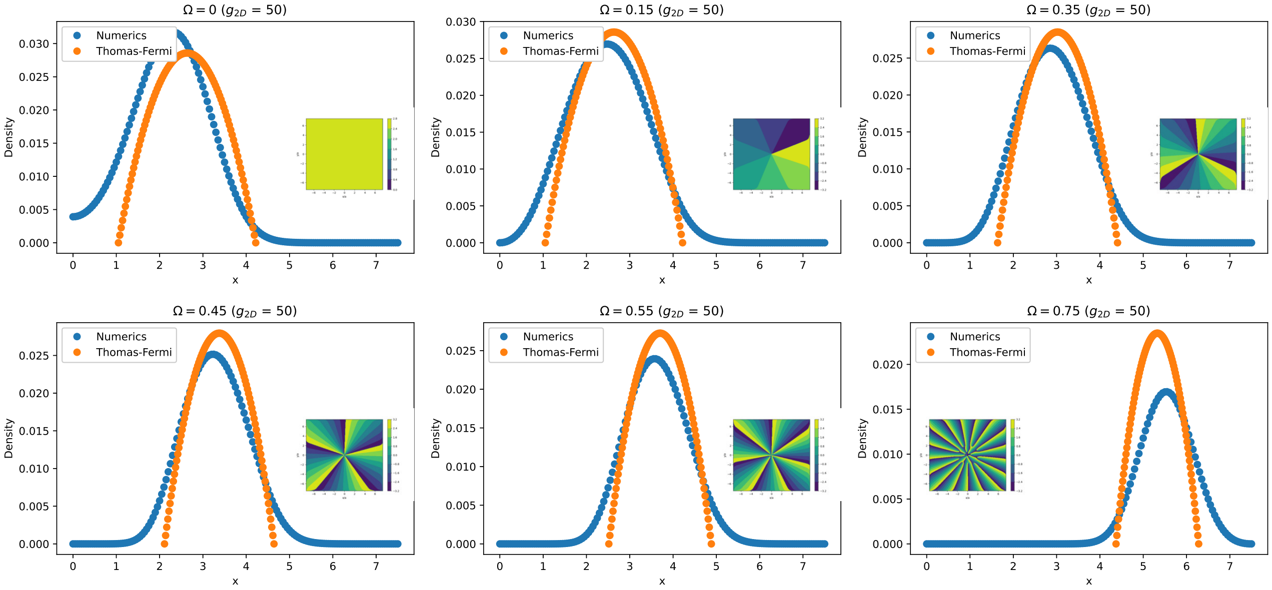

Figure 31 – Density profile for various angular speeds Ω, $g_{2D} = 50$ and the SHO potential with $\rho_0 = 2.5$. The blue dots represent the numerical profiles, extracted from a 1D cut from the full wave function (with the phase profile displayed in the inset), while the orange dots are the Thomas-Fermi prediction given by Eq.(4.70) with the numerical solutions of Eq.(4.77).
Source: By the author.

By solving the self-consistent system of equations, we obtain values for d and R, and relate ν and Ω by means of Eq.(4.78).

The parameter d can re expressed in terms of R by means of Eq.(4.75). This procedure allows us to obtain a numerical solution for R. Consequently, using Eq.(4.75) we obtain an expression for d, and hence for R_1 and R_2. Because the density profile is a polynomial of second degree, the knowledge of the roots and coefficients is sufficient for the complete characterization of the problem, and so every quantity of interest can be calculated.

The procedure outlined above was carried out with fixed $g_{2D} = 50$ and $\rho_0 = 2.5$, and some sample profiles can be seen in Figure 31. We picked $g_{2D} = 50$ to try to maintain consistency with the collective modes results (same reason for the choice of ρ_0), to be discussed ahead, and because the value was close enough to the MH analysis so as to allow comparison between the two potentials. Because this is a fairly low interaction parameter, we should not expect the results to agree much in terms of the normalization and chemical potential, but nevertheless there's a good overall agreement between the profiles.

We can see in Figure 32 the values of R_1 and R_2 compared to numerical simulations and various settled thresholds. It is clear from the data that the threshold of 10^{-2} is the one that better reproduces our model, and in analysis where this was relevant it was the

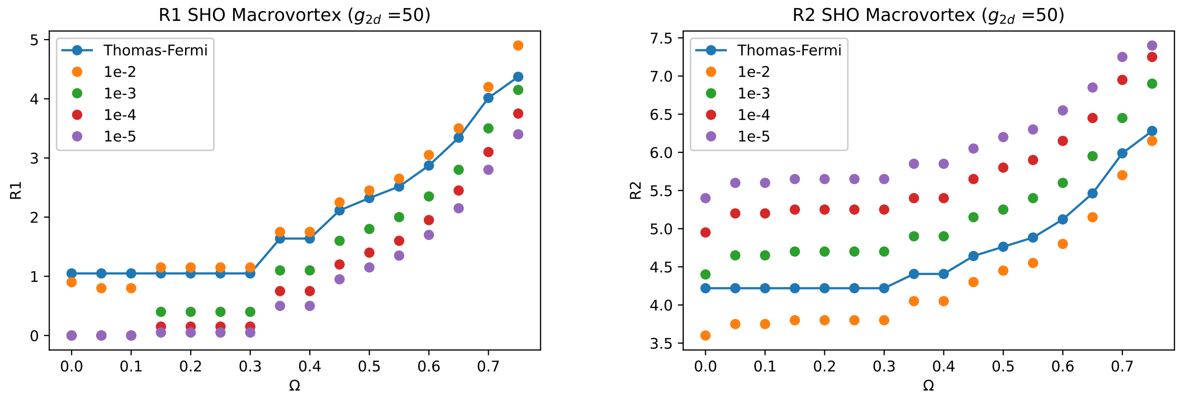
R1 SHO Macrovortex (g_{2d} =50)

R2 SHO Macrovortex (g_{2d} =50)

Figure 32 – Radii of the inner (left) and outer (right) boundaries of the condensate as a function of Ω, for the SHO potential with $\rho_0 = 2.5$ and $g_{2D} = 50$. The points are extract from numerical simulations, with the different thresholds being the value for which the density was considered to vanish.
Source: By the author.

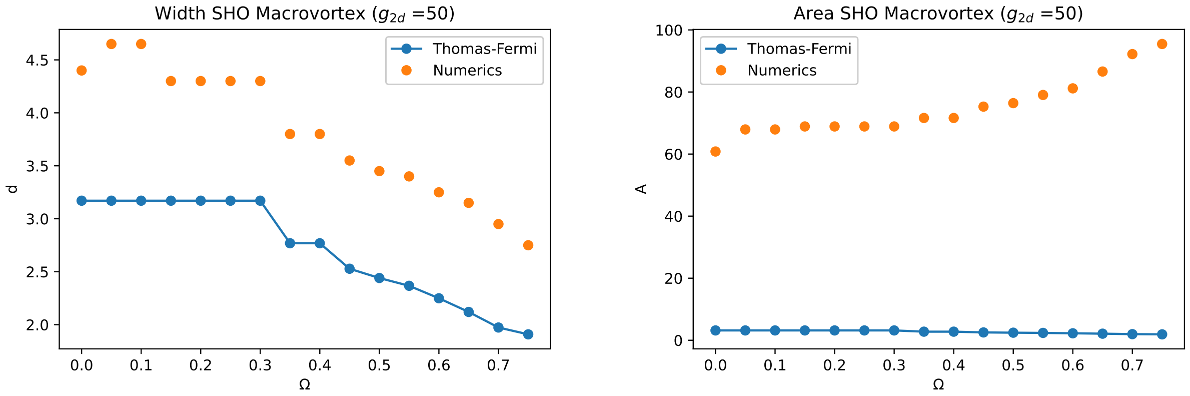
Width SHO Macrovortex (g_{2d} =50)

Area SHO Macrovortex (g_{2d} =50)

Figure 33 – Width (left) and area (right) as a function of Ω for the SHO potential in a macrovortex regime with $\rho_0 = 2.5$ and $g_{2D} = 50$.
Source: By the author.

value chosen as the threshold.

Not surprisingly, the values of the width and area are not in good agreement between our model and the numerics. The trend of decreasing width with Ω appears to be well reproduced, while the Thomas-Fermi model appears to predict a constant area as Ω increases but instead numerics appears to indicate an increase. This disagreement might get better for larger values of g_{2D}. Unfortunately, it was not possible to verify it concretly in our simulations because of limited computational resources.

Finally, in Figure 34 we can see how the energy and chemical potential of the Thomas-Fermi model compares to numerical results. As is typicall, the overall behavior is adequate but absolute values might diverge dramatically. Remarkably, the chemical potential was found to be in reasonable agreement when we have the discussion of the

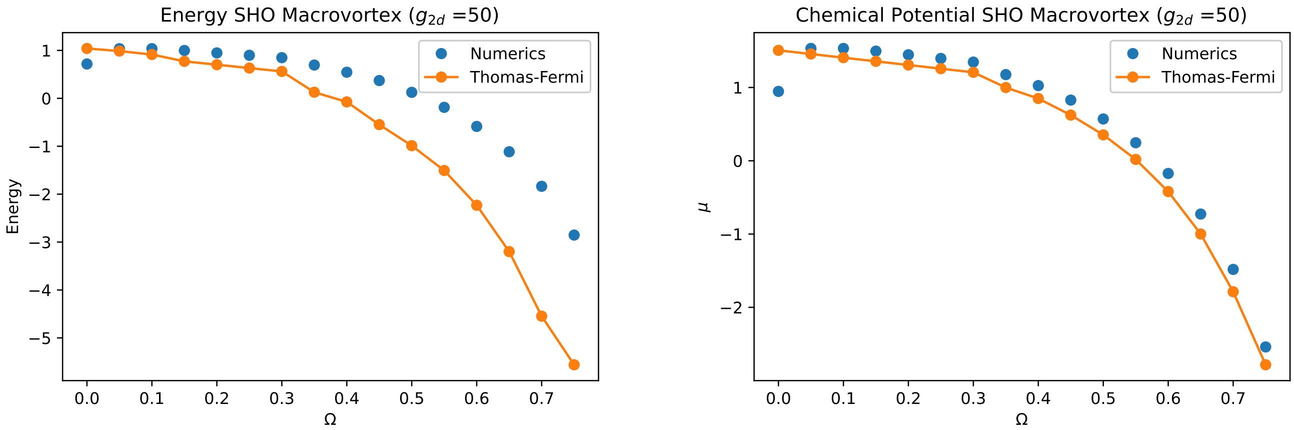

Figure 34 – Energy (left) and chemical potential (right) as a function of Ω, for the SHO potential in a macrovortex regime with $\rho_0 = 2.5$ and $g_{2D} = 50$. For the Thomas-Fermi points, the chemical potential was calculated using Eq.(4.76) while the energy was calculated using the full integral expression Eq.(4.27). Source: By the author.

Mexican Hat showed by Figure 30 in mind.

4.2.2.2 Vortex lattice

Once more, due to the polynomial quadratic form of the effective potential in this regime, it is possible to obtain simple analytical expressions for the Thomas-Fermi radii in this case. As in the MH potential case, the velocity field of the fluid mimics a rigid body:

$$\boldsymbol{v}_s = \boldsymbol{v}_{sb} \tag{4.79}$$

so that the Thomas-Fermi profile is of the form

$$n = \frac{1}{2g_{2D}} \left[2\mu - (\rho - \rho_0)^2 + \Omega^2 \rho^2\right]. \tag{4.80}$$

This has a simple analytic solution. In terms of the mean radius R and the width d we have

$$R = \frac{\rho_0}{1 - \Omega^2}, \tag{4.81}$$

and

$$d = \left(\frac{6}{\pi}\frac{g_{2D}}{\rho_0}\right)^{1/3}. \tag{4.82}$$

The chemical potential can be obtained through normalization and is simply:

$$\mu = \frac{1}{8}\left(1 - \Omega^2\right)\left(d^2 - 4R^2\Omega^2\right) \tag{4.83}$$

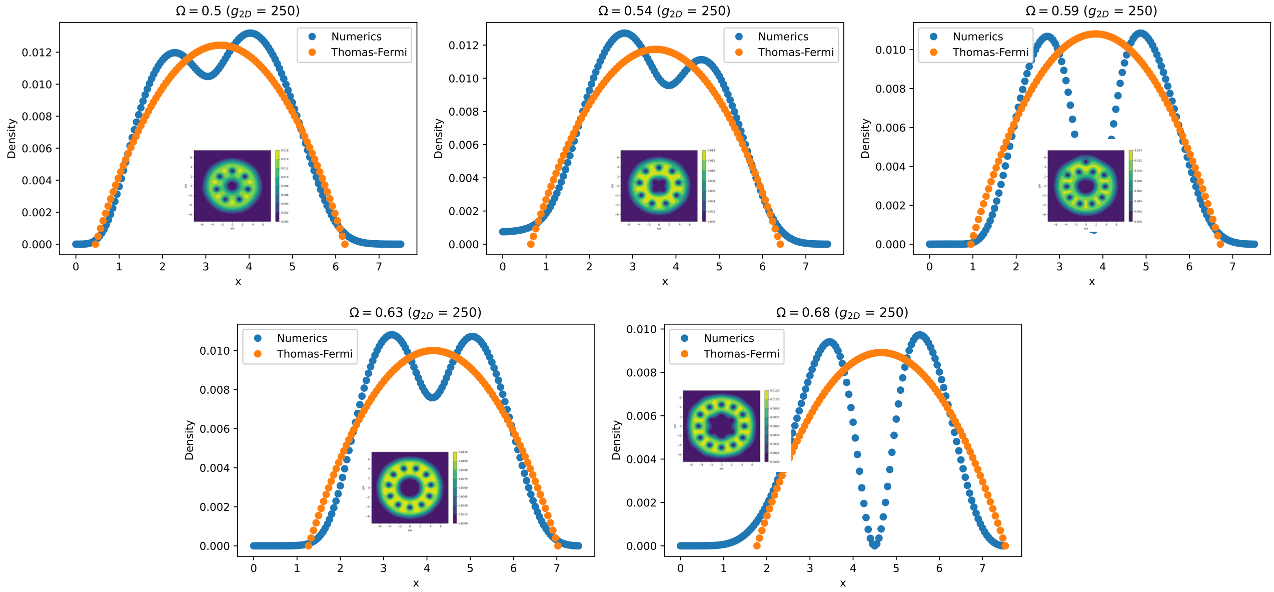

Figure 35 – Density profiles according to a 1D cut from a numerical simulation (with the full 2D profile shown in the inset) as well as the Thomas-Fermi density given by Eq.(4.80), for various angular velocities, $g_{2D} = 250$ and $\rho_0 = 2.5$. The many bumps that can be seen in the numerics are due to the vortices that happens to be at the cut location.
Source: By the author.

while the energy per particle is

$$E = \frac{3}{40} d^2 \left(1 - \Omega^2\right) - \frac{1}{2} \frac{\rho_0^2 \Omega^2}{\left(1 - \Omega^2\right)}. \tag{4.84}$$

In Figure 35 we show Eq.(4.80) plotted together with numerical simulations, for a range of different angular speeds. The interaction parameter $g_{2D} = 250$ was chosen because it was the smallest interaction parameter where we obtained a lattice for the range of angular speeds shown. Further increasing the angular velocity or the interaction parameter, however, would render the numerics unstable (the ground state outputed by the program was clearly not correct), unless big spatial grids and high simulation times were employed. Unfortunately, due to limited computational resources this option was not viable.

In Figure 36 we can see the radii as predicted by Eq.(4.81) and Eq.(4.82) and numerical values extracted for various thresholds. Overall, both 10^{-4} and 10^{-3} threshold appears to give a good fit to data, so we picked 10^{-3} as this was a common value in other analysis.

Having the numerical values of the radii, we can compare how the width and area changes as a function of Ω, according to the Thomas-Fermi predictions and numerical simulations. Plots can be seen in Figure 37. The numerics display a very erratic behavior

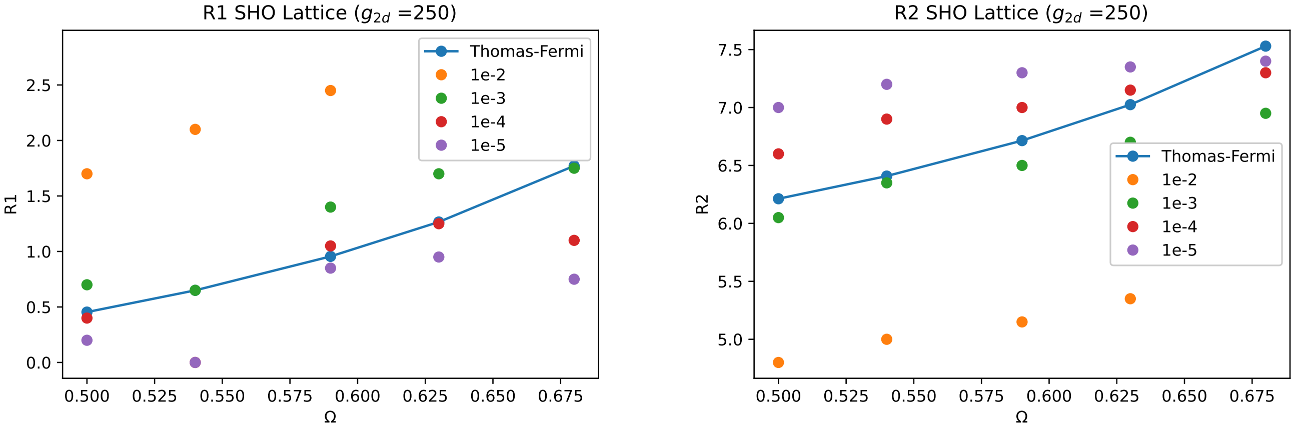

Figure 36 – Radii of the inner (left) and outer (right) boundaries of the condensate as a function of Ω, for the SHO potential in a lattice regime with $\rho_0 = 2.5$ and $g_{2D} = 250$. The points are extract from numerical simulations, with the different thresholds being the value for which the density was considered to vanish.
Source: By the author.

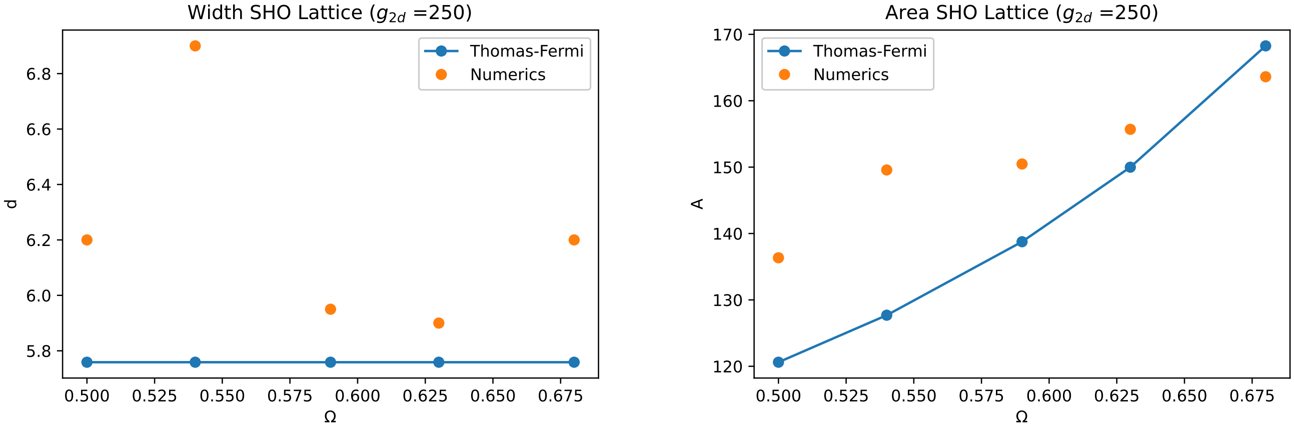

Figure 37 – Width (left) and area (right) as a function of Ω for the SHO potential in a lattice regime with $\rho_0 = 2.5$ and $g_{2D} = 250$.
Source: By the author.

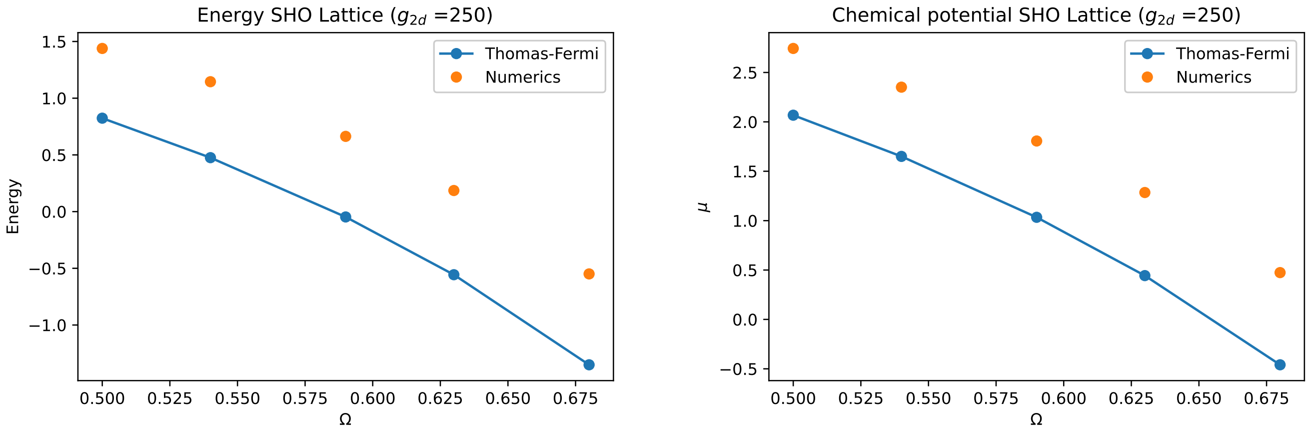

Figure 38 – Energy (left) and chemical potential (right) as a function of Ω, for the SHO potential in a lattice regime with $\rho_0 = 2.5$ and $g_{2D} = 250$. For the Thomas-Fermi points, the chemical potential was calculated using Eq.(4.83) while the energy was calculated using Eq.(4.84).
Source: By the author.

due to the fact that the exact location of the radii is affected by the many vortices in the bulk. Therefore it is not possible to discern an overall trend in the width behavior. As for the area, it appears that at least the increasing behavior of the area with Ω is well reproduced by the Thomas-Fermi predictions.

Finally, we shown in Figure 38 how the energy and chemical potential changes as a function of the angular speed Ω. Their behavior is quite similar, only changing from an overall scale in the vertical axis.

By now, we were able to ascertain that the Thomas-Fermi approximation is reasonable and we expect it to get better for decreasing importance of the kinetic energy term. This gives us additional security when using this approximation in our collective modes analysis, as we shall discuss next.

4.2.2.3 Main features of MH and SHO potential

In this subsection we analyze in more details the features our Thomas-Fermi model predicts to the MH and SHO potential.

Focusing in macrovortices for now, we can see in Figure 39 how the effective angular velocity Ω changes when we increase the central vortex charge, ν. As we already remarked, the SHO potential appears to act as a pinning potential, as we can see that even large increases in charge produces little no change in the effective angular velocity. In contrast, the MH potential is much more responsive. Therefore, we expect it to be easier to form lattices in MH potential when compared to the SHO potential, and this is indeed what we observed in our phase diagrams, Figure 15 and 20.

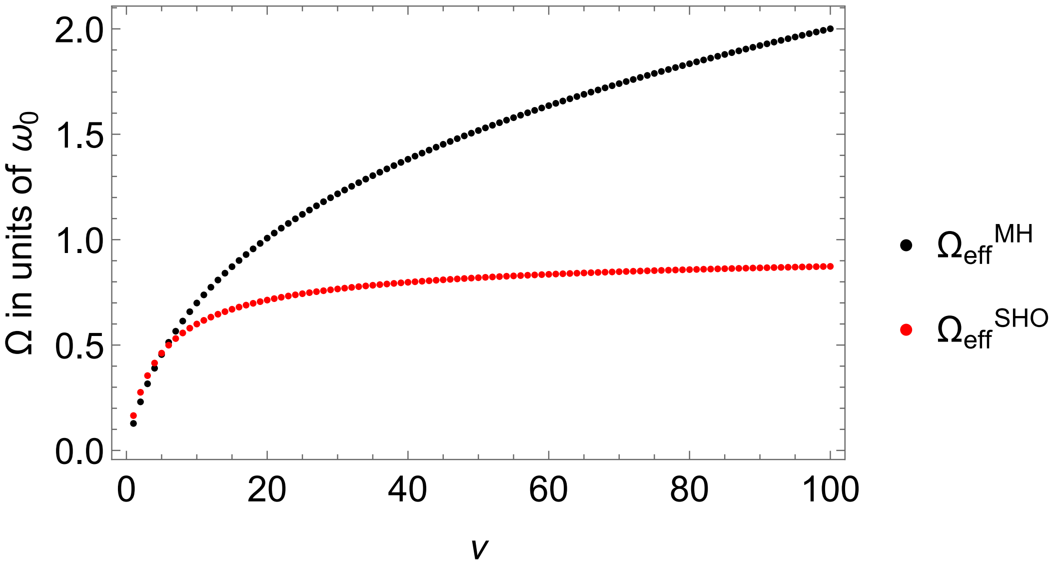

Figure 39 – Ω in units of the harmonic oscillator frequency ω_0 as a function of the macrovortex charge ν, as predicted by solving the self-consistent system of Thomas-Fermi equations, for the MH (red dots) and SHO (black dots) potentials.
Source: By the author.

We can further refine this analysis by comparing the evolution of geometric quantities such as the mean radius R, the width d and the area A. The behavior of this quantities as a function of Ω can be seen in Figure 40 and Figure 41 for macrovortices and lattices, respectively. For the SHO potential in a macrovortex configuration, we see that the area increases with ν while the width decreases after an initial plateau. Starting from a macrovortex configuration, therefore, it's unlikely to see a lattice formation, because as the bulk needs to get accomodated in the nearly constant width of the system, the energy cost of a vortex in the bulk increases. This behavior only gets more dramatic in a lattice configuration, where area appears to increases quickly while width remains constant (of course, in this case a lattice is already present in the gas). It's possible, therefore, to imagine a scenario where a vortex lattice becomes a macrovortex as the vortices in the bulk migrate to the hollow central region.

Similar conclusions can be reach for the MH potential: we have decreasing area and width with ν. This suggests that it is unlikely to see a transition to a vortex lattice by varying only Ω, for the same reasons outlined above. For the lattice configuration, area remains constant while width decreases. This again appears to favor a lattice to macrovortex transition if angular velocity continues to increase.

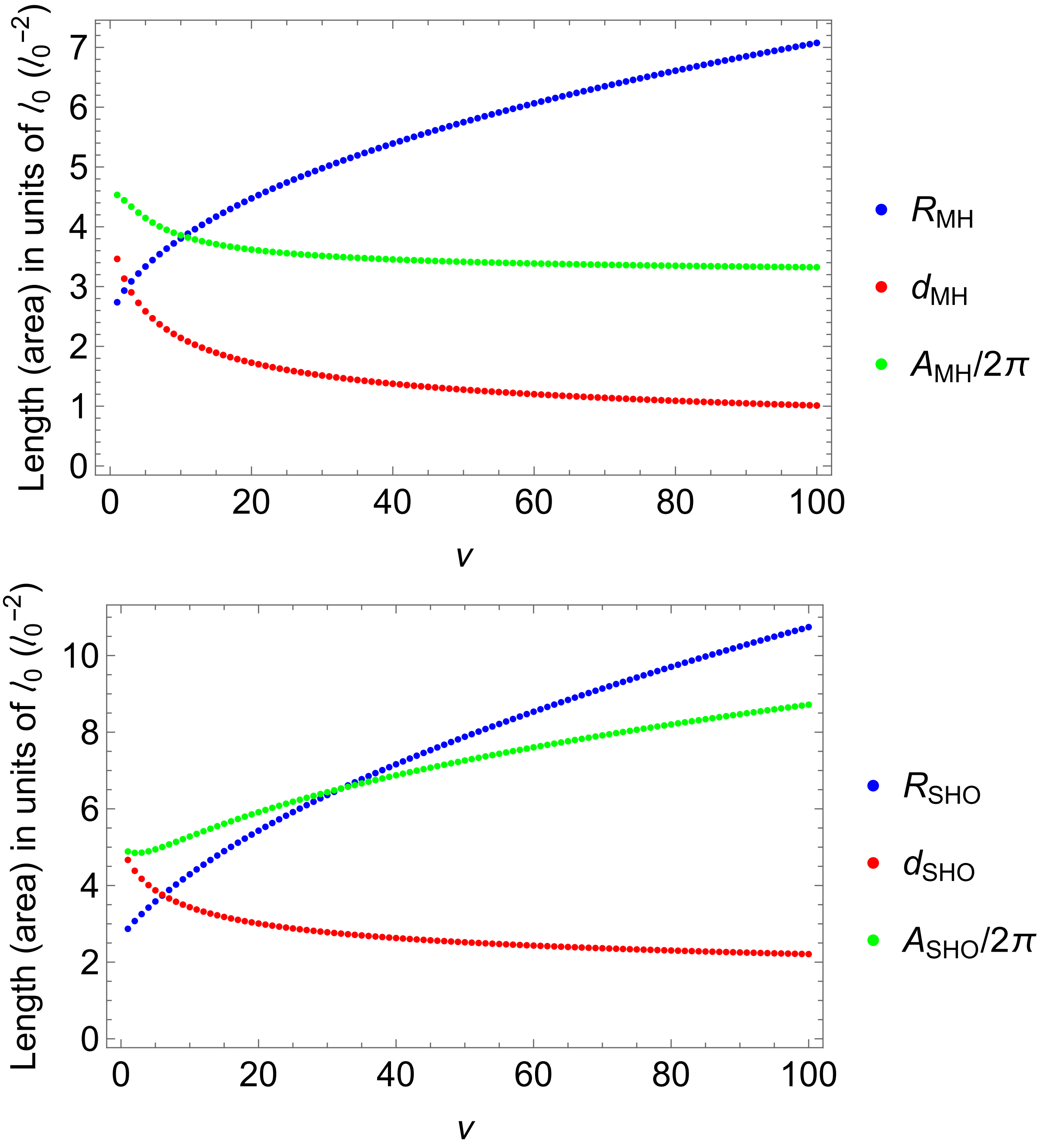

Figure 40 – Mean radius R, width d and area A as a function of ν for TF profiles in the MH (top) with $\lambda = 0.05$ and SHO (bottom) with $\rho_0 = 2.5$ potential in a macrovortex configuration. Lengths are in harmonic oscillator lengths $l_0 = a = (\hbar/M\omega_0)^{1/2}$.
Source: By the author.

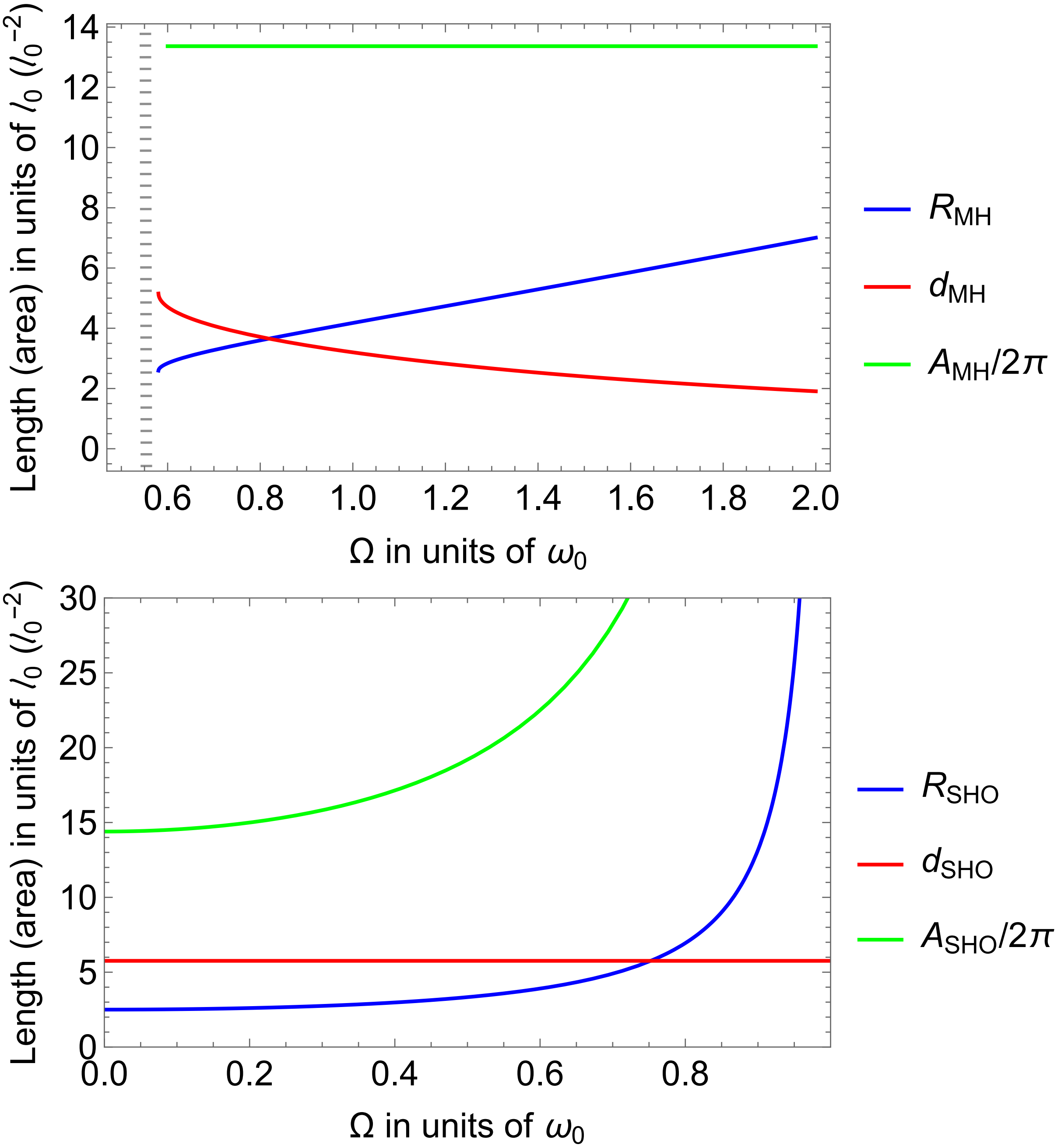

Figure 41 – Mean radius R, width d and area A as a function of Ω for TF profiles in the MH (top) with $\lambda = 0.05$ and SHO (bottom) with $\rho_0 = 2.5$ potential in a lattice configuration. Lengths are in harmonic oscillator lengths $l_0 = a = (\hbar/M\omega_0)^{1/2}$.

Source: By the author.

4.3 Collective Modes

We need to characterize the moments of the strength function for a system with states $|n\rangle$ and energies E_n:

$$S_{\pm}(E) = \sum_{n>0} \left| \langle n | \hat{F}^{\pm} | 0 \rangle \right|^2 \delta\left(E - E_n\right), \tag{4.85}$$

for the excitation operators:

$$\hat{F}_{\text{Monopole}} = \sum_i \left(x_i^2 + y_i^2\right), \tag{4.86}$$

and

$$\hat{F}^{\pm}_{\text{Quadrupole}} = \sum_j \left(x_j \pm i y_j\right)^2. \tag{4.87}$$

The quadrupole operator $F = \sum x^2 - y^2$ is a combination of $\hat{F}^{+}_{\text{Quadrupole}}$ and $\hat{F}^{-}_{\text{Quadrupole}}$. When there is no rotation these two perturbations are equivalent because the problem is axially symmetric, but when rotation is introduced there comes the necessity of differentiating between co and counter propagating modes. To characterize the strength function, we use the moments

$$m_p^{\pm} = \int_0^{\infty} dE \left[S_+\left(E\right) \pm S_-\left(E\right)\right] E^p, \tag{4.88}$$

and write sum rules of these moments that can be expressed in terms of expected values of the system's ground state (for more details, see Chapter 2).

4.3.1 Monopole

In this situation we found that the upper bound

$$\omega = \sqrt{m_3/m_1} \tag{4.89}$$

already yields good results. Since

$$m_1 = \frac{1}{2} \left\langle \left[\hat{F}_{\text{Monopole}}, \left[\hat{H}, \hat{F}_{\text{Monopole}}\right]\right] \right\rangle, \tag{4.90}$$

$$m_3 = \frac{1}{2} \left\langle \left[\left[\hat{F}_{\text{Monopole}}, \hat{H}\right], \left[\hat{H}, \left[\hat{H}, \hat{F}_{\text{Monopole}}\right]\right]\right] \right\rangle. \tag{4.91}$$

Using the potential

$$V(\rho) = -\frac{1}{2}\rho^2 + \frac{\lambda}{2}\rho^4, \tag{4.92}$$

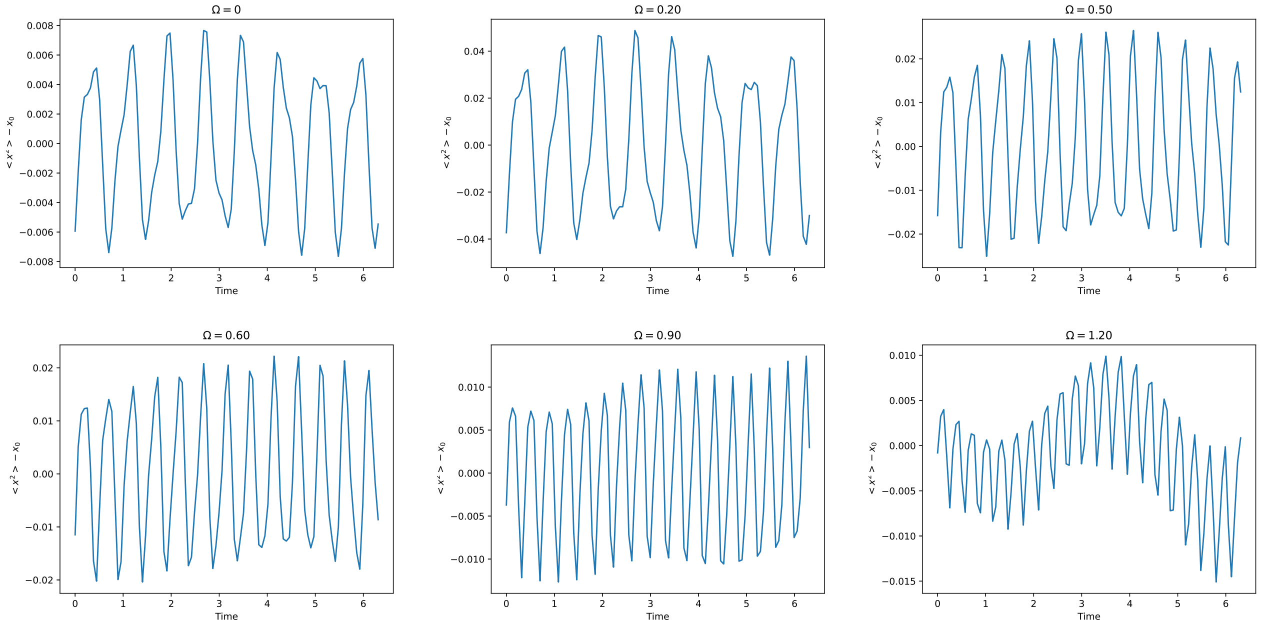

Figure 42 – $\langle x^2\rangle - x_0$ as a function of time (in units of ω^{-1}) for the Mexican Hat potential, $g_{3D} = 10$ and various Ω respectively. The term x_0 is the time average of $\langle x^2\rangle$, and we subtracted it to get rid of zero frequency peaks that would otherwise be present in the Fourier analysis.
Source: By the author.

we obtain

$$\omega^{\text{MH}}_{\text{Monopole}} = \omega_0\sqrt{2\frac{E_{kin}}{E_{ho}} - 2 + 2\frac{E_{int}}{E_{ho}} + 8\lambda\frac{\langle\rho^4\rangle}{\langle\rho^2\rangle}} \tag{4.93}$$

where

$$E_{kin} = \frac{1}{2}\left\langle p^2\right\rangle, \tag{4.94}$$

$$E_{ho} = \frac{1}{2}\left\langle \rho^2\right\rangle, \tag{4.95}$$

and

$$E_{int} = \frac{g_{2D}}{2}\left\langle \sum_{i\neq j}\delta\left(\boldsymbol{r}_i - \boldsymbol{r}_j\right)\right\rangle. \tag{4.96}$$

The interaction energy term can be handled by integration by parts or using the Virial Theorem (see Appendix A).

We now compare the predictions of Eq.(4.93) with numerical simulations. In order to excite the monopole modes numerically, we use real time simulation using as input a wave function calculated with imaginary time with a slightly higher g_{3D} than the one

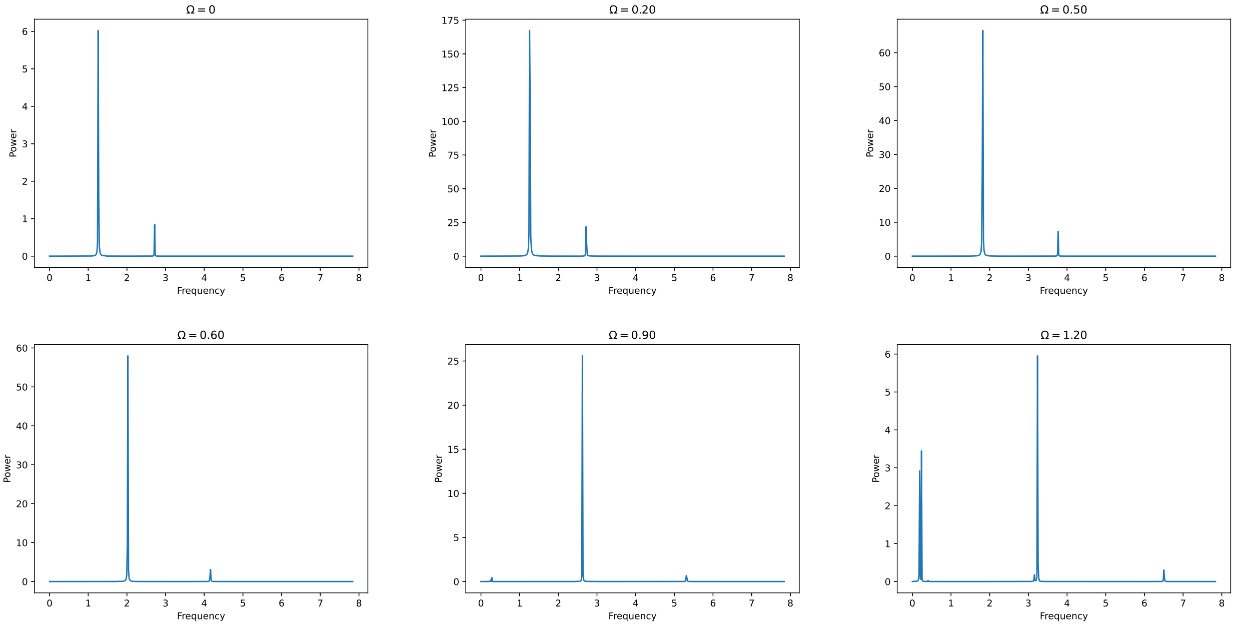

Figure 43 – Fourier transform of the signals shown in Figure 42.
Source: By the author.

used in the real time. We then generate 1000 wave function files, each corresponding to a different time point, and study how $\langle x^2 \rangle$ evolves with time. The results can be seen in Figure 42 and the corresponding Fourier transform in Figure 43. It can be seen that the signal is characterized by two peaks. The peak with larger power is the peak we chose to analyze; the second peak appears probably due to the presence of the hole in the condensate's center.

In the top part of Figure 44 we can see the results of this analysis, done for $g_{3D} = 10$ where we always have a central macrovortex and $g_{2D} = 200$ where the result is always a vortex lattice. We can see that the the frequency of the modes changes in "jumps": it stays constant, for instance, for $\Omega \in [0, 0.2]$ then it goes up for $\Omega = 0.3$. This is because the central vortex charge does not vary continuously with Ω - the observed frequency jumps happens precisely when there is an increase in the total charge. This behavior can be seen both for a macrovortex as well as a vortex lattice. The increase in frequency that takes places is a reflection of the lower compressibility of the system: the higher the charge of the vortices the more variation there is the velocity field and therefore the more cost in energy to compress it. The distribution of this vorticity in multiple vortices also makes the system more incompressible, as is reflect by the fact that for a same Ω, the frequency is higher for a vortex lattice than a macrovortex.

For the shifted harmonic oscillator, as with the Mexican Hat potential, we found

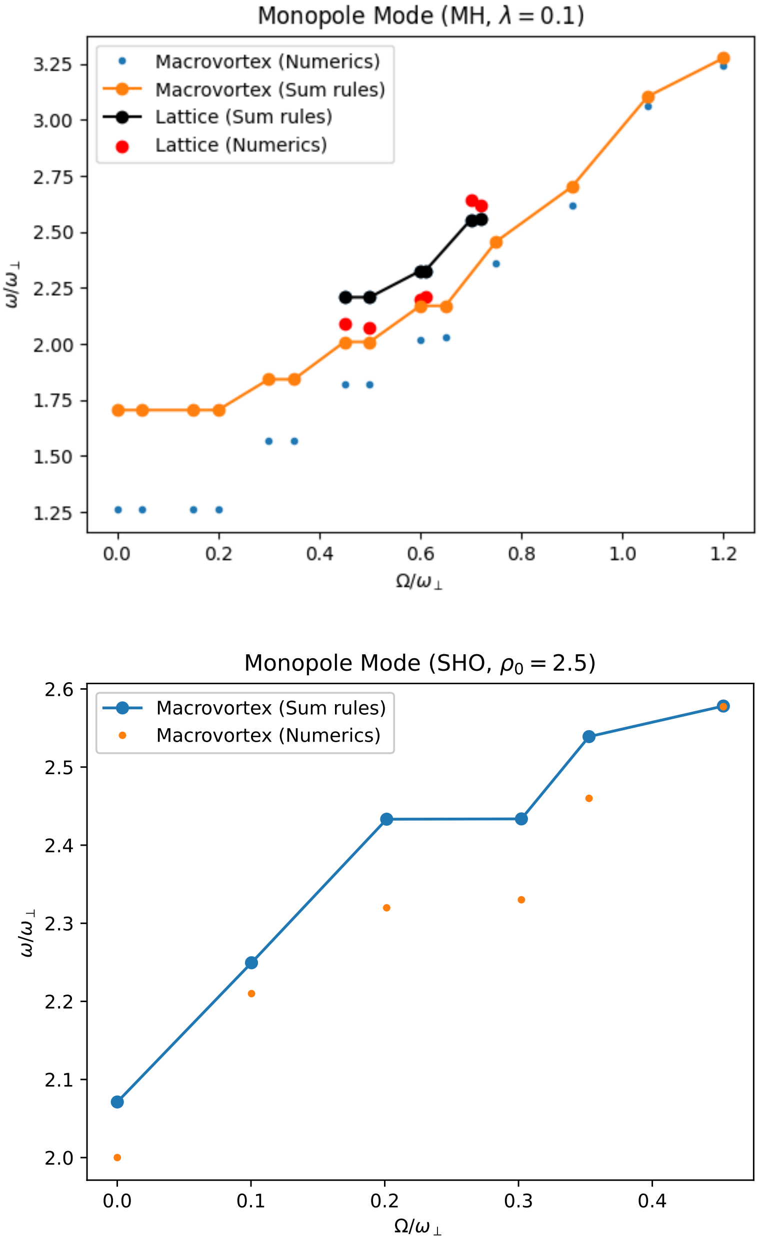

Figure 44 – Monopole modes frequency for the Mexican Hat potential with $\lambda = 0.1$ (top), and shifted harmonic oscillator potential with $\rho_0 = 2.5$ (bottom) as predicted by Eq.(4.93) and Eq.(4.98) respectively and numerical calculations. The points labelled as macrovortex were calculated with $g_{3D} = 10$ and all corresponds to a central macrovortex, while the points labelled lattice were calculated with $g_{3D} = 200$ and corresponds to a vortex lattice configuration. The SHO points were calculated with $g_{2D} = 50$.
Source: By the author.

it sufficient to use the simple upper bound $\sqrt{m_3/m_1}$, resulting in:

$$\omega^{\text{SHO}}_{\text{Monopole}} = \sqrt{2\frac{E_{kin}}{E_{ho}} + 2 + 2\frac{E_{int}}{E_{ho}} - \rho_0\frac{\langle\rho\rangle}{\langle\rho^2\rangle}} \tag{4.97}$$

or using the Virial theorem:

$$\omega^{\text{SHO}}_{\text{Monopole}} = \sqrt{1 + 3\frac{E_{kin}}{E_{ho}} + 3\frac{E_{int}}{E_{ho}}}. \tag{4.98}$$

As with the Mexican Hat potential, in the right of Figure 44 we noticed the same increase in frequency with the angular velocity, related to the system's compressibility. Unfortunately, we were not able to explore the lattice regime for the SHO potential. In order to obtain a vortex lattice we needed to greatly increase g_{3D}, and the resulting configurations were not stable when subject to the required perturbation to excited the monopole modes. Furthermore, increasing g_{3D} implies a bigger $\langle\rho\rangle$ which increases computational cost as the spatial grid required to the simulation increases in size. However, we could extract sensible Thomas-Fermi predictions of these behaviors as we shall now discuss.

If we use the Thomas-Fermi profiles for calculating the expected values in Eq.(4.98), the kinetic energy becomes

$$E_{kin} = \frac{1}{2}\nu^2\left\langle\frac{1}{\rho^2}\right\rangle, \tag{4.99}$$

for a macrovortex configuration or

$$E_{kin} = \frac{1}{2}\Omega^2\left\langle\rho^2\right\rangle, \tag{4.100}$$

for a vortex lattice.

The predicted values for the frequencies can be seen in Figure 45, for $g_{2D} = 100$ and $g_{2D} = 250$ for macrovortices and lattices, respectively. There's a substantial agreement between the numerical and analytical points. Once more, we can see that lattice points are slightly above the macrovortex points, reaffirming our discussion about the incompressibility of the gas. It is more clear now, however, that the change in frequency if not very large. Also, it can be seen that the overall frequency values of the MH potential are larger than in the SHO.

4.3.2 Quadrupole

For the quadrupole modes the situation is more complicated. We found that the simple upper bound $\sqrt{m_3/m_1}$ no longer gives a good estimate of the frequency of the

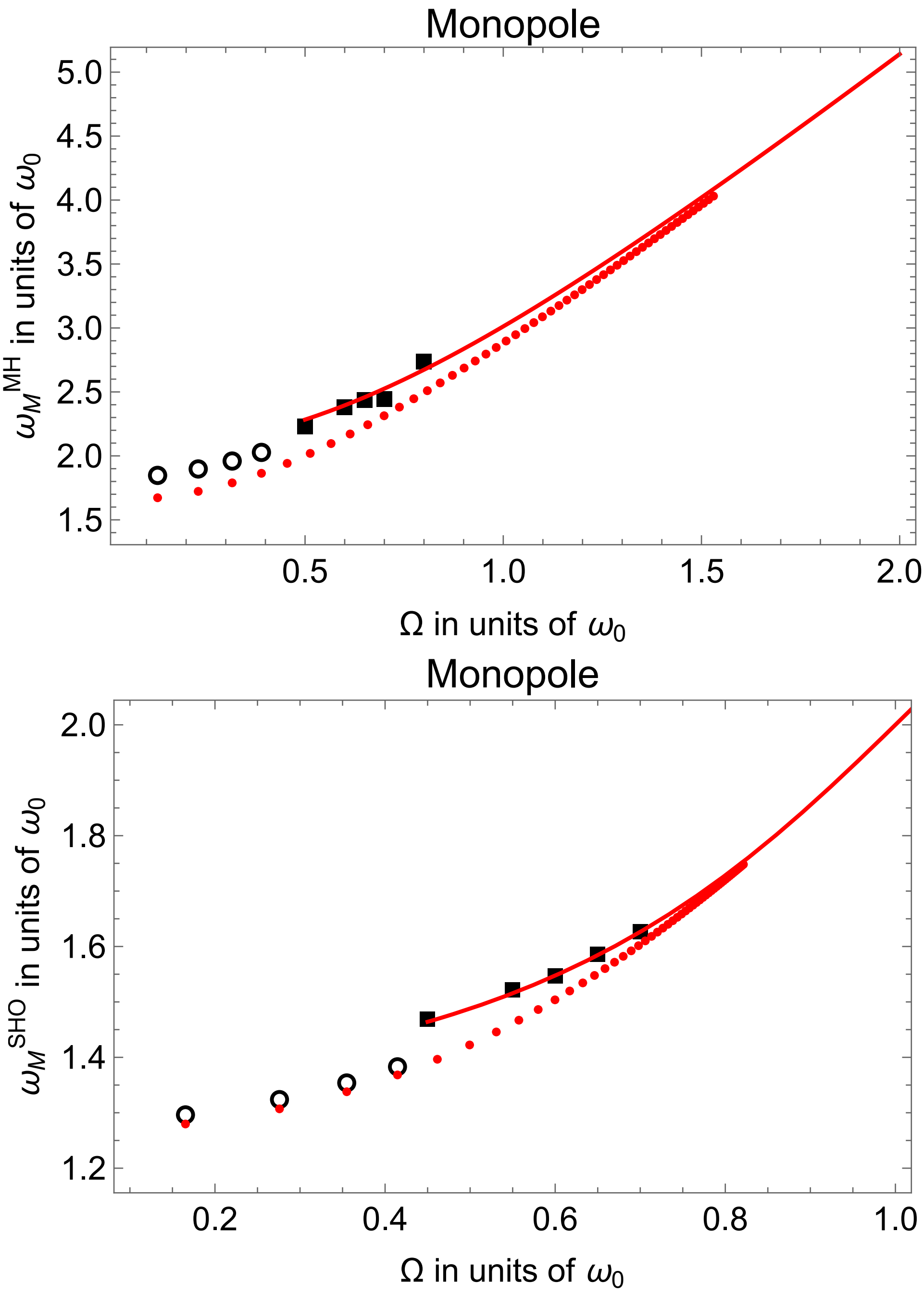

Figure 45 – Comparison of the monopole frequency obtained with the numeric solution of the GPE for the macrovortex (open circles) and vortex lattice (solid squares) configurations. The TF prediction, in a selected interval of frequencies, is shown by the filled points for the macrovortex and by the solid lines for the vortex-lattice. Macrovortex points were calculated with $g_{2D} = 100$ and lattice points for $g_{2D} = 250$.
Source: By the author.

mode, even if we use the generalized definition of the moments $\sqrt{m_3^\pm/m_1^\pm}$. Instead, our approach here is to suppose the strength function to be characterized by two modes:

$$S_\pm\left(E\right) = \sigma^\pm \delta\left(E - E_\pm\right), \tag{4.101}$$

with $\sigma^+ = \sigma^- = \sigma^0$ (because $m_0^- = \sigma^+ - \sigma^- = 0$). Then the following equations holds in virtue of the definition of the moments $m_p^\pm$ and some simple algebra:

$$m_1^+ = \sigma_0\left(E_+ + E_-\right), \tag{4.102}$$

$$m_{-1}^+ = \sigma_0\left(\frac{1}{E_+} + \frac{1}{E_-}\right) = \frac{m_1^+}{E_+E_-}, \tag{4.103}$$

$$m_2^- = \sigma_0\left(E_+^2 - E_-^2\right) = m_1^+\left(E_+ - E_-\right), \tag{4.104}$$

$$m_3^+ = \sigma_0\left(E_+^3 + E_-^3\right) = m_1^+\left(E_+^2 - E_+E_- + E_-^2\right), \tag{4.105}$$

$$m_4^- = \sigma_0\left(E_+^4 - E_-^4\right) = m_2^-\left(E_+^2 + E_-^2\right). \tag{4.106}$$

This results in a system of equations for the unknowns $E_\pm$, with solution

$$E_\pm = \frac{1}{2}\left[\sqrt{\left(\frac{m_2^-}{m_1^+}\right)^2 + 4\frac{m_1^+}{m_{-1}^+}} \pm \frac{m_2^-}{m_1^+}\right]. \tag{4.107}$$

This moments can be calculated without much difficulty, with exception of m_{-1}^+. We can, however, use Eq.(4.105) and Eq.(4.106) to write

$$\frac{m_3^+}{m_1^+} = \frac{m_4^-}{m_2^-} - \frac{m_1^+}{m_{-1}^+}, \tag{4.108}$$

so

$$\omega^{\text{MH}}_{\text{Quadrupole},\pm} = \frac{1}{2}\left[\sqrt{\left(\frac{m_2^-}{m_1^+}\right)^2 + 4\left(\frac{m_4^-}{m_2^-} - \frac{m_3^+}{m_1^+}\right)} \pm \frac{m_2^-}{m_1^+}\right]. \tag{4.109}$$

eq:monopoleSHOIn terms of commutators, we can straightforwardly compute the moments as:

$$m_1^+ = \left\langle\left[F_-, \left[H, F_+\right]\right]\right\rangle, \tag{4.110}$$

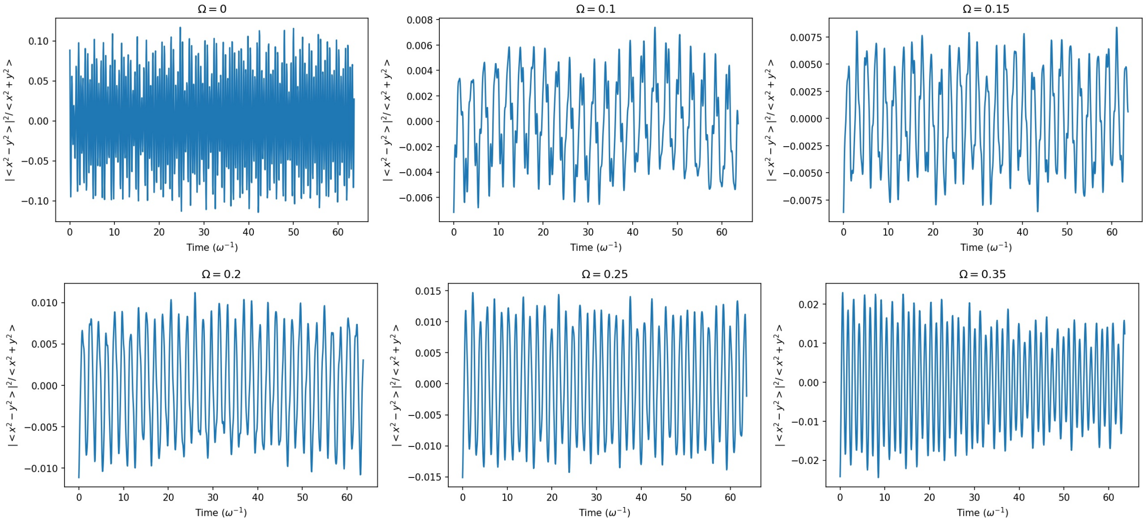

Figure 46 – Evolution of $\langle x^2 - y^2 \rangle / \langle x^2 + y^2 \rangle$ with time, for the Mexican Hat potential with $\lambda = 0.01$, $g_{2D} = 50$ and various angular velocities.
Source: By the author.

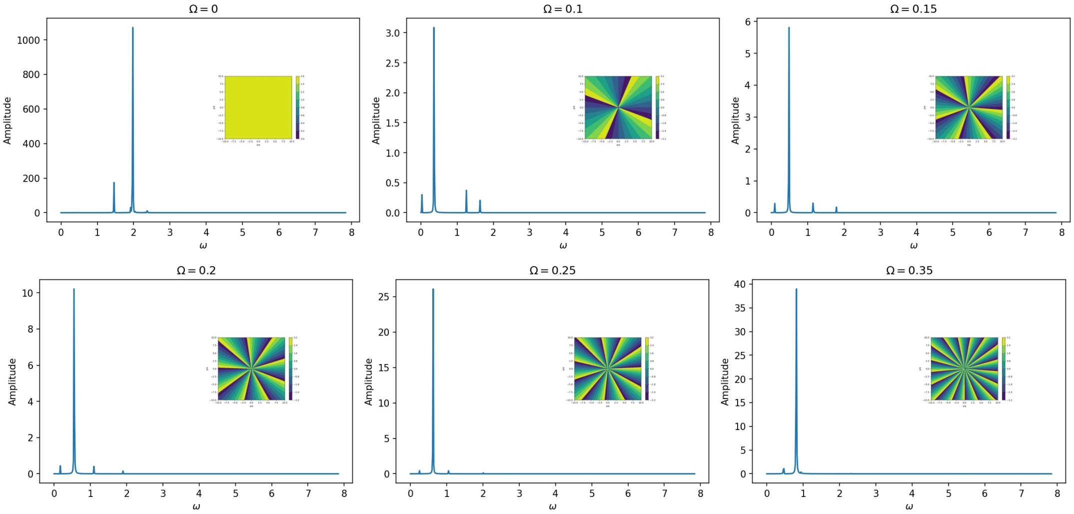

Figure 47 – Fourier transform of the time signals displayed in Figure 46. In the inset we show the phase structure of the condensate's phase structure for the given angular velocities.
Source: By the author.

$$m_2^- = \langle [[F_-, H], [H, F_+]] \rangle , \tag{4.111}$$

$$m_3^+ = \langle [[F_-, H], [H, [H, F_+]]] \rangle , \tag{4.112}$$

$$m_4^- = \langle [[[F_-, H], H], [H, [H, F_+]]] \rangle . \tag{4.113}$$

For the Mexican Hat potential, this results in

$$\frac{m_2^-}{m_1^+} = \frac{1}{\Omega}\frac{E_{rot}}{E_{ho}} - 4\Omega, \tag{4.114}$$

$$\frac{m_3^+}{m_1^+} = 2\left[\frac{E_{kin}}{E_{ho}} - 1 + 6\Omega - 3\frac{E_{rot}}{E_{ho}} + 3\lambda\frac{\langle\rho^4\rangle}{\langle\rho^2\rangle}\right], \tag{4.115}$$

and

$$\frac{m_4^-}{m_2^-} = 4\frac{\frac{E_{kin}}{E_{ho}} - 1 + 2\Omega^2 - \frac{3}{2}\frac{E_{rot}}{E_{ho}} + \frac{1}{4\Omega^2}\frac{E_{rot}}{E_{ho}} - 3\lambda\left(\frac{1}{2\Omega}\frac{\langle\rho^2 L_z\rangle}{\langle\rho^2\rangle} - \frac{\langle\rho^4\rangle}{\langle\rho^2\rangle}\right)}{1 - \frac{1}{4\Omega^2}\frac{E_{rot}}{E_{ho}}}. \tag{4.116}$$

We then compare the sum rules prediction with numerical simulations. In order to excite the quadrupole modes in the numerical simulations, we simulate the ground state wave function with imaginary time propagation using a slightly anisotropic potential in the x direction, making $\omega_x \to \omega_x + \delta\omega_x$, and use the resulting wave function as an initial state in a real time evolution simulation. We then track how $\langle x^2 - y^2\rangle$ changes with time, as can be seen in Figure 46, and extract the frequencies associated with this motion using a fast Fourier transform (Figure 47). This procedure typically produces 4 different peak frequencies, but sometimes fewer peaks can be discerned. We group these frequencies by hand, constructing series of values by presuming the change with Ω to be as smooth as possible.

The end result of this process is shown in Figure 48 for each branch of the frequencies predicted by Eq.(4.109). The numerical sequencies that fits best with the data were chosen as the numerical points. Unlike the monopole case, we were unable to study how these frequencies behave in lattices, because the vortex structure was very fragile. Frequently, we simulated a ground state with some given vorticity ν, and then found out that the frequency perturbation $\omega_x + \delta\omega_x$ did not preserve ν. To avoid these problems we worked only with small interaction parameters and careful checked that ν remained constant. As in the monopole case, we were able to derive sensible predictions using the Thomas-Fermi profiles, as we shall discuss further ahead.

The two branches shown in Figure 48 reflect modes co-rotating and anti-rotating with the condensate, and their splitting is proportional to the total angular momentum of the system. The mode anti-rotating eventually rotates at the same speed of the condensate yielding zero frequency modes. The other branch increases in frequency as the system becomes more incompressible, as in the monopole case.

We also did try a four mode sum rule approach, with two doubly degenerate modes, but found that results did not improve much when compared to the simple two modes used in Eq.(4.109). This is in contrast to the shifted harmonic oscillator, as we shall see next.

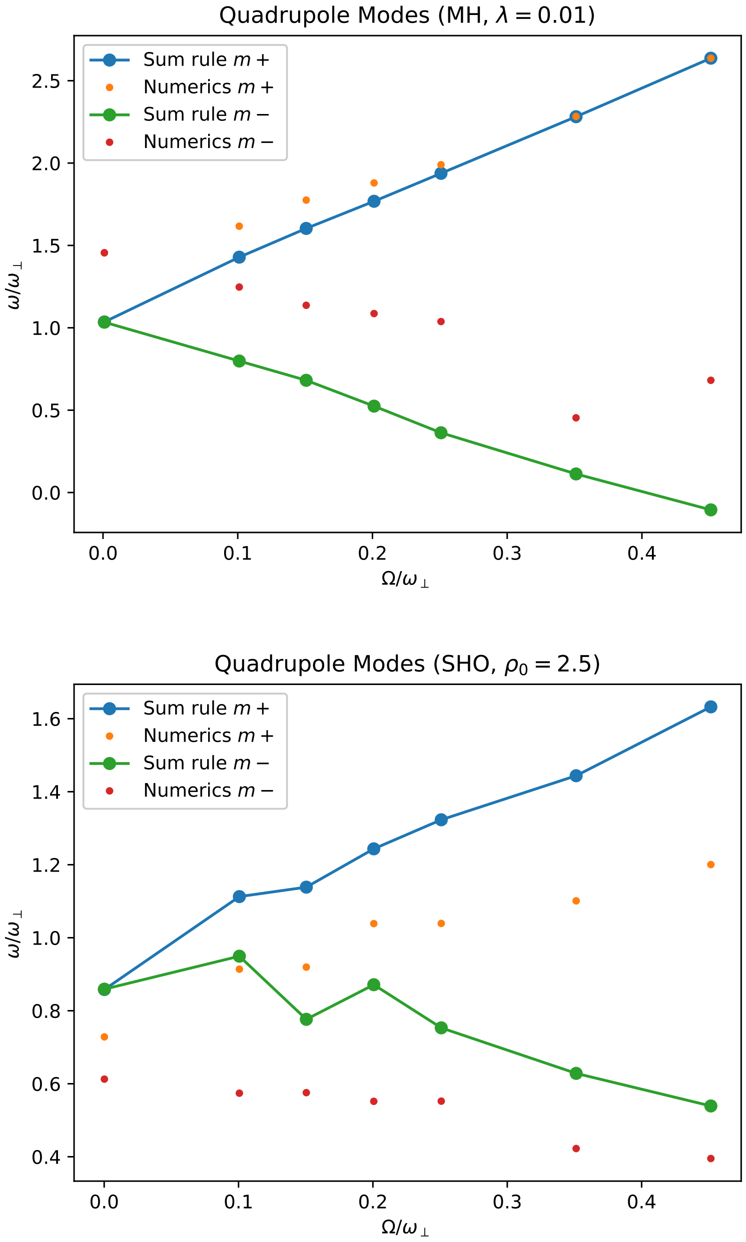

Figure 48 – Quadrupole mode frequencies for the Mexican Hat potential with $\lambda = 0.01$ (top) and for the shifted harmonic oscillator potential with $\rho_0 = 2.5$ (down), as predicted by sum rules Eq.(4.109) and by Eq.(4.127) respectively as well the numerical procedure outlined in the text. In both cases, $g_{2D} = 50$.
Source: By the author.

For the shifted harmonic oscillator, Eq.(4.114) still holds but Eq.(4.115) and Eq.(4.116) becomes:

$$\frac{m_3^+}{m_1^+} = 2\left[\frac{E_{kin}}{E_{ho}} + 1 + 6\Omega^2 - 3\frac{E_{rot}}{E_{ho}} - \frac{3}{4}\rho_0\frac{\langle\rho\rangle}{\langle\rho^2\rangle}\right] \tag{4.117}$$

and

$$\frac{m_4^-}{m_2^-} = 4\frac{\frac{E_{kin}}{E_{ho}} + 1 + 2\Omega^2 - \frac{3}{2}\frac{E_{rot}}{E_{ho}} - \frac{1}{4\Omega^2}\frac{E_{rot}}{E_{ho}} + \frac{3}{4}\rho_0\left(\frac{1}{2\Omega}\left\langle\frac{L_z}{\rho}\right\rangle\frac{1}{\langle\rho^2\rangle} - \frac{\langle\rho\rangle}{\langle\rho^2\rangle}\right)}{1 - \frac{1}{4\Omega^2}\frac{E_{rot}}{E_{ho}}}. \tag{4.118}$$

The resulting branches as well as the results of the numerical simulations can be seen in the bottom of Figure 48. In contrast to the Mexican Hat case, the splitting of the branches appears to be more slowly varying with Ω: $\omega_+ - \omega_- \sim 2.5$ in the Mexican Hat potential, but only ~ 1 in the shifted harmonic oscillator. Overall the frequencies in the SHO potential appears to be slightly below that of the Mexican Hat.

For the shifted harmonic oscillator we also tried a four mode approximation, i.e, we suppose the strength function to be characterized by

$$S_+(E) = \sigma_H\delta(E - E_H) + \sigma_L\delta(E - E_L), \tag{4.119}$$

$$S_-(E) = \sigma_H^\dagger\delta(E - E_H) + \sigma_L^\dagger\delta(E - E_L). \tag{4.120}$$

There are thus 4 modes, two of them being degenerated (σ and $\sigma^\dagger$). In terms of the moments, we have

$$m_0^- = \sigma_H + \sigma_L - \sigma_H^\dagger - \sigma_L^\dagger = 0, \tag{4.121}$$

$$m_{-1}^+ = \frac{\sigma_H}{E_H} + \frac{\sigma_L}{E_L} + \frac{\sigma_H^\dagger}{E_H} + \frac{\sigma_L^\dagger}{E_L}, \tag{4.122}$$

$$m_1^+ = \sigma_H E_H + \sigma_L E_L + \sigma_H^\dagger E_H + \sigma_L^\dagger E_L, \tag{4.123}$$

$$m_2^- = \sigma_H E_H^2 + \sigma_L E_L^2 - \sigma_H^\dagger E_H^2 - \sigma_L^\dagger E_L^2, \tag{4.124}$$

$$m_3^+ = \sigma_H E_H^3 + \sigma_L E_L^3 + \sigma_H^\dagger E_H^3 + \sigma_L^\dagger E_L^3, \tag{4.125}$$

$$m_4^- = \sigma_H E_H^4 + \sigma_L E_L^4 - \sigma_H^\dagger E_H^4 - \sigma_L^\dagger E_L^4, \tag{4.126}$$

a system of six equations for six unknowns. Solving this system of equations results in:

$$E_{H,L}^2 = \frac{1}{2}\left[\frac{m_4^-}{m_2^-} \pm \sqrt{\left(\frac{m_4^-}{m_2^-}\right)^2 - 4\frac{m_1^+}{m_{-1}^+}\left(\frac{m_4^-}{m_2^-} - \frac{m_3^+}{m_1^+}\right)}\right]. \tag{4.127}$$

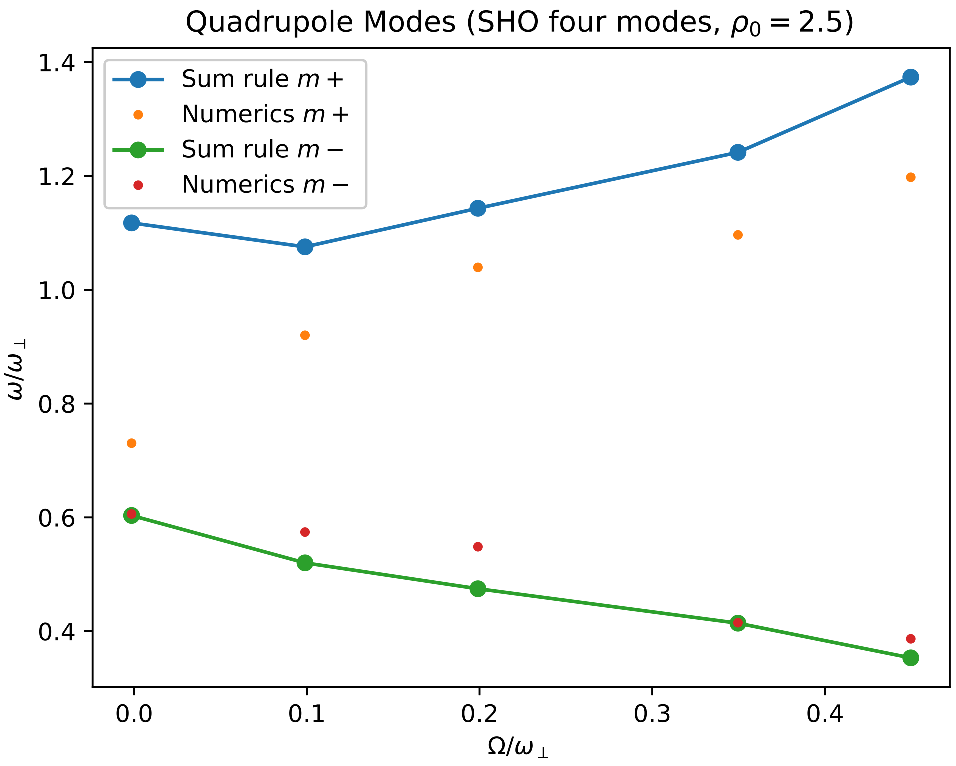

Figure 49 – Frequency of the quadrupole modes with a four modes assumption for the shifted harmonic oscillator with $\rho_0 = 2.5$ as predicted by Eq.(4.127), together with numerical data.
Source: By the author.

For this equation we need to calculate m_1^+/m_{-1}^+. The calculation of m_{-1}^+ is related to the system static response, and the details of the calculation are given in Appendix B. Here, we only mention that the calculation of this moment presumes the condensate to be described by a Thomas-Fermi approximation, and if $R \equiv R_1 + R_2$ and $d \equiv R_2 - R_1$ with $R_2 > R_1$ being the Thomas-Fermi radii, we obtain for a macrovortex scenario:

$$\frac{m_1^+}{m_{-1}^+} = \frac{8d^2\left[\left(d^2 - 4R^2\right)^2\left(3d^2 + 20R^2\right) - 48\left(d^2 - 20R^2\right)\nu^2\right]}{5\left(d^2 - 4R^2\right)^2\left(3d^4 + 40d^2R^2 + 48R^4\right)}, \tag{4.128}$$

where ν is the charge of the macrovortex. The resulting prediction for the frequency of the modes can be seen in Figure 49. Note that there is a frequency splitting even at $\Omega = 0$, although it is much larger for the sum rule prediction as compared to the numerical data. Overall, we found that this four mode scenario gives better results for the shifted harmonic oscillator, but not for the Mexican Hat potential. This is possibly due to the fact that the Thomas-Fermi approximation was not very good in the regime of parameter space used in the Mexican Hat potential.

Finally, seeking to alleviate the limitations described above, we analyzed the be-

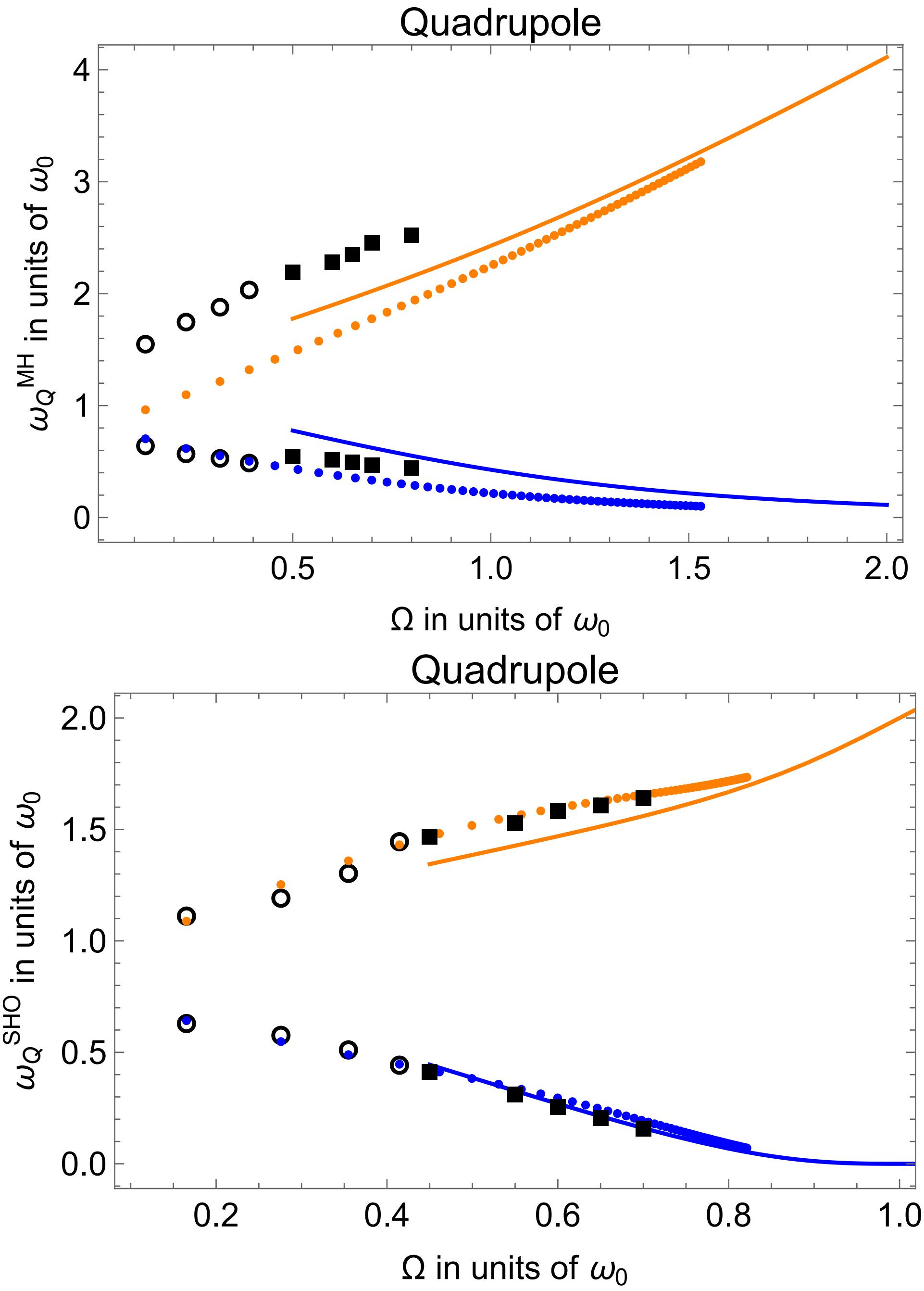

Figure 50 – Comparison of the quadrupole frequency obtained with the numeric solution of the GPE for the macrovortex (open circles) and vortex lattice (solid squares) configurations. The TF prediction, in a selected interval of frequencies, is shown by the filled points for the macrovortex and by the solid lines for the vortex-lattice. Macrovortex points were calculated with $g_{2D} = 100$ and lattice points for $g_{2D} = 250$. The parameters of the potential were $\lambda = 0.05$ for the MH and $\rho_0 = 2.5$ for the SHO.
Source: By the author.

havior of these modes when using the Thomas-Fermi approximation, as can be seen in Figure 50. The main conclusion of the mode splitting with increasing angular velocity still holds. We can also see that the lower branch approaches a zero value frequency for the SHO potential. This coincides with the critical angular velocity $\Omega = 1$ where the mean radius diverges. Also, as in the monopole case, we didn't see drastic changes in frequency when changing from macrovortex to lattices, but this time we see that the quadrupole frequency actually decreases in the SHO potential when changing to a lattice (but not in the MH, where the same monopole behavior is observed). It is unclear, however, if this behavior is substantiated by numerical calculations as we were unable to reproduce the numerical points in that frequency range.

5 CONCLUSION

Rotation in Bose-Einstein condensates is a topic that has attracted widespread research and discussion as of late. Seeking to better understand the elusive nature of vortices in more exotic potentials, the Mexican Hat and the shifted harmonic oscillator, which reproduces features of the bubble trap in some scenarios, we employed a set of tools in the hope of capturing their behavior and features over the phase diagram formed by the angular velocity Ω and the interaction parameter g_{2D}.

Our first approach was to use variational methods so as to obtain coefficients characterizing the wave function of the condensate in some simple linear combination. Because of the form of the potential, the wave function might have a central hole even at zero angular velocity, so we adapted the Gaussian function that served as envelop in certain scenarios. By varying the coefficients of the linear combination (or the total angular momentum in the more complicated scenario of the SHO potential), we obtained a phase diagram showing how the vortices charge change when varying the angular speed Ω and interaction parameter g_{2D}. Perhaps not surprisingly we found that at low Ω and g_{2D} the system prefers to form macrovortex configurations, as was already anticipated by Lundh in similar contexts (21): because the wave function's single particle energy varies faster than linearly with angular momentum, a pure state in terms of the coefficients of the linear combination is preferable. If, however, the interaction parameter is large enough the system's interparticle interaction eventually overcomes the energetic gain and it becomes once more optimal for the system to occupy a linear combination of states, leading to a vortex array. Using this variational functions we also predicted perturbation theory boundaries between the states with different angular momentum, allowing for predictions on when it was expected to see an increase in the vortex charge.

If the interaction parameter and/or the angular velocity are sufficiently high, as we already mentioned we expect the system to form vortex lattices. To predict the formation of these lattices and their behavior in terms of the variational function, we constructed a stability matrix formed by the second derivative of the energy with respect to the coefficients of the linear combination. By analyzing the sign of the eigenvalues of this matrix, we were able to predict leading order instabilities that formed the vortex lattice. Sadly, this was easier done in the MH potential than in the SHO, since we were not forced to use a modified ansatz in the MH potential and we were also able to simulate the MH for higher interaction parameters and angular velocities. Nevertheless, in the MH case we obtained clear boundaries between the macrovortex and lattice states and the corresponding predictions in terms of the distribution of the charge.

Since the use of the modified ansatz did not yield good predictions for the $\nu = 0$

line, we tried using the simple ansatz for the SHO potential and, excepting for mentioned line, were able to obtain a well behaved phase diagram together with the corresponding predictions to the transition to vortex lattices. As we noted, it appears to be harder to break a macrovortex in the SHO potential, as can be seen by the larger region of the phase space occupied by the macrovortex phase.

The results of our variational analysis were used in numerical simulations with imaginary time propagation. This algorithms depends in supplying an initial wave function for the program, and we found that supplying the wave function calculated by variational calculations leaded for more stable and consistent results than when using wave functions calculated numerically for similar parameters or analytically defined wave functions. Quite generally we found a good agreement between the predictions of the variational and numerical calculations with respect to the vortex charge and charge distribution - provided that we do not use high interaction parameters and angular speeds. One feature of notice is that the angular velocity interval between states of different vortex charge becomes narrower as the total charge increases, reaching a point when even minute changes in angular velocity results in dramatic change in the vortex charge. The formation of lattices is also favored if the central region of the condensate has an appreciable atom density: then it becomes energetically favored for the condensate to distribute its charge among charge 1 vortices instead of concentrating the charge in a single vortex, since this option results in a condensate with a smaller volume.

To gain better insights over the vortices behavior with angular velocity, we adapted Thomas-Fermi models to our two potentials, which allow for more simple mathematical models and the direct determination of geometric quantities of interest, such as the width and the area of the condensate as a function of the angular velocity. For instance, we can inquire in how efficiently angular momentum can be transferred to the fluid. As we anticipated in the discussion of the phase diagram, it appears that the SHO acts as a pinning potential, stabilizing the macrovortex configuration. It is thus much easier to achieve higher macrovortex charges for lower variations of angular velocities - the angular momentum is more efficiently transferred to the fluid.

Explanations can then be advanced in terms of the predicted geometrical behavior of the Thomas-Fermi profiles. We reached similar conclusions for sightly different reasons. For instance, for the SHO potential in a macrovortex configuration, the area increases with ν, while the width decreases after an initial plateau. This means that if for a certain interaction parameter the system starts in a macrovortex configuration, we do not expect a vortex lattice to form: since the area increases constant with decreasing width, the bulk of the gas where the condensate is able to host vortices get scarcer and the most likely scenario is for vortices to form in the hole.

This behavior is accentuated in a lattice configuration, where the area increases more drastically while the width remains constant. This allows for a scenario were we start with a vortex lattice, increase angular velocity and start to observe vortices migrating for the central region as more vortices form in the bulk, but then stabilize in a configuration populated by vortices in the central region and the bulk.

In the MH for the macrovortex configuration both the area and the width decreases with ν. This suggests that a change for a vortex lattice is unlikely varying only the angular velocity, as there will be less bulk area available to host the vortices. For the lattice configuration, area remains constant while width decreases. This makes it likely to the system to transition to a macrovortex scenario if the angular velocity continues to increase.

For providing yet another way of studying vortices in this potentials, we turned our look for the collective modes of the gas. We studied both the monopole breathing oscillations and the quadrupole in plane motion, seeking to understand how the vortices change the frequency of the mode. By using the sum rule methodology, we derive multiple expressions for these frequencies.

For monopole frequencies and the MH potential, the results were quite direct and simple: an increasing Ω results in increasing frequencies provided there's a change in the vortex charge or charge distribution, as evidenced by multiple plateaus formed by varying Ω and constant charge. We also found that for the same total charge, a vortex lattice has a corresponding slightly higher monopole frequency, a result we attribute to the lower compressibility of the gas when there are multiple vortices populating the gas' bulk. Finally, we note that typical numerical values were slightly lower than the sum rules predictions. This is expected, however, because those predictions were based in the ratio m_3/m_1 which provides only an upper bound.

To study the lattice points we used the Thomas-Fermi predictions, since the numerics were rendered unstable, having achieved similar conclusions.

Analysis for the quadrupole modes, while more complicated to execute, yielded similar conclusions for both potentials. As with the SHO potential in the monopole mode, we were not able to obtain lattice points because the resulting perturbation applied to the wave function disturbed the vortex configuration, so we limited ourselves only to macrovortex configurations (latter, we were able to study lattice points when using the Thomas-Fermi approximation). With increasing Ω there were two branches of the quadrupole modes, representing modes with angular momentum in the same and opposite direction of the rotation. The splitting between these branches increases with the angular velocity, and as with the harmonic oscillator, can be used to measure the rotation of the gas (24). With a two modes assumption, the frequencies merge at $\Omega = 0$, but with a four mode assumption they are separated even at $\Omega = 0$, a feature that can also be seen in our numerical methods. In general, agreement between the numerics and sum rules was better when using a four mode assumption, but care must be taken when using the four modes because the calculations required us to use the Thomas-Fermi model (a model that we verified to be reasonable when using the range of parameters of these works). When using the Thomas-Fermi approximation we confimed this conclusions, but notice that in the SHO potential the macrovortex to vortex lattice transitions actually causes a decrease in frequency. This behavior was not seen in the numerics, but we did not obtain numerical points for high Ω values were this difference seems more dramatic.

All in all, using collective modes for studying vortices appears to be promising for higher angular velocities and interaction parameters. Since our phase diagram considerations suggests that the boundaries of phases with different total charges gets narrower as we increase the angular velocity, the corresponding change in frequency of the collective modes due to the increasing charge can be analyzed. We also expect that the macrovortex to lattice transition might yield some signature in the frequency of the collective modes. We already know that a lattice has a higher frequency than a macrovortex, at least for the MH potential, and perhaps this knowledge can be used to derive boundaries in the phase diagram, allowing for confirmation and extension of our analysis of the stability matrix.

In a future work we want to improve our variational phase-diagram result, including higher values for the external rotation and for the atomic interaction to better map the experimental conditions. For that, we intend to use the Bogoliubov de Gennes equations to track the system dynamic instability and then to recalculate the system phase diagram with less computational cost. Our method and predictions might serve as a guide to optimize the achievement and detection of important structures in the quantum gases experiments, such as vortex lattices and giant vortex (49).

REFERENCES

1 BOSE, S. N. Plancks gesetz und lichtquantenhypothese. **Zeitschrift für Physik**, v.26, n.1, p. 178-181, Dec. 1924. ISSN 1434-6001.

2 ANDERSON, M. H. *et al.* Observation of Bose-Einstein condensation in a dilute atomic vapor. **Science**, v.269, n. 5221, p. 198-201, July 1995. ISSN 0036-8075.

3 PETHICK, C. J.; SMITH, H. **Bose-Einstein condensation in dilute gases**. 2nd. ed, Cambridge: Cambridge University Press, 2008. 585 p. ISBN 9780511802850.

4 FETTER, A. L. Rotating vortex lattice in a Bose-Einstein condensate trapped in combined quadratic and quartic potentials. **Physical Review A**, v. 64, n.6, p.063608-6, 2001. ISSN 10941622.

5 BRETIN, V. *et al.* Fast rotation of a Bose-Einstein condensate. **Physical Review Letters**, v. 92, n. 5, p. 050403-4, 2004. ISSN 10797114.

6 ZOBAY, O.; GARRAWAY, B. M. Two-dimensional atom trapping in field-induced adiabatic potentials. **Physical Review Letters**, v. 86, n. 7, p. 1195-1198, Feb. 2001. ISSN 0031-9007.

7 BUTTS, D. A.; ROKHSAR, D. S. Predicted signatures of rotating Bose-Einstein condensates. **Nature**, v. 397, n. 6717, p. 327-329, Jan. 1999. ISSN 0028-0836.

8 EINSTEIN, A. **Quantentheorie des einatomigen idealen gases**. [*S.l.*]: Wiley, 2005. v.1. 237-244 p.

9 SALINAS, S. R. A. **Introduction to statistical physics**. New York: Springer, 2001. 390 p. (Graduate Texts in Contemporary Physics). ISBN 978-1-4419-2884-9.

10 GRIFFITHS, D.J. **Introduction to quantum mechanics**. 2nd. ed, Lebanon, Indiana: Pearson Prentice Hall, 2004. 480 p. ISBN 0131118927.

11 BAGNATO, V.; KLEPPNER, D. Bose-Einstein condensation in low-dimensional traps. **Physical Review Letters**, v. 123, n. 16, p. 160403, Oct. 2019. ISSN 0031-9007.

12 TONONI, A.; SALASNICH, L. Bose-Einstein condensation on the surface of a sphere. **Physical Review Letters**, v. 123, n. 16, p. 160403, Oct. 2019. ISSN 0031-9007.

13 MÓLLER, N. S. *et al.* Bose-Einstein condensation on curved manifolds. **New Journal of Physics**, v. 22, n. 6, 2020. ISSN 13672630.

14 CHIN, C. *et al.* Feshbach resonances in ultracold gases. **Reviews of Modern Physics**, v. 82, n. 2, p. 1225-1286, Apr. 2010. ISSN 0034-6861.

15 PITAEVSKII, L.; STRINGARI, S. **Bose-Einstein condensation and superfluidity**. New York: Oxford University Press, 2016. 567 p. ISBN 978-0-19-875888-4.

16 STOOF, H. T.; GUBBELS, K. B.; DICKERSCHEID, D. B., **Ultracold quantum fields**. Dordrecht: Springer Netherlands, 2008. v. 2009. 485 p. (Theoretical and Mathematical Physics, 2). ISSN 1864-5879. ISBN 978-1-4020-8762-2.

17 LANDAU, L. D.; LIFSHITZ, E. M. **Quantum mechanics**. 3rd. ed, Oxford: Pergamon Press, 1977. 458 p. ISBN 9783527315314.

18 ABRIKOSOV, A. The magnetic properties of superconducting alloys. **Journal of Physics and Chemistry of Solids**, v. 2, n. 3, p. 199-208, Jan. 1957. ISSN 00223697.

19 ABO-SHAEER, J. R. *et al.* Observation of vortex lattices in Bose-Einstein condensates. **Science**, v. 292, n. 5516, p. 476-479, Apr. 2001. ISSN 0036-8075.

20 KAVOULAKIS, G. M.; MOTTELSON, B.; PETHICK, C. J. Weakly interacting Bose-Einstein condensates under rotation. **Physical Review A**, v. 62, n. 6, p. 063605, Nov. 2000. ISSN 1050-2947.

21 LUNDH, E. Multiply quantized vortices in trapped Bose-Einstein condensates. **Physical Review A**, v. 65, n. 4, p. 043604, Mar. 2002. ISSN 1050-2947.

22 ARFKEN, G. **Mathematical methods for physicists**. 3rd. ed, San Diego: Academic Press, Inc. 1985.

23 KIMURA, T.; SAITO, H.; UEDA, M. A variational sum-rule approach to collective excitations of a trapped Bose-Einstein condensate. **Journal of the Physical Society of Japan**, v. 68, n. 5, p. 1477-1480, May 1999. ISSN 0031-9015.

24 ZAMBELLI, F.; STRINGARI, S. Quantized vortices and collective oscillations of a trapped Bose-Einstein condensate. **Physical Review Letters**, v. 81, n. 9, p. 1754-1757, Aug. 1998. ISSN 0031-9007.

25 FETTER, A. L. Rotating trapped Bose-Einstein condensates. **Laser Physics**, v. 18, n. 1, p. 1-11, Jan. 2008. ISSN 1054-660X.

26 TONG, D. **Lectures on the quantum Hall effect**. Jan. 2016. Available at: http://arxiv.org/abs/1606.06687. Access at: 11/10/2022.

27 FETTER, A. L. Rotating trapped Bose-Einstein condensates. **Review of Modern Physics**, v. 81, n.2, p. 647-691, 2009. ISSN 00346861.

28 SONIN, E. B. Ground state and Tkachenko modes of a rapidly rotating Bose-Einstein condensate in the lowest-Landau-level state. **Physical Review A**, v. 72, n. 2, p. 021606, Aug. 2005. ISSN 1050-2947.

29 BLANC X.; ROUGERIE, N. Lowest-Landau-level vortex structure of a Bose-Einstein condensate rotating in a harmonic plus quartic trap. **Physical Review A**, v. 77, n. 5, p. 053615-8, 2008. ISSN 10502947.

30 COOPER, N. R.; KOMINEAS, S.; READ, N. Vortex lattices in the lowest Landau level for confined Bose-Einstein condensates. **Physical Review A**, v. 70, n. 3, p. 033604, Sept. 2004. ISSN 1050-2947.

31 WATANABE, G.; BAYM, G.; PETHICK, C. J. Landau Levels and the Thomas-Fermi structure of rapidly rotating Bose-Einstein condensates. **Physical Review Letter**, v. 93, n. 19, p. 190401, Nov. 2004. ISSN 0031-9007.

32 HO, T. L. Bose-Einstein Condensates with large number of vortices. **Physical Review Letter**, v. 87, n. 6, p. 060403–4, 2001. ISSN 10797114.

33 COOPER, N. Rapidly rotating atomic gases. **Advances in Physics**, v. 57, n. 6, p. 539–616, Nov. 2008. ISSN 0001-8732.

34 HEINRICHS, S.; MULLIN, W. J. Quantum-Monte-Carlo calculations for bosons in a two-dimensional harmonic trap. **Journal of Low Temperature Physics**, v. 113, n. 3-4, p. 231–236, July 1998. ISSN 00222291.

35 CAZALILLA, M. A.; HO, A. F.; GIAMARCHI, T. Interacting Bose gases in quasi-one-dimensional optical lattices. **New Journal of Physics**, v. 8, n. 8, p. 158–158, Aug. 2006. ISSN 1367-2630.

36 HO, T. L.; MA, M. Quasi 1 and 2d dilute Bose gas in magnetic traps: existence of off-diagonal order and anomalous quantum fluctuations. **Journal of Low Temperature Physics**, v. 115, n. 1-2, p. 61–70, 1999. ISSN 00222291.

37 PETROV, D. S.; HOLZMANN, M.; SHLYAPNIKOV, G. V. Bose-Einstein condensation in quasi-2D trapped gases. **Physical Review Letters**, v. 84, n. 12, p. 2551–2555, Mar. 2000. ISSN 0031-9007.

38 HERVE, M. d. G. **Superfluid dynamics of annular Bose gases**. 2018. 216 p. Thesis (PhD) — Université Paris 13, Paris, 2018.

39 WING, W. H. On neutral particle trapping in quasistatic electromagnetic fields. **Progress in Quantum Electronics**, Elsevier, v. 8, n. 3-4, p. 181–199, 1984.

40 RABI, I. I. *et al.* A new method of measuring nuclear magnetic moment. **Physical Review**, v. 53, n. 4, p. 318–318, Feb. 1938. ISSN 0031-899X.

41 PERRIN, H.; GARRAWAY, B. M. Trapping atoms with radio frequency adiabatic potentials. **Advances In Atomic, Molecular, and Optical Physics**, v. 66, p. 181–262, 2017.

42 COLOMBE, Y. *et al.* Ultracold atoms confined in rf-induced two-dimensional trapping potentials. **Europhysics Letters**, v. 67, n. 4, p. 593–599, Aug. 2004. ISSN 0295-5075.

43 FRYE, K. *et al.* **The Bose-Einstein condensate and cold atom laboratory**. Dec. 2019. Available at: http://arxiv.org/abs/1912.04849. Access at: 11/10/2022.

44 LESANOVSKY, I.; KLITZING, W. von. Time-averaged adiabatic potentials: versatile matter-wave guides and atom traps. **Physical Review Letters**, v. 99, n. 8, p.083001, Aug. 2007. ISSN 0031-9007.

45 BARRETT, B. *et al.* The Sagnac effect: 20 years of development in matter-wave interferometry. **Comptes Rendus Physique**, Elsevier Masson SAS, v. 15, n. 10, p.875–883, Dec. 2014. ISSN 16310705.

46 RYU, C. *et al.* Observation of persistent flow of a Bose-Einstein condensate in a toroidal trap. **Physical Review Letters**., v. 99, n. 26, p. 260401, Dec 2007. ISSN 0031-9007.

47 BRAND, J.; REINHARDT, W. P. Generating ring currents, solitons and svortices by stirring a Bose-Einstein condensate in a toroidal trap. **Journal of Physics B**, v. 34, n. 4, p. L113, Feb. 2001. ISSN 0953-4075.

48 COZZINI, M.; JACKSON, B.; STRINGARI, S. Vortex signatures in annular Bose-Einstein condensates. **Physical Review A**, v. 73, n. 1, p.013603, Jan. 2006. ISSN 1050-2947.

49 GUO, Y. *et al.* **Supersonic rotation of a superfluid**: a long-lived dynamical ring. p. 3, July 2019. Available at: https://arxiv.org/abs/1907.01795. Access at: 11/10/2022.

50 JACKSON, A. D.; KAVOULAKIS, G. M.; LUNDH, E. Phase diagram of a rotating Bose-Einstein condensate with anharmonic confinement. **Physical Review A**, v. 69, n. 5, p.053619, May 2004. ISSN 1050-2947.

APPENDIX

APPENDIX A – VIRIAL THEOREM

In this appendix we discuss the virial theorem, which is useful to re-express some terms in our sum rules expressions in terms of energy values. We assume the particles of the gas to undergoe contact two-body interaction described by a Delta function, and the external potential to be either the Mexican Hat (MH) or the shifted harmonic oscillator (SHO). We also assume the Hamiltonian to be

$$H = \sum_{i=1}^{N} \left[\frac{\boldsymbol{p}_i^2}{2M} + V(\boldsymbol{r}_i) \right] + g_{2D} \sum_{i<j} \delta\left(\boldsymbol{r}_i - \boldsymbol{r}_j\right) - \sum_{i=1}^{N} \boldsymbol{\Omega} \cdot \left(\boldsymbol{r}_i \times \boldsymbol{p}_i\right). \tag{A.1}$$

If the state is stationary then

$$\frac{d}{dt} \left\langle \sum_i \boldsymbol{r}_i \cdot \boldsymbol{p}_i \right\rangle = 0, \tag{A.2}$$

where $\langle ... \rangle$ denotes the expectation value, $\boldsymbol{r}_i, \boldsymbol{p}_i$ are the position and momentum vector of the particles, g_{2D} is the interaction parameter, M is the mass of the particles, $\boldsymbol{\Omega}$ is the angular velocity and V is the potential function.

On the other hand,because of Heisenberg's equation of motion

$$\frac{d}{dt} \sum_i \boldsymbol{r}_i \cdot \boldsymbol{p}_i = \frac{i}{\hbar} \left[\hat{H}, \sum_i \boldsymbol{r}_i \cdot \boldsymbol{p}_i \right]. \tag{A.3}$$

For the MH potential

$$V^{\mathrm{MH}}(\rho) = \frac{1}{2} \left(-\rho^2 + \lambda \rho^4 \right) \tag{A.4}$$

we obtain

$$E_{kin} + E_{int} + E_{ho} - \lambda \left\langle \rho^4 \right\rangle = 0. \tag{A.5}$$

Here,

$$E_{kin} = \left\langle \sum \frac{\boldsymbol{p}_i^2}{2M}_i \right\rangle, \tag{A.6}$$

$$E_{int} = \left\langle g_{2D} \sum_{i<j} \delta\left(\boldsymbol{r}_i - \boldsymbol{r}_j\right) \right\rangle, \tag{A.7}$$

and

$$E_{ho} = \left\langle \frac{M\omega^2}{2} \sum_i \rho_i^2 \right\rangle. \tag{A.8}$$

Equation (A.5) can be rewritten as

$$2E_{kin} - 2E_{trap}^{\mathrm{MH}} + 2E_{int} - \lambda \left\langle \rho^4 \right\rangle = 0, \tag{A.9}$$

with

$$E_{trap}^{\mathrm{MH}} = -\frac{1}{2} \left\langle \rho^2 \right\rangle + \frac{\lambda}{2} \left\langle \rho^4 \right\rangle . \tag{A.10}$$

On the other hand, for the SHO potential

$$V^{\mathrm{SHO}} \left(\rho \right) = \frac{1}{2} \left(\rho - \rho_0 \right)^2 \tag{A.11}$$

we have

$$2E_{kin} + 2E_{int} - 2E_{ho} + \rho_0 \left\langle \rho \right\rangle = 0, \tag{A.12}$$

which can be rewritten as

$$2E_{kin} - 2E_{trap}^{\mathrm{SHO}} + 2E_{int} - \rho_0 \left\langle \rho \right\rangle + \rho_0^2 = 0, \tag{A.13}$$

with

$$E_{trap}^{\mathrm{SHO}} = \left\langle \frac{M\omega^2}{2} \sum_i \left(\rho_i - \rho_0 \right)^2 \right\rangle . \tag{A.14}$$

APPENDIX B – COMPRESSIBILITY MODES

In this appendix we discuss the calculation of the m_{-1} moments, quantities that are useful in computing m_1/m_{-1} which is a more stringent upper bound to the frequency of the collective modes than the usual m_3/m_1 which we used in past chapters. In contrast to the other moments, m_{-1} cannot be expressed in terms of commutators of perturbation operators and the system's Hamiltonian; instead, it is related to the system static response function $\chi_M(0)$. A natural rule for calculating m_{-1} is through the explicit determination of the polarization $\propto \chi(0)$ induced in the system by an external static field. The details of the calculation are different for each mode, as we shall proceed to discuss.

From linear response theory, we knows that if F is an hermitian operator (15):

$$2m_{-1} = -\chi_M(0). \tag{B.1}$$

For m_1^+ moment we have already calculated for a quadrupole perturbation

$$m_1^+ = \frac{8N\hbar^2\left\langle\rho^2\right\rangle}{M}. \tag{B.2}$$

In order to determine the static response function $\chi_M(0)$ we first consider the Hamiltonian:

$$H = \sum_{i=1}^{N}\left[\frac{p_i^2}{2M} + V(\boldsymbol{r}_i)\right] + g_{2D}\sum_{i<j}^{N}\delta(\boldsymbol{r}_i - \boldsymbol{r}_j) - \sum_{i=1}^{N}\boldsymbol{\Omega}\cdot(\boldsymbol{r}_i \times p_i), \tag{B.3}$$

where N is the number of the mass M particles, p_i, $\boldsymbol{r}_i$ are the momentum and position vectors of the i-th particle, g_{2D} is the two dimensional interaction parameter and $\boldsymbol{\Omega}$ is the angular velocity vector. To this Hamiltonian, we add the quadrupolar perturbation

$$\delta V_{ext} = \frac{M}{2}\omega_0^2\varepsilon\left(x^2 - y^2\right), \tag{B.4}$$

which reproduces the required asymmetry to produce the mode. More specifically, we are interested in calculating (15):

$$m_{-1}^{Q} = \frac{4N}{M\omega_0^2}\lim_{\epsilon\to 0}\left\langle x^2 + y^2\right\rangle\left(\frac{\partial\delta_\varepsilon}{\partial\varepsilon}\right), \tag{B.5}$$

where

$$\delta_\varepsilon \equiv \frac{\left\langle y^2 - x^2\right\rangle}{\left\langle x^2 + y^2\right\rangle}. \tag{B.6}$$

The calculation of δ_ε require us to make some assumptions. In the MH potential, let us assume the system to be described by a Thomas-Fermi profile and in a vortex lattice regime. Then

$$n_{V_L}^{MH}(\rho) = \frac{\mu + \frac{M\Omega^2}{2}\left(x^2+y^2\right) + \frac{M\omega_0^2}{2}\left[\left(1+\varepsilon\right)x^2 + \left(1-\varepsilon\right)y^2\right] - \frac{1}{2}M\omega_0^2\lambda\left(x^2+y^2\right)^2}{g_{2D}}.$$

By using Eq.(B.5) is easy to show that

$$m_{-1}^{+} = \frac{\pi}{3g_{2D}}\frac{N}{M\omega_0^2}\left(R_2^6 - R_1^6\right), \tag{B.7}$$

where $R_{1,2}$ are the two Thomas-Fermi radii, with $R_2 > R_1$. So

$$\frac{m_1^+}{m_{-1}^+} = 4\hbar^2\omega_0^2\lambda\frac{R_+^2R_-^4}{3R_+^4 + R_-^4}, \tag{B.8}$$

with $R_+^2 \equiv R_1^2 + R_2^2$ and $R_-^2 \equiv R_2^2 - R_1^2$.

The full expressions depends on the configuration of the vortices and the potential:

- Mexican Hat, vortex lattice:

$$\frac{m_1^+}{m_{-1}^+} = 4\hbar^2\omega_0^2\frac{\left(1+\left(\Omega/\omega_0\right)^2\right)\eta^2}{3\left(1+\left(\Omega/\omega_0\right)^2\right)^2 + \eta^2}, \tag{B.9}$$

- Mexican Hat, macrovortex (charge ν):

$$\frac{m_1^+}{m_{-1}^+} = 4\hbar^2\omega_0^2R_-^2\frac{12\nu^2 + R_+^4 - R_-^4}{3R_+^8 - 2R_-^4R_+^4 - R_-^8}. \tag{B.10}$$

- Shifted harmonic oscillator, vortex lattice:

$$\frac{m_1^+}{m_{-1}^+} = \hbar^2\omega_0^2\frac{8\left(1-\left(\Omega/\omega_0\right)^2\right)\left(3d^4 + 20R^2d^2\right)}{5\left(3d^4 + 40d^2R^2 + 48R^4\right)}, \tag{B.11}$$

where $d \equiv R_2 - R_1$ is the width and $R \equiv \left(R_1 + R_2\right)/2$ is the mean radius.

- Shifted harmonic oscillator, macrovortex:

$$\frac{m_1^+}{m_{-1}^+} = \hbar^2\omega_0^2\frac{8d^2\left[\left(d^2-4R^2\right)^2\left(3d^2+20R^2\right) - 48\left(d^2-20R^2\right)\nu^2\right]}{5\left(d^2-4R^2\right)^2\left(3d^2+40d^2R^2+48R^4\right)}. \tag{B.12}$$

INDEX